

TERAHERTZ MICRO-RESONATORS  
INVESTIGATED IN THE NEAR- AND  
FAR-FIELD

*Arkabrata Bhattacharya*

The cover image is a photograph to be defined

ISBN: XXX

A catalogue record is available from the Eindhoven University of Technology Library.  
A digital version of this thesis can be downloaded from <http://www.differ.nl>

# **Terahertz Micro-resonators Investigated in the Near- and Far-field**

PROEFSCHRIFT

ter verkrijging van de graad van doctor aan de  
Technische Universiteit Eindhoven, op gezag van de  
rector magnificus prof.dr.ir. F. P. T. Baaijens, voor een  
commissie aangewezen door het College voor  
Promoties, in het openbaar te verdedigen op dinsdag  
30 mei 2016 om 16:00 uur

door

Arkabrata Bhattacharya

geboren te West Bengal, India

Dit proefschrift is goedgekeurd door de promotiecommissie:

voorzitter: prof. dr. ir. G. M. W. Kroesen  
1<sup>e</sup> promotor: prof. dr. J. Gómez Rivas  
2<sup>e</sup> promotor: prof. dr. A. Fiore  
leden: dr. M. Matters-Kammerer  
prof. dr. L. Kuipers  
prof. dr. R. Hillenbrand  
prof. dr. R. Kersting  
prof. dr. L. D. A. Siebbeles

This work was supported by the Netherlands Foundation for Fundamental Research on Matter (FOM), the Netherlands Organization for Scientific Research (NWO) and the European Research Council (ERC) through Grant No. 259272 THZ-PLASMON.

*To my family and friends*



# Contents

<b>1</b>	<b>Introduction</b>	<b>9</b>
1.1	Light: A historical perspective . . . . .	10
1.2	Photonic devices for communication, sensing and other applications . . . . .	12
1.3	THz frequencies . . . . .	13
1.4	Generation and Detection of THz radiation . . . . .	14
1.4.1	Photoconductive Antennas . . . . .	15
1.4.2	Optical Rectification and Electro-Optic sampling . . . . .	16
1.4.3	Built-In Field in Semiconductors . . . . .	17
1.4.4	Photo-Dember effect . . . . .	17
1.5	THz spectroscopy . . . . .	18
1.5.1	THz Time-Domain Spectroscopy . . . . .	19
1.5.2	Time-Resolved THz Spectroscopy . . . . .	20
1.6	Outline of the thesis . . . . .	22
<b>2</b>	<b>On Near-fields and THz frequencies</b>	<b>23</b>
2.1	Theoretical foundations of the rigorous diffraction theory and diffraction limit . . . . .	24
2.1.1	Propagation of light in matter . . . . .	25
2.1.2	The Fresnel and Fraunhofer approximations: the near and far-fields . . . . .	29
2.1.3	Image of a point source and diffraction limit . . . . .	32
2.1.4	The Vector approach to the rigorous diffraction theory . . . . .	34
2.2	Light-matter interaction in the sub-wavelength scale: to create, to manipulate and detect local fields . . . . .	35
2.2.1	“There’s plenty of room at the bottom” . . . . .	35
2.2.2	Creation of local fields: evanescent fields and field enhancements . . . . .	36
2.2.3	Manipulation of local fields: plasmons and surface waves . . . . .	38
2.2.4	Detection of local fields: near-field microscopy techniques . . . . .	41
2.3	Near-field measurement techniques . . . . .	43
2.4	THz near-field micro-spectrometer . . . . .	43
<b>3</b>	<b>Vectorial Mapping of Complex Electric Near-Field near THz resonators</b>	<b>47</b>
3.1	Introduction . . . . .	48
3.2	Terahertz near-field imaging . . . . .	49

## CONTENTS

---

3.3	Numerical simulations . . . . .	51
3.4	Conclusions . . . . .	55
<b>4</b>	<b>Large Near-to-Far Spectral Shifts for THz resonances</b>	<b>57</b>
4.1	Introduction . . . . .	58
4.2	Sample description . . . . .	59
4.3	Experimental results . . . . .	60
4.4	Numerical Simulations . . . . .	61
4.5	Driven-damped Harmonic Oscillator Model . . . . .	62
4.6	Fano model . . . . .	64
4.7	Conclusions . . . . .	66
<b>5</b>	<b>Diffraction enhanced transparencies and slow THz light</b>	<b>67</b>
5.1	Introduction . . . . .	68
5.2	Sample description . . . . .	69
5.3	Experimental results . . . . .	69
5.4	Coupled dipole model . . . . .	75
5.5	THz near-field imaging . . . . .	80
5.6	Conclusions . . . . .	81
<b>6</b>	<b>Visualizing mode hybridization in the near-field of terahertz dolmens</b>	<b>83</b>
6.1	Introduction . . . . .	84
6.2	Experimental results . . . . .	84
6.3	Conclusions . . . . .	88
	<b>References</b>	<b>91</b>
	<b>Summary</b>	<b>109</b>
	<b>List of Publications</b>	<b>113</b>
	<b>Acknowledgments</b>	<b>115</b>
	<b>About the author</b>	<b>115</b>

# CHAPTER 1

## INTRODUCTION

---

### 1.1 Light: A historical perspective

Out of the various ways we humans perceive nature, vision is the most dominant. The sheer amount of information we process through vision, as compared to the other senses, is overwhelming. The act of vision starts when the light from an object is imaged by the cornea and the lens in our eye to the light-sensitive membrane, the retina. This transduced information is further processed by our brain to complete our perception of the surroundings. The Oxford dictionary defines light as “The natural agent that stimulates sight and makes things visible”. Thus, it is not surprising that we, human beings, have always been fascinated by light.

Perhaps the oldest documented philosophical study of light dates back to the 4th or 5th century BC in ancient Indian schools of thought *Sankhya* and *Vaisheshika*. The first considered light as one of the five fundamental elements which makes up the universe. In the *Vaisheshika* school, light was thought of as very high velocity “atoms” or quanta of fire which can exhibit different characteristics depending on the velocity and arrangement of the fire atoms, and not as one of the fundamental elements. In ancient Greece, almost around the same time, *Empedocles* and *Plato* postulated that the universe was made of four elements similar to the *Vaisheshika* school of thought. *Empedocles* believed that Aphodite lit fire in our eyes which shone out and made sight possible. However, interaction between rays from eyes and from sun was necessary for vision (emission theory). Other philosophers like *Democritus*, *Epicurus* and *Aristotle* formed the opposing theory of vision which considered light from objects are captured by the human eye and the eye copies the image (intromission theory) of the objects. Many years after all these theories, emerged the writings of Euclid in a formal scientific text, *Optica* which describes his postulate about rectilinear propagation of light, mathematical description of reflection, refraction. He also questioned the previous theory of *Empedocles*. Later on, *Ptolemy* in his book, *Optics*, directly supported the intromission theory of light. These ideas were resurrected and extended in the middle ages by the Persian philosophers *Al-Kindi* and *Ibn Sahi* [1]. *Ibn Sahi*’s research went so far as to computing optimum curvatures and sizes of lenses and curved mirrors. Later, another Persian scholar *Ibn-al-Haytham* wrote the Book of Optics (*Kitab al-manazir*) [2] where he proposed experiments in optics for determining and explaining optical phenomenon like reflection and refraction. This text was initially ignored but later on became the standard text for the majority of Middle ages. It was in the early 17th century when Johannes Kepler explained in his writings what we know today as geometric optics as well as astronomical optical phenomena [3]. René Descartes in the mid 17th century theorised that light behaved as a mechanical wave and has higher velocities in denser media in analogy with sound waves [4]. Although incorrect, his theory is considered as the beginning of modern optics. Issac Newton expanded Descartes’ theory into the famous corpuscular theory of light, which stated that light is made up of small discrete particles called corpuscles which travel in a straight line with finite velocity and has a certain momentum [5]. He also theorised that white light is a mix of colors which can be separated out. Opposing theory was promoted almost immediately by Robert Hook [6] and later by Christiaan Huygens [7]. This theory considers light to have a wave nature, and is famously known today as the wave theory of light. Newton’s theory was widely accepted

over the wave theory up until the beginning of 19th century, when Thomas Young [8] and Augustin-Jean Fresnel [9] conducted their ground-breaking double-slit experiment which showed the interference of light and thus, reinstating Huygens' wave theory. This work was one of the most significant works of that time as it opened another domain of study which we know today as physical optics. In an independent theory by James Clerk-Maxwell about electromagnetism [10], optics fitted in and it was established that light is an electromagnetic wave. In 1899, Max Plank modelled the blackbody radiation successfully and showed that the energy exchange between light and matter happens in discrete quantities of energy known as *quanta* [11]. Albert Einstein's famous paper on the photo-electric effect established the quantization of light [12]. This led to a new field of research, quantum mechanics, which led to yet another more advanced explanation of light based on the theory of quantum electrodynamics.

Optics is formally defined by the Encyclopedia of Science and Technology (McGraw-Hill) as, "... the branch of physics which involves the behaviour and properties of light, including its interactions with matter and the construction of instruments that use or detect it." Although the theoretical knowledge and understanding of the basic nature of light began in the 4-5th century B.C. and evolved over time, the development of optical instruments to harness light for use has been known to man from even earlier periods. The earliest known lenses were made from polished crystals like quartz. They date back to 7th century B.C. in the ancient Egyptian and Mesopotamian civilizations. Ancient Romans have been known to use water in glass spheres as lenses. This practical use of light along with the philosophical explanations by the Indian and Greek civilizations spearheaded the development of optics through the centuries. Persians were known to use lenses and mirrors for burning before the Middle ages. Europe witnessed the first usable eyeglasses as early as the 13th century. These rudimentary methods finally paved the way for more complex optical innovation like compound microscopes [13] in the late 16th and refracting telescopes [14] in the 17th century. Since then there has been immense development of instrumentation over centuries both for enhancing imaging as well as analysing the behavior of light. History has witnessed development of imaging instruments such as complex microscopes [15–17], telescopes [18–20] and cameras [21] and analysing instruments such as interferometers [22, 23], photometers [24], polarimeters [25], spectrometers [26] to name a few.

The trend in optical instrumentation took a sharp turn with the invention of laser [27] in the 1960s followed by optical fibers [28, 29] and amplifiers [30, 31]. These inventions formed the bases of modern revolutions in telecommunication and internet. Another growth in this field was due to both advances and limitations faced in the field of electronics. The early 20th century saw a boom in technological advances in the field of electronics for its use in telecommunication, computing, sensing and power transmission. However, as the technology grew more and more complex, the challenges faced with respect to speed, power consumption and size became overwhelming. At this point scientists came to realize that electronics can be coupled to novel devices which use light to overcome these challenges. This motivation combined with the discovery of lasers spearheaded the still growing field of research: *photonics*. There has been an ever increasing demand to integrate these photonic devices to the existing electronic technology from the later half

of the 20th century up until now.

### **1.2 Photonic devices for communication, sensing and other applications**

*Photonics* has been defined as the science of light generation, detection and manipulation through emission, transmission, modulation, signal processing, switching, amplification and detection/sensing [32, 33]. Optical devices which have been known to mankind from ancient times can arguably fit into this definition. However, in the modern world the connotation of photonics has a whole new level of understanding. The evolution of the level of instrumentation for manipulation of light-matter interaction which has been achieved in the last 50 years is phenomenal. All of the modern developments of photonics can be attributed to the discovery, which revolutionized modern optics, of the *laser* in 1960 by T. H. Maiman at the Hughes Research Laboratory [34]. The discovery of lasers remains the key discovery for the emergence of modern photonics as it was possible to achieve light sources with exceptional properties like spatial and temporal coherence with high intensities and control of amplitude, phase, frequency and polarization of the emitted light. The next key ingredient for the development of modern photonics is the development of semiconductor devices like light emitting-diodes (LEDs) [35], laser-diodes (LDs) [36] and photo-diodes (PDs) [37], which can generate and detect light. These devices not only allowed photonic devices to more compact sizes but also boosted up the efficiencies of light-matter interactions. Another ingredient which spearheaded the evolution of photonics was the discovery of optical fibers which allowed transmission of light with very low propagational losses. These developments with various others in electronics, electro-optics and quantum electronics led to the state-of-the-art photonics as we know it. Thus the classical optical instrumentation, which dealt mainly with reflection and refraction of light, combined with these new generation of optical instruments resulted in the development of photonics. Modern micro- and nano-fabrication techniques have evolved photonics to the whole new field of research of micro- and nano-photonics.

The applications of photonics are ubiquitous in our daily life. Perhaps the most important application of photonics was thought to be in the field of telecommunication. Fiber-optic communication has replaced long distance copper wire communication almost throughout the world mainly due to extremely lower attenuation and interference losses as well as very high bandwidths. Optical fibers acts as the communication channel in this process. Light-emitting diodes or laser diodes acts as the source for these channels. Information is transferred in the form of intensity of frequency modulated multiplexed optical waves, which are amplified at regular intervals using optical amplifiers (Er doping across the length of the fiber [38]). At the receiving end, the photodetector detects the optical signal using photo-electric effect and the signal is decoded electronically. Modulation and de-modulation of these signals are performed by optical modulators which are photonic devices which manipulate the the properties of the light by absorption and refraction. However, due to advances in the fabrication techniques, the photonic devices have evolved to sub-wavelength photonic structures that can harness electromagnetic

radiation at sub-wavelength scales and different frequency ranges. Periodic arrangements of these sub-wavelength structures forms photonic crystals [39–41] and surfaces [42–44] and can manipulate the macroscopic properties of light. This miniaturization has made these efficient devices applicable for other relevant fields as sensing and sub-wavelength spectroscopy, sub-wavelength optical devices like inter-connects, non-linear devices like optical transistors to be used in futuristic optical computational technologies. Daily usage of simple and complex photonic devices are already in the areas of medicine, industrial manufacturing, military, metrology to name a few.

There has been an enormous technological progress in photonics mainly around visible and infra-red frequencies over the past decades. In recent times, there has been a lot of interest in Terahertz (THz) frequencies because of their unique potential over the optical and infrared counterpart in several research areas such as sensing and communication. These unique properties will be discussed in the next section. The technological progress at THz frequencies in the past, however, was limited because of the unavailability of efficient THz emitters and detectors. With the advent of new discoveries at THz frequencies, harnessing this part of the electromagnetic spectrum became a reality. As a result of this, photonic engineering at THz frequencies, i.e., *THz photonics* has developed at a phenomenal pace.

### 1.3 THz frequencies

Terahertz (THz) frequency range refers to the range of the electromagnetic spectrum with frequencies typically ranging from 0.1 to 10 THz, which translates to free-space wavelengths of 0.3 to 3 mm, as shown in Fig. 1.1. The characteristic photon energies lie in the range of 0.4 to 40 meV.

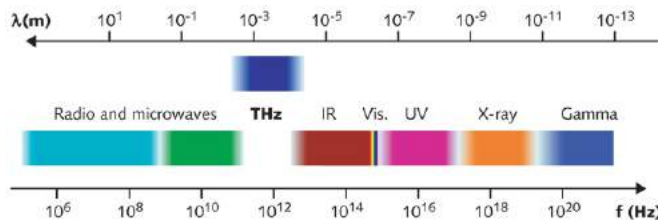


**Figure 1.1:** The electromagnetic spectrum showing the position of THz frequencies with respect to other frequency ranges (Picture from LaserFocusWorld.com)

The THz frequency range is in between the microwave and infrared frequencies in the electromagnetic spectrum. This radiation constitute a powerful tool to probe many physical phenomena in a broad range of materials like organic molecules, ionic crystals as well as in semiconductors. The rotational, vibrational and translational modes of molecules, radical and atoms of many materials have characteristic energies in the THz ranges, making this radiation an interesting candidate for spectroscopy. These materials are thus, transparent to THz with unique spectral fingerprints. Furthermore, THz radiation com-

binesthe advantage of relatively high spatial resolution compared to radio-frequencies along with a high penetration depth with low scattering, making it a perfect candidate for sensing and detection of different materials. This makes THz studies very relevant for security, medical, chemical, quality control as well as material science applications. THz photons have very low photon energies compared to X-rays and ultraviolet frequencies and are hence, non-ionizing. This renders THz safe for probing biological matter *in-vivo*, making it very useful for non-invasive drug detection, medical, bio-imaging industries. At these frequencies, it is possible, through time-domain spectroscopy techniques, to measure both the amplitude and phase of the electric field simultaneously. Similar capabilities at optical frequencies have been developed recently [45–48], but they are very complex compared to the techniques used at THz frequencies. From the knowledge of the transient electric field at the THz regime it is possible to extract the complex dielectric function of a material from direct measurements [49], rather than from complex Kramers-Kronig analysis [50]. At the same time pump-probe techniques allows us to measure the dynamical response of charge carriers in most materials, i.e., this is a direct measurement of charge carrier lifetimes [51]. This information about physical quantities of materials is relevant for applications of these materials. Semiconductors are good examples of materials which have been extensively studied using THz techniques. New materials, like perovskites, graphene and 2D semiconductors have evolved over the past decade, which showing an immense potential for renewable solar energy applications [52–54]. THz radiation has a great potential for the characterization of these materials. Hence, THz frequencies have the promise to be a very efficient tool for contact-less, non-invasive probing of physical properties for many materials, therefore, finding relevance in many disciplines of research as well as in industrial applications. However, THz research is still developing as the equipments used are conventionally large, expensive and require special operating conditions. This makes THz technology hard to be implemented in daily applications. But researchers are striving hard to beat these limitations to realize the real potential of this frequency range.

The THz frequency range was and it is still referred to as the “THz gap” [55]. The main reason for this was the unavailability of efficient devices which operates in this frequency range. In the lower photon energies, i.e. the microwaves, device fabrication was limited to frequencies lower than 100 GHz. While in the higher side of the spectrum, i.e. the optical frequencies, interband laser diodes were already designed, but no suitable semiconductors could be found for extending the same techniques to THz frequencies at room temperature. However, it is not surprising that THz techniques grew exponentially over the past years considering the interesting applications discussed previously.

### 1.4 Generation and Detection of THz radiation

Before going any further it is important to discuss briefly the various methods for the generation and detection of THz radiation. With rapid technological progress, many techniques for generation and detection of THz radiation are available at present, such as photo-conductive antennas [56], optical rectification and electro-optic sampling in

non-linear crystals [57, 58], built-in fields and the photo-Dember effects in semiconductors [59, 60], air-photonics [61, 62], molecular gas lasers [63], free-electron lasers and synchrotron [64, 65], quantum cascade and semiconductor lasers [66, 67]. In the following section, we discuss a few of the conventional techniques which are commonly used in THz research.

### 1.4.1 Photoconductive Antennas

Out of the various methods for generation of THz radiation, the use of photoconductive antenna is the oldest one [56]. This technique uses an above-the-band-gap laser pulse to generate free charge carriers in the conduction band of a semiconductor under an applied bias voltage. The voltage bias accelerates the generated free carriers and hence gives rise to an electromagnetic pulsed radiation which is typically in the THz frequency range. The schematic of this process is shown in Fig. 1.2(a). The response of this device depends not only on the exciting laser pulse, but also on the time response of the semiconducting material. The resulting THz radiation typically has bandwidths in the order of a few THz.

For detection, the same device is used but in a reversed configuration [68]. The excitation laser pulse generates the free carriers as before, but in this case there is no biasing voltage which accelerates the charges. It is the electric field of the THz radiation which gives the necessary bias and as a result, a current is generated which is proportional to the magnitude of the THz electric field. In this case, it is very important that the generation and subsequent recombination of the free carriers are very fast compared to the slowly-varying THz electric field, such that the THz electric field at one time instant acts as a DC bias to the device. Hence, the semiconductor for the photo-conductive antennas are grown at low-temperature to introduce surface defects which reduces the carrier lifetimes. By controlling the time delay between the THz radiation and the excitation pulse, it is possible to map the THz electric field pulse as a function of time. This is schematically shown in Fig. 1.2(b).

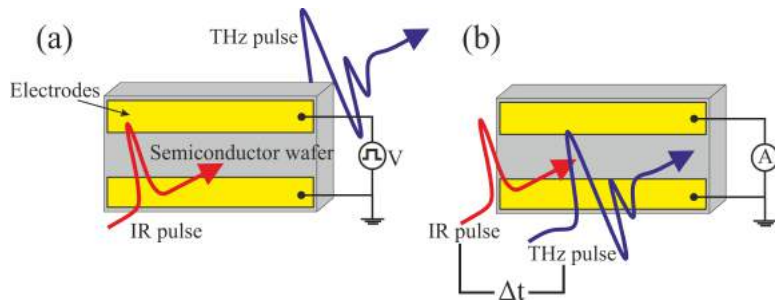


**Figure 1.2:** Schematic representation of the operating principle of photo-conductive antennas for (a) generation of THz radiation and (b) detection of THz.



of polarization is detected with the use of a quarter-wave plate, a Wollaston prism and a balanced photodiode (BPD). The change in the polarization, i.e., the difference in signal of the BPD is directly proportional to the amplitude of the THz. Thus, by changing the time delay between the probe beam and the THz the electric field of the THz can be measured as a function of time. This scheme is shown in Fig. 1.3(b).

### 1.4.3 Built-In Field in Semiconductors

In some semiconductors the surface states may have a different Fermi energy than the bulk material. A classic example of such a semiconductor is GaAs. The energy bands below the surface in such materials bend due to the difference in the Fermi levels. This leads to the formation of built-in surface fields near the band-bending area. This is shown by the schematic in Fig. 1.4. The figure shows the band-bending and surface fields in an n-type GaAs wafer. The Fermi level of the wafer is near the conduction band, whereas the Fermi level of the surface state is near the center of the bandgap, i.e., lower than the Fermi level of the bulk. As a result, the surface field drives the free electrons towards the bulk material and there is a creation of a depletion layer near the surface. When excited with a laser pulse above the bandgap, the photo-induced electron hole pairs are accelerated by the existing electric field, similar to a photo-conductive antenna. This sets the electrons and holes in a dipolar oscillation until an equilibrium is reached and consequently a THz pulse is generated [59].

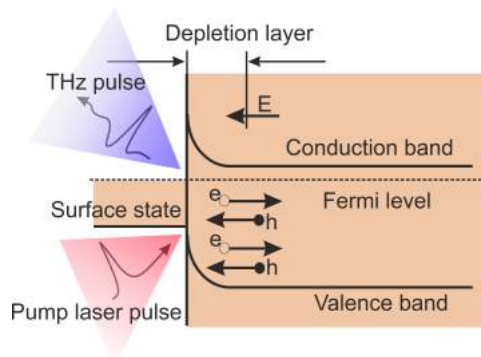


**Figure 1.4:** In-built field effect in an n-doped GaAs wafer for the generation of THz.

### 1.4.4 Photo-Dember effect

THz pulse can be generated even without the presence of built-in fields in some semiconductors with ultra-fast laser pulses. This is known as the photo-Dember effect [60]. When a laser pulse with photon energy over the bandgap of the material is absorbed, electron-hole pairs are created. However, as the absorption of the laser beam is strong, the distribution of the electron-hole pairs is very inhomogeneous close to the surface. This

asymmetry leads to a diffusion of electrons and holes towards the bulk of the material. However, the diffusion speeds between the electrons and holes are different owing to the higher mobility of electrons than holes. This difference in speeds leads to charge separation in the semiconductor and the generation of a transient photo-Dember field, which in turn generates the THz radiation. Usually InSb, owing to its high electron mobility is considered to be a promising THz emitter among the other semiconductors with low bandgap. The main striking feature of this effect is that, the polarity of the THz radiation is the same for both n- and p-type semiconductors, which is not the case in in-built fields in semiconductors [75, 76]. The photo-Dember effect is schematically represented in Fig. 1.5.

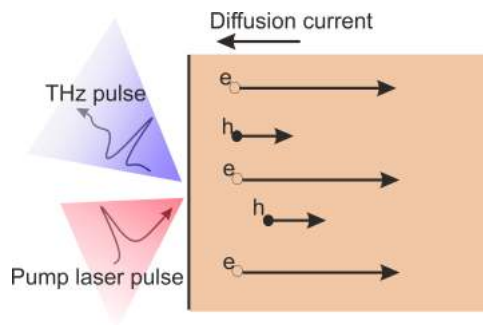


**Figure 1.5:** Photo-Dember effect in a semiconductor wafer for the generation of THz radiation.

## 1.5 THz spectroscopy

As discussed earlier, many materials have characteristic fingerprints in the THz frequency range, making this part of the electromagnetic spectrum very interesting and unique to study the interaction of matter with light. Furthermore, the THz electromagnetic field oscillations are slow enough to be measured in the laboratory. An extended technique is THz time-domain spectroscopy (THz-TDS) [49]. The ability to measure electric field as a function of time opens up a whole new dimension for THz spectroscopy. The knowledge of the complete electromagnetic field enables us to extract the complete information about the interaction between light and matter under question.

THz electric field oscillations lasts typically for about a few picoseconds. As a result THz can and has been extensively used to probe ultrafast dynamics of charge carriers in semiconductors as well as other materials. This technique is known as time resolved THz spectroscopy (TRTS) [51]. Semiconductors remain the most probed material with THz not only because of ultrafast processes, but also because of the fact that the excitonic states in these materials have typical binding energies in the THz frequencies.

Owing to extremely low perturbations caused by THz radiation compared to the bandgap energies in most materials, they serve as an excellent agent to probe conductivity

of materials in a non-invasive and non-contact fashion. This property of THz is ever more important now because of the advent of new complex materials like perovskites, 2D semiconductors organic polymers and graphene with potential applications in energy research.

### 1.5.1 THz Time-Domain Spectroscopy

THz Time-Domain Spectroscopy (THz-TDS) is a spectroscopic technique which uses short THz pulses to probe the physical properties of a material. In this technique, the detection is sensitive to the changes caused by the interaction of THz radiation with matter both in amplitude and phase. THz-TDS intrinsically gives more information on the light-matter interaction than conventional spectroscopic techniques at optical frequencies, where the detection is sensitive to field intensities only.

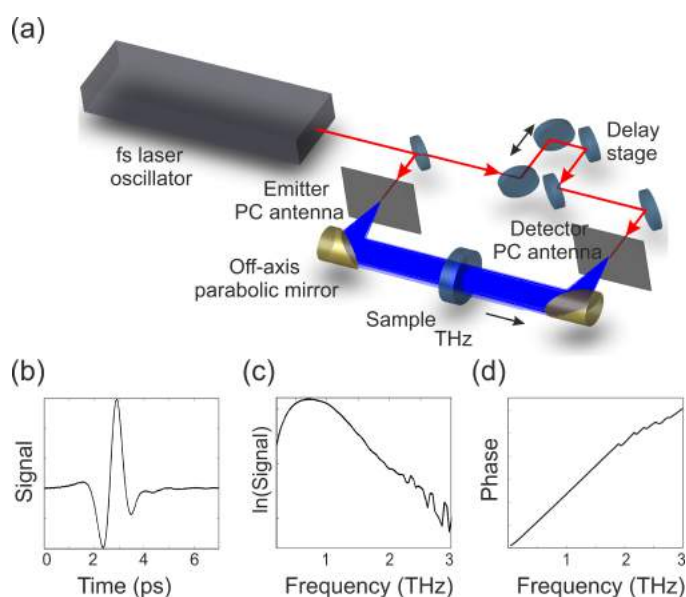


**Figure 1.6:** (a) Schematic representation of THz time-domain spectroscopy using photoconductive generation and detection mechanism. (b) Typical THz transient measured from such a setup, (c) Intensity spectrum in log scale and (d) Phase spectrum generated by Fourier transforming the measured transient

A typical THz time-domain spectrometer is shown in Fig. 1.6(a). A train of single cycle THz pulses is generated by an ultrafast pulsed infrared laser with photo-conductive sampling technique. Each of these pulses usually lasts for about a few picoseconds and contains frequency components typically in the range of 0.1 to 10 THz. This pulse train is incident onto the sample and is detected by another photoconductive antenna which is gated by a fraction of the IR beam from the laser. The path length between the emitter and the detector can be controlled by a delay stage. For each position of the delay stage

the detector measures a current proportional to the amplitude of the THz pulse at a corresponding time instant. By changing the time delay between the THz pulses and the IR gating pulses, the whole THz transient signal can be measured. This signal is Fourier transformed to generate the amplitude and phase spectrum which represents the interaction of the THz with the material in question. The THz generation and detection can be done alternatively with any of the schemes described in the previous section. Figures 1.6(b), (c) and (d) show a typical THz transient measured by this setup, the intensity and phase spectrum generated by Fourier transforming this transient signal respectively.

### 1.5.2 Time-Resolved THz Spectroscopy

Time-Resolved THz Spectroscopy (TRTS) is a technique which is used to study the transient properties of a material upon optical excitation on a sub-picosecond time scale. This technique is also known as optical pump-THz probe spectroscopy.

The schematic of a typical TRTS setup is shown in the Fig. 1.7(a). This setup is similar to a THz-TDS setup with an additional path which brings a significant fraction of the amplified optical pulse onto the sample. The generation of the THz is done with a photo-conductive antenna as in the previous case. The detection is done using optical rectification as discussed previously. By positioning the delay stage in the THz generation path (Delay line 1), it is possible to fix the detection to the amplitude peak of the THz pulse. By scanning the delay stage of the optical pump beam (Delay line 2) the time delay in the excitation of the sample can be controlled. Thus, the change of the THz peak amplitude in the detection with pump time delays can be measured, which is a measure of the transient decay of the material response upon optical excitation. This decay can be measured for any position in the THz transient by controlling the delay line 1. A typical THz transient measured for a fixed position in delay line 2 is shown in Fig. 1.7(b). For a fixed position in delay line 1 (corresponding to the position of the THz peak amplitude marked by the red circle in Fig. 1.7(b)), the dynamic response of the sample can be measured by scanning delay line 2, as shown in Fig. 1.7(c).

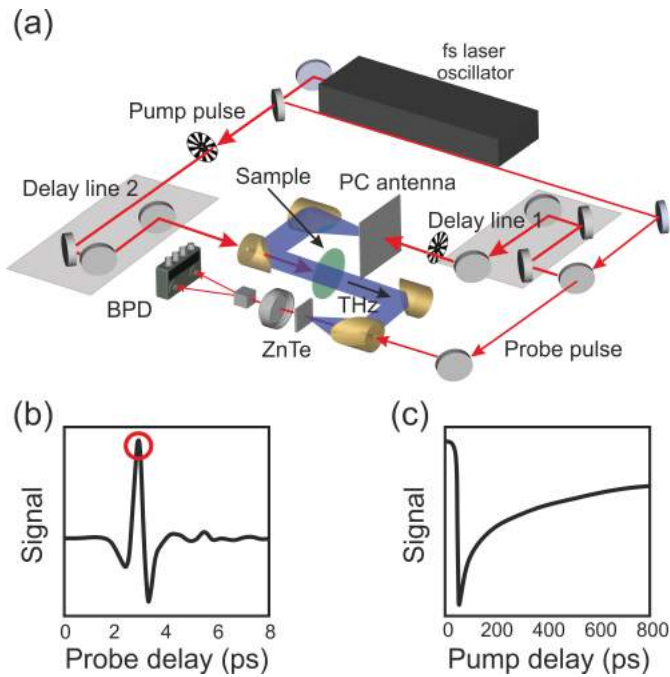


**Figure 1.7:** (a) Schematic representation of a Time-Resolved THz Spectroscopy setup using photo-conductive generation and electro-optic detection. (b) Typical THz transient measured from such a setup. The red circle is centered around the maximum amplitude of the THz transient, where the delay stage in the THz generation path is locked and (c) illustrates the change of the maximum amplitude as a function of the delay between optical pump and the probe THz pulse.

## 1.6 Outline of the thesis

This thesis studies the interaction of THz light with resonant structures both in the near- and far-field. In the *Introduction* chapter we describe the evolution of optics and photonics in general followed by a general introduction to THz frequencies and instrumentation needed for generation and detection of THz waves. The chapter ends with a description of conventional far-field spectroscopic techniques at THz frequencies.

In *Chapter 2*, we present the theoretical foundations of diffraction theory and its significance in the propagation of electromagnetic waves. We also describe the limit of resolution in the far-field and hence the necessity to study electromagnetic fields in the near-field region of sub-wavelength structures. We further describe the creation, manipulation and detection of near-fields and the related instrumentation. Further, this chapter describes instrumentation specific to THz near-field measurements.

In *Chapter 3*, we use the near-field spectroscopic technique discussed in Chapter 2 to perform vectorial mapping of the electric near-field components of a gold rod resonant at THz frequencies, both in amplitude and phase. This chapter focusses on a scheme to measure directly the different spatial components of the near-field associated with a resonant structure under illumination.

In *Chapter 4*, we study the far-field and the near-field spectral responses of a resonant structure (bow-tie resonator) and show that conventional spectral characterization of such resonances in the far-field leads to indeterministic results due to interference between the scattered and incident fields. This chapter focusses on the relationship between the spectral responses on the near- and far-fields due to resonant structures and reinstates the necessity of near-field measurements for their accurate characterization.

In *Chapter 5*, we study a photonic metasurface (frequency detuned and displaced resonant rods) based on far-field coupling between periodic structures and show that these structures can induce a transparency window, i.e., a frequency window of near unity transmission and reduce the group velocity of THz light by 4 orders of magnitude. Further study of such structures in the near-field reveals the basic physics behind the formation of such induced transparencies and group velocity reduction. This chapter focusses on the manipulation of the macroscopic spectral response of resonant structures through far-field coupling in the sub-wavelength scales.

In *Chapter 6*, we study a photonic structure (dolmens) with a response based on near-field coupling of resonances and show a transparency window and associated group velocity reductions similar to that of the previous chapter, induced by the hybridization of modes. We further show that reducing the distance between the structures increases the near-field coupling and hence, enhances the associated hybridization. This chapter focusses on the manipulation of the macroscopic spectral response of resonant structures using near-field coupling between them.

In a broad context, this thesis aims to provide a holistic picture of how THz frequencies interact with resonant sub-wavelength structures in the near-field. It focusses on the generation and detection of THz near-fields around resonant structures, its relationship with conventional far-field responses and the effect on the macroscopic response in the far-field due to manipulation of local electromagnetic fields.

## CHAPTER 2

# ON NEAR-FIELDS AND THZ FREQUENCIES

---

*The understanding of how photonic devices work at THz frequencies requires a fundamental description of electromagnetic waves in the near-field regions of the structures. Diffraction theory explains how light fields propagate to the so called “far-field” as well as get confined to the “near-field” regions. In this chapter, we describe the basics of diffraction theory and resolution limit of far-field imaging, which was the primary motivating factor behind the evolution of near-field optics. This description is summarized from standard text books (Refs. [77–79]). We also present the theory and techniques behind the generation, manipulation and detection of near-field in the THz frequency range. Finally we present the THz near-field micro-spectroscopy setup that was built and used for the measurements discussed throughout this thesis.*

## 2.1 Theoretical foundations of the rigorous diffraction theory and diffraction limit

Early developments of optical instruments were based on the understanding of light as rays which travels in straight lines and can refract at optical interfaces and reflect from surfaces. These assumptions did not consider the wave nature of light, however they worked to describe most of the observed phenomena and formed the basis of what we know today as *geometrical optics*[80]. Our understanding of light since the early 19th century has shown us compelling evidence about the wave nature of light. This led to the understanding that geometrical optics is a very accurate approximation of the behavior of light whenever the wavelength is very short compared to the size of the object that it interacts with. Although geometrical optics gives very accurate description of the propagation of light where it is applicable, it breaks down for objects which are comparable to the wavelength of light. It is in these situations that the wave nature of light comes into play and the theory of *diffraction* explains the propagation of light.

The theory of diffraction has a fascinating history behind its development. The first scientific report on unexplained behavior of light came from Grimaldi's work in 1655 [81]. He illuminated a sharp aperture and observed that the image on the screen is a blur rather than a sharp and well defined circle as predicted by the corpuscular theory of light of Isaac Newton [5]. The first understanding of such unexplained behavior of light was in the year 1678 when Christian Huygens first published his work on the wave nature of light [82]. He intuitively expressed that if each point on a wavefront of a disturbance were considered as a source of a secondary spherical perturbation, then the wavefront at the next time instant can be found by constructing the envelope of these secondary wavelets. This idea was not instantly accepted due to the strong support of "corpuscular" theory of propagation of light by Newton. However, the famous "double-slit" experiments by Thomas Young in 1804 [8], reinstated the wave-theory of the propagation of light by introducing the concept of *interference*, which critical for a wave propagation. By combining the ideas of Huygens and Young, Augustin Jean Fresnel in 1818 was able to calculate the distribution of light in diffraction patterns [9]. In his theory, he allowed the mutual interference between the secondary wavelets and used some arbitrary assumptions of amplitude and phase of these wavelets. This theory was contradicted and ridiculed by the scientific community. It was only after the integration of electro-magnetism by Maxwell in 1860 [10], which gave the needed mathematical framework for the development of Fresnel's ideas, when Fresnel's ideas began to get accepted. It was Gustav Kirchhoff who developed the advanced mathematics integrating the ideas of Huygens and Fresnel [83]. He showed that the intuitive assumptions of Fresnel were indeed logical and that these are a consequence of the wave nature of light. However, the theory had assumptions which were proved to be inconsistent by Poincafe [77] and Sommerfeld [77, 84]. As a result, Kirchhoff's formulation of the Huygens-Fresnel principle can be seen as a first approximation to the diffraction problem, although it yields very accurate results when compared to experiments. Sommerfeld eliminated the assumptions used by Kirchoff on the amplitude and phase of secondary wavelets by using certain boundary conditions to the Green's function[85, 86]. This is the

so-called *Rayleigh-Sommerfeld diffraction theory* and will be treated later in this chapter. It is worth mentioning that both Kirchhoff and Sommerfeld approximated the optical field to be scalar. This approximation yields accurate results when the diffracting aperture is much larger than the wavelength of light and the diffracting field is not observed too close to the aperture. This forms the basis of *scalar diffraction theory*. Although the scalar theory of diffraction does not yield correct results in the sub-wavelength regime, near very small structures, they give an excellent qualitative understanding of the diffraction problem in general. The vectorial description of diffraction theory was treated successfully for the first time by Kottler [87] and others [88]. However, with the advent of modern computers, a more practical approach to study the diffraction problem for complex sub-wavelength structures is numerically, by solving Maxwell's equations rather than the analytical diffraction theory.

### 2.1.1 Propagation of light in matter

In the year 1873, James Clerk Maxwell, in his book *Treaties of Electricity and Magnetism* [10], formulated for the first time the general laws which formed the basis of what we know as the electromagnetic theory of light. In his theory, he predicted that the general behavior of all electric, magnetic and electromagnetic waves are governed by the same set of laws, which we know today as the Maxwell's equations [79]:

$$\nabla \times \bar{E} + \frac{\partial \bar{B}}{\partial t} = 0, \quad (2.1)$$

$$\nabla \times \bar{H} - \frac{\partial \bar{D}}{\partial t} = \bar{J}, \quad (2.2)$$

$$\nabla \cdot \bar{D} = \rho, \quad (2.3)$$

$$\nabla \cdot \bar{B} = 0. \quad (2.4)$$

In these equations,  $\bar{E}$  and  $\bar{H}$  are the electric and magnetic field vectors (in SI units). These vectors describe the electro-magnetic field. The physical quantities  $\bar{D}$  and  $\bar{B}$  are the electric displacement and the magnetic induction vectors, respectively, which represent the effect of the electromagnetic field on matter. The quantities  $\rho$  and  $\bar{J}$  represent the electric charge density and electric current density vector respectively. These quantities represents the source from which the electro-magnetic field generates. From these sets of equations, the electro-magnetic fields can be fully characterized once the relationship between the  $\bar{E}$  and the  $\bar{H}$  as well as the  $\bar{D}$  and  $\bar{B}$  are known. The equations which defines the relation between these quantities are know as the constitutive equations, and they depend on the properties of the matter in which the wave propagates. The constitutive equations are,

$$\bar{D} = \epsilon \bar{E} = \epsilon_0 \bar{E} + \bar{P}, \quad (2.5)$$

$$\bar{B} = \mu \bar{H} = \mu_0 \bar{H} + \mu_0 \bar{M}. \quad (2.6)$$

In these equations the  $\epsilon$  and  $\mu$  are constitutive parameters, which are known as dielectric and permeability tensors of the medium, respectively.  $\epsilon_0$  and  $\mu_0$  are the vacuum permittivity and permeability. When the electromagnetic field propagates through matter,

the electric field perturbs the motion of the charge carriers and produces an effective charge separation, which leads to formation of dipolar polarization in the material per unit volume, known as electric polarization,  $\overline{P}$ . Similarly, the magnetic field can induce magnetization in matter known as magnetic polarization,  $\overline{M}$ . For an isotropic medium both  $\epsilon$  and  $\mu$  reduce to scalars.

If we consider the propagation of an electromagnetic field in a dielectric, non-magnetic, isotropic, non-dispersive medium, in absence of free charges, the Maxwell's equations in Eq. (2.1) reduces to,

$$\nabla \times \overline{E} + \mu \frac{\partial \overline{H}}{\partial t} = 0, \quad (2.7)$$

$$\nabla \times \overline{H} - \epsilon \frac{\partial \overline{E}}{\partial t} = 0, \quad (2.8)$$

$$\nabla \cdot \epsilon \overline{E} = 0, \quad (2.9)$$

$$\nabla \cdot \mu \overline{H} = 0. \quad (2.10)$$

Solving Maxwell's equations for  $\overline{E}$  and  $\overline{H}$  leads to the set of differential equations which describe the propagation of electromagnetic waves,

$$\begin{aligned} \nabla^2 \overline{E} - \frac{n^2}{c^2} \frac{\partial^2 \overline{E}}{\partial t^2} &= 0, \\ \nabla^2 \overline{H} - \frac{n^2}{c^2} \frac{\partial^2 \overline{H}}{\partial t^2} &= 0, \end{aligned} \quad (2.11)$$

where  $n$  is the refractive index of the medium and is defined as

$$n = \left( \frac{\epsilon}{\epsilon_0} \right)^{1/2}, \quad (2.12)$$

and  $c$  represents the velocity of propagation of the electro-magnetic wave in vacuum and is given by

$$c = \frac{1}{\sqrt{\mu_0 \epsilon_0}}. \quad (2.13)$$

Since the vector wave equations (Eq. (2.11)) are obeyed by both  $\overline{E}$  and  $\overline{H}$ , it is possible to construct an identical scalar equation which is obeyed by all the components of electric and the magnetic vectors. Hence, the generalized scalar wave equation is,

$$\nabla^2 u(\overline{r}, t) - \frac{n^2}{c^2} \frac{\partial^2 u(\overline{r}, t)}{\partial t^2} = 0, \quad (2.14)$$

where  $u(\overline{r}, t)$  can be any of the components of the electric or magnetic fields as a function of position and time. This implies that all components of the electric and magnetic fields behave identically in a linear, isotropic, homogeneous and non-dispersive dielectric medium and the behavior can be described by the scalar wave equation. For a monochromatic wave, the scalar field can be written as,

$$u(\overline{r}, t) = \text{Re}\{U(\overline{r})e^{-2\pi i\nu t}\}, \quad (2.15)$$

where  $U(\vec{r})$  is a complex function of position. As, the time dependance is known a priori, the complex function  $U(\vec{r})$  fully describes the wave. Hence, Eq. (2.14) becomes,

$$(\nabla^2 + k^2)U = 0, \quad (2.16)$$

where  $k = 2\pi n\nu/c = 2\pi/\lambda$  is known as the wave number. Equation (2.16) is known as Helmholtz equation and defines the behavior of a complex amplitude of a monochromatic wave propagating through a homogeneous dielectric medium ( $n \geq 1$ ) [77].

The calculation of the complex disturbance  $U$  at an observation point can be accomplished by the use of Green's theorem [77, 85]. The theorem states: *Let  $U(P)$  and  $G(P)$  be any two complex-valued functions of position, and let  $S$  be a closed surface surrounding a volume  $V$ . If  $U$ ,  $G$ , and their first and second partial derivatives are single values and continuous within and on  $S$ , then we have,*

$$\iiint_V (U\nabla^2 G - G\nabla^2 U) dv = \iint_S \left( U \frac{\partial G}{\partial n} - G \frac{\partial U}{\partial n} \right) ds \quad (2.17)$$

where  $\frac{\partial}{\partial n}$  is the partial derivative in the outward normal direction at each point on  $S$ . This theorem forms the basis of wave propagation in matter. The problem can be described by the Fig. 2.1. However, this theorem applies to the wave propagation only with a proper choice of an auxiliary function  $G$  and a proper  $S$ , which is an arbitrary closed surface around the observation point. The Kirchhoff-Helmholtz solution to this problem is based on the choice of  $G$ , which is

$$G(|r|) = \frac{e^{ik|\vec{r}-\vec{r}_0|}}{|\vec{r}-\vec{r}_0|}. \quad (2.18)$$

This function represents a spherical wave in free space of unit amplitude around  $P(\vec{r}_0)$  observed at  $Q(\vec{r})$ , and  $|\vec{r}-\vec{r}_0|$  represents the distance between the two points P and Q (See Fig.2.1). This  $G(|r|)$  is also known as the free space Green's function. The validity of the chosen Green's function to the diffraction problem relies on the fact that it has to be continuous within the enclosed volume and have continuous first and second partial derivatives in  $V$ . So, to exclude the discontinuities in at P, we need to choose a small spherical surface  $S_\epsilon$  of radius  $\epsilon$  around P as shown in Fig. 2.1. If Green's theorem is applied to the volume  $V'$  between  $S$  and  $S_\epsilon$ , along with  $G$  satisfying Helmholtz equation within the volume  $V'$ , we arrive at the Helmholtz-Kirchhoff integral theorem,

$$U(P) = \frac{1}{4\pi} \iint_S \left( \frac{\partial U}{\partial n} \left[ \frac{e^{ik(r-r_0)}}{r-r_0} \right] - U \frac{\partial}{\partial n} \left[ \frac{e^{ik(r-r_0)}}{r-r_0} \right] \right) dS. \quad (2.19)$$

This equation allows us to express the field at any point P in terms of boundary values of the wave on any closed surface surrounding that point. This relation plays the most significant role in the development of scalar diffraction equations.

Kirchhoff formulated the diffraction by an aperture in an infinite opaque screen using Helmholtz-Kirchhoff integral with a careful choice of the surface of integration. This is illustrated by the schematic shown in Fig. 2.2. In the figure, we consider that the infinite opaque screen is illuminated by a monochromatic source from left by a point Q and we

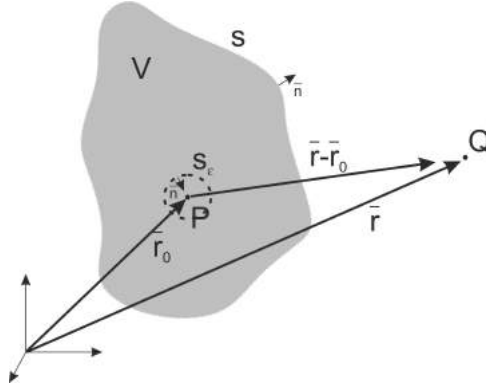


**Figure 2.1:** Implementation of Green's theorem for calculating the Helmholtz-Kirchhoff integral theorem

want to find the field distribution at point, P using the Helmholtz-Kirchhoff integral. Kirchhoff used some approximations for solving this problem. First, he assumed that across the surface  $\Sigma$ , the field distribution  $U$  and its derivative  $\partial U/\partial n$  are exactly the same as they would be in absence of the screen. Secondly, the part of surface  $S_1$  that is in the shadow of the screen, has  $U = \partial U/\partial n = 0$ . These conditions are known as *Kirchhoff's boundary condition*[77, 89]. Both of these assumptions are not true in reality, however holds under the approximation that the aperture is large compared to the wavelength. A further simplification to the problem is made by assuming that the points P and Q are many wavelengths away from the aperture. Now, if we consider that the aperture is illuminated by a single spherical wave from Q, the disturbance in point P can be expressed as,

$$U(P) = \frac{A}{i\lambda} \iint_{\Sigma} \frac{e^{ik(r_1+r_0)}}{r_1 r_0} \left[ \frac{\cos(\hat{n}, \bar{r}_0) - \cos(\hat{n}, \bar{r}_1)}{2} \right] dS, \quad (2.20)$$

where, A is the amplitude of the spherical wave from point Q. This result holds for illumination by a single point source and is known as the *Fresnel-Kirchhoff diffraction formula* or *Kirchhoff's solution of Huygens-Fresnel principle*[77]. It can be seen that interchanging the position of the source and object yields the same result, i.e. Eq. (2.20) is symmetric with respect to P and Q. This is known as the *Helmholtz reciprocity theorem*.

We can rewrite Eq. (2.20) in the following form,

$$U(P) = \iint_{\Sigma} U'(P_0) \frac{e^{ikr_0}}{r_0} dS, \quad (2.21)$$

where

$$U'(P_0) = \frac{1}{i\lambda} \left[ \frac{Ae^{ikr_1}}{r_1} \right] \left[ \frac{\cos(\hat{n}, \bar{r}_0) - \cos(\hat{n}, \bar{r}_1)}{2} \right]. \quad (2.22)$$

Equation (2.21) shows that the disturbance at P is the result of the sum of infinitesimally small point sources in the aperture itself. Each of these secondary sources has a certain

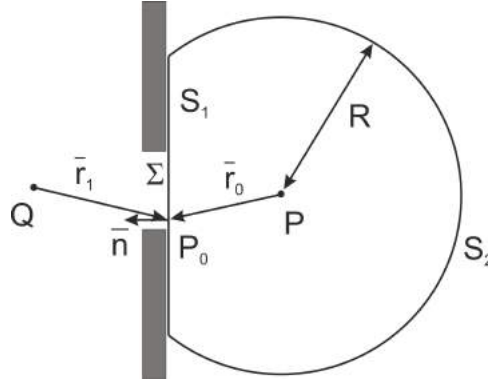


**Figure 2.2:** Kirchhoff's formulation of diffraction by a plane screen with a point source illumination.

phase and amplitude which is described by  $U'(P_0)$  through Eq. (2.22). This further reinstates that the disturbance is related not only to the illumination wavefront, but also to the angle of illumination and angle of observation. These properties were assumed by Fresnel to be true for explaining Young's double slit results, and validated rigorously by Kirchhoff. Hence the name Fresnel-Kirchhoff diffraction formula or simply Kirchhoff's solution of Huygens-Fresnel principle.

As stated earlier, the Kirchhoff's solution to Huygens-Fresnel principle assumes certain boundary conditions which are inappropriate. It also becomes unusable when multiple sources are used. These inconsistencies were removed by Sommerfeld and the solution is known as the Rayleigh-Sommerfeld solution to Huygens-Fresnel principle [77]. Sommerfeld used an alternative Green's function using conjugate points of disturbance, i.e.,  $P$  as the mirror image of the point  $Q$  on the other side of the screen, to arrive at the disturbance at  $P$  due to  $P_0$  based on Fig. 2.2, which is,

$$U(P) = \frac{1}{i\lambda} \int \int_{\Sigma} U(P_0) \frac{e^{ikr_0}}{r_0} \cos(\hat{n}, \bar{r}_0) dS. \quad (2.23)$$

It should be noted that for small angles the Rayleigh-Sommerfeld solution yields exactly the same result as the Kirchhoff's solution to Huygens-Fresnel principle. Also, under the assumption that the point of disturbance is many wavelength away from the aperture, angles tend to be small and thus, Kirchhoff's solution also yields near-perfect results for the diffraction problem, in spite of the approximations.

### 2.1.2 The Fresnel and Fraunhofer approximations: the near and far-fields

Solutions to Huygens-Fresnel principle become more practical when they are expressed in Cartesian coordinates, as shown in Fig. 2.3. Here, the diffracting aperture is assumed to lie

in the  $(\xi, \eta)$  plane and the illumination is along the positive Z-axis from the left. Following Eq. (2.23), the disturbance across the  $(x, y)$  plane, parallel to the  $(\xi, \eta)$  plane is given by

$$U(P) = \frac{1}{i\lambda} \iint_{\Sigma} U(Q) \frac{e^{ikr_0}}{r_0} \cos(\theta) dS, \quad (2.24)$$

where  $\theta$  is the angle between the outward normal  $\hat{n}$  and the vector  $\vec{r}_0$ , which is the displacement vector from  $P$  to  $P_0$ . Under the small angle approximation, the Huygens-Fresnel principle can be written as

$$U(P) = \frac{z}{i\lambda} \iint_{\Sigma} U(\xi, \eta) \frac{e^{ikr_0}}{r_0^2} d\xi d\eta, \quad (2.25)$$

where

$$r_0 = \sqrt{z^2 + (x - \xi)^2 + (y - \eta)^2}. \quad (2.26)$$

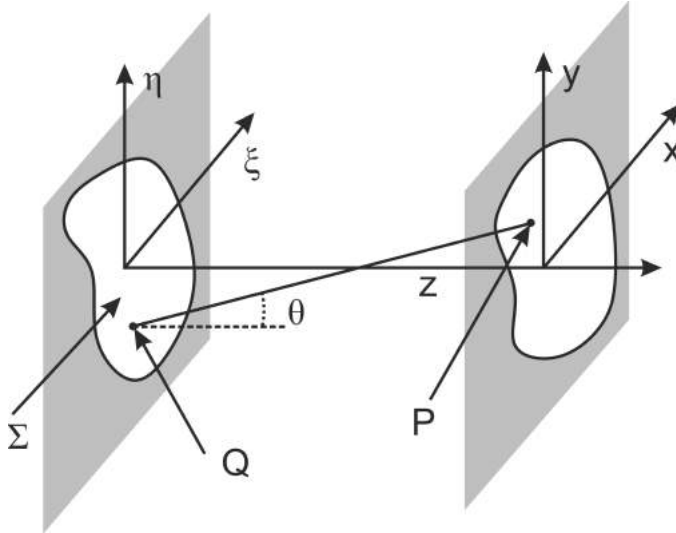


**Figure 2.3:** Fresnel-Kirchhoff formulation of diffraction geometry in rectangular coordinates.

**Fresnel approximation:** For simplifying Eq. (2.25) further we need certain approximations. Under the approximation that both  $(x - \xi)$  and  $(y - \eta)$  are smaller than  $z$ , Eq. (2.26) can be reduced using a Binomial expansion. Retaining the second order terms, we arrive at,

$$r_0 \approx z \left[ 1 + \frac{1}{2} \left( \frac{x - \xi}{z} \right)^2 + \frac{1}{2} \left( \frac{y - \eta}{z} \right)^2 \right]. \quad (2.27)$$

The effect of the second order terms becomes significantly large as  $r_0$  appears in the exponential and the k-vectors can have relatively large values in the Eq. (2.25). Thus it is

necessary to consider the second term when  $z$  is not very large compared to  $(x - \xi)$  and  $(y - \eta)$ . Using this approximation we arrive at the Fresnel approximation of the Huygens-Fresnel principle [77, 78, 90],

$$U(x, y) = \frac{e^{ikz}}{i\lambda z} e^{i\frac{k}{2z}(x^2+y^2)} \int \int_{-\infty}^{\infty} U(\xi, \eta) e^{i\frac{k}{2z}(\xi^2+\eta^2)} e^{-i\frac{2\pi}{\lambda z}(x\xi+y\eta)} d\xi d\eta. \quad (2.28)$$

Apart from the multiplicative factors, this equation can be recognized as the Fourier transform of the complex field right after the aperture multiplied by a quadratic phase factor. This expression is called the *Fresnel diffraction integral* and is used to calculate field distributions close to the diffracting aperture, also known as the *near-field region*. The Fresnel approximation, from the perspective of angular spectrum representation, can be interpreted as a small angle approximation. This is why Fresnel approximation is also known as the paraxial approximation. The quadratic phase factor can be eliminated by considering spherical surfaces with very large radii in Fig. 2.3 instead of planar surfaces. This approximation expresses the field on the spherical surface on the right as exact Fourier transform of the field at the spherical surface on the left. This implies that the quadratic phase factors in the Eq. (2.28) are simply paraxial representations of spherical surfaces.

**Fraunhofer approximation:** In addition to Fresnel approximation, another approximation is used in which we consider that the observation plane is far away from the diffracting aperture, i.e.

$$z \gg \frac{k(\xi^2 + \eta^2)_{max}}{2}, \quad (2.29)$$

and the quadratic phase factor becomes unity over the whole diffracting aperture. The field distribution can be found by a direct Fourier transform of the field distribution at the aperture itself. This approximation is known as the *Fraunhofer approximation* [78, 91]. The distances from the aperture where this approximation holds is known as the *far-field region*. The field distribution is given by

$$U(x, y) = \frac{e^{ikz}}{i\lambda z} e^{i\frac{k}{2z}(x^2+y^2)} \int \int_{-\infty}^{\infty} U(\xi, \eta) e^{-i\frac{2\pi}{\lambda z}(x\xi+y\eta)} d\xi d\eta. \quad (2.30)$$

This expression, as mentioned above, is the Fourier transform of the field distribution at the aperture with frequencies,

$$f_X = \frac{x}{\lambda z}, \quad (2.31)$$

$$f_Y = \frac{y}{\lambda z}. \quad (2.32)$$

$f_X$  and  $f_Y$  are known as *spatial frequencies* [78] and forms the basis of the angular spectrum representation in spatial coordinates, analogous to spectral distributions in temporal frequency space. The Fraunhofer approximation can be regarded as an special case of Fresnel approximation. The various zones (with changing  $z$ ) through which the Fresnel approximation transforms to Fraunhofer regimes is shown in Fig. 2.4.

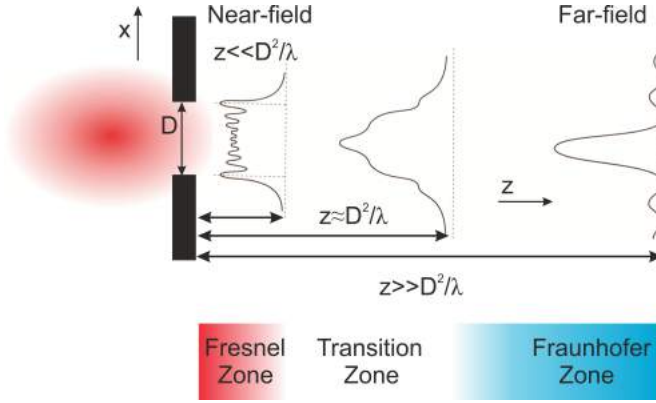


**Figure 2.4:** Fresnel (near-field) and Fraunhofer (far-field) zones as a function of distance from the diffracting aperture.

### 2.1.3 Image of a point source and diffraction limit

A point source can be thought of as an circular aperture lit by an uniform light source from the back. Considering the radius of the aperture to be  $d$  and  $q$  as the radial co-ordinate in the  $(\xi, \eta)$  plane of Fig. 2.3, the transmittance function is given by,

$$U(q) = \text{circ}\left(\frac{q}{d}\right) = \begin{cases} 1, & \text{if } q \leq d \\ 0, & \text{otherwise.} \end{cases} \quad (2.33)$$

Thus, if  $r$  is the radial component in cylindrical coordinates in the observation plane  $(x, y)$ , following Eq. (2.30),

$$U(r) = e^{ikz} e^{i\frac{kr^2}{2z}} \frac{A}{i\lambda z} \left[ 2 \frac{J_1(kdr/z)}{kdr/z} \right]. \quad (2.34)$$

where  $J_1$  is the Bessel function of the first kind of first order. This is a result of the Fourier-Bessel transform of the circular function in cylindrical coordinates. The corresponding intensity distribution in the far-field can be written as

$$I(r) = \left(\frac{A}{\lambda z}\right)^2 \left[ 2 \frac{J_1(kdr/z)}{kdr/z} \right]^2. \quad (2.35)$$

This intensity distribution is known as the *Airy pattern* [92, 93], named after George Biddell Airy who demonstrated this effect theoretically in 1835. Figure 2.5 shows the intensity distribution on the observation plane due to the diffracting aperture. The diffraction of a point source generates a blur in the observation plane. This is what Grimaldi described in his work on the first documented work on diffraction [81].

Since the field distribution from all light sources can be thought of as the interference of point sources, the intensity distribution on the observation plane can be thought of as a superposition of Airy patterns. Hence, imaging through any optical device sets a fundamental limit to the distance between two point sources after which the two images

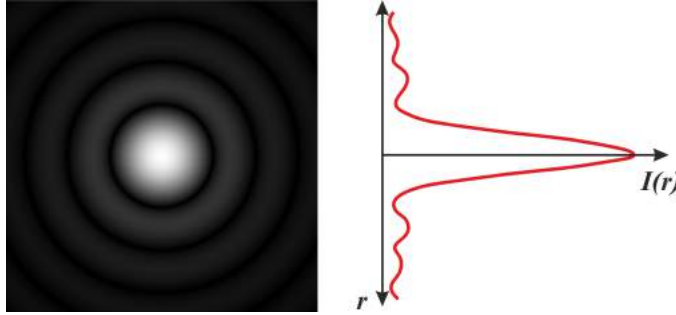


**Figure 2.5:** Intensity distribution of an Airy pattern in the observation plane. The red curve shows the cross-cut of this intensity distribution along the  $r$  coordinate.

cannot be resolved from each other. This limit is known as the *diffraction limit*. Imaging devices operating in the Fraunhofer regime (far-field) suffers from this fundamental limit, which restricts their capability to have infinite resolution. The factors which sets the limit of resolution are the size of the aperture of the optical element and the wavelength of light. Thus, optical imaging elements operating in the far-field are also known as *diffraction limited*.

There are several criteria which set a quantitative value to this phenomenon. The two most famous criteria are:

**Rayleigh criterion:** This criterion was set by Lord Rayleigh [94]. The Rayleigh criterion states that the two point sources are regarded as just resolved when the diffraction maximum of the first coincides with the first order minimum of the second. For larger separations the image is well resolved, otherwise it is unresolved. This criterion considers the two sources to have equal strengths. Following Eq. (2.35), for circular apertures Rayleigh criterion is given by

$$a = 1.22 \frac{\lambda z}{d}, \quad (2.36)$$

where  $a$  is the minimum resolvable distance between the two point sources in the aperture plane,  $z$  is the distance between the observation and aperture plane,  $d$  is the diameter of the aperture (for imaging systems, this is the diameter of the aperture of the system itself) and  $\lambda$  is the wavelength of the light.

**Sparrow criterion:** Most researchers found that images of point sources could still be resolved beyond the Rayleigh criterion. A more stringent criterion was set by Sparrow, where he considered a better overlap of the two Airy patterns such that the first and the second derivative of the combined intensity pattern vanish at the center. This is called the Sparrow criterion [95], and is given by

$$a = 0.94 \frac{\lambda z}{d}. \quad (2.37)$$

The two criteria for resolution of two point sources are shown in Fig. 2.6. For the Rayleigh criterion in (a), the position of the individual peaks of the Airy patterns coincide

with the first minimum of the other Airy pattern. This determines the limit of resolution for the Rayleigh criterion. In the Sparrow criterion (Fig. 2.6(b)), the distance between the Airy patterns is smaller.

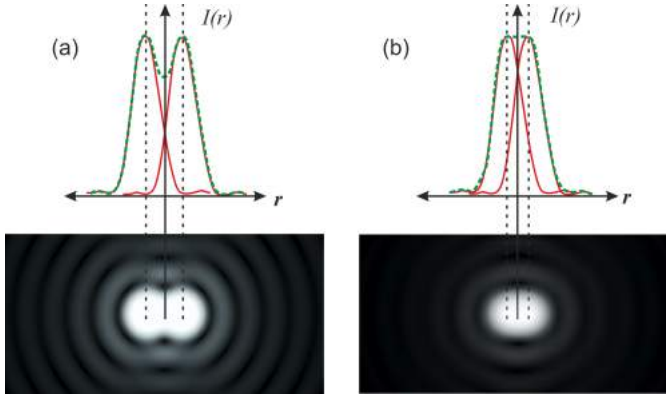


**Figure 2.6:** (a) Rayleigh criterion for the determination of the resolution limit. (b) Resolution limit in the Sparrow criterion. The red curves represents the individual Airy patterns of the two point sources, while the green curve is the image of the two sources. The vertical dotted lines indicate the position of the maxima of the individual Airy patterns.

### 2.1.4 The Vector approach to the rigorous diffraction theory

Scalar diffraction theory, as discussed in previous sections, gives extremely good agreement with experiments, as well as a basic understanding of the physics. However, when the diffracting structures have complex geometries, are comparable in size to the wavelength of light and the observation plane is very close to the structure, i.e. the diffracting plane, the theory is less accurate. As there is a trend to produce smaller devices, characterizing the light-matter interaction close to these structures are becoming increasingly important. This kind of characterization measurements have shown that the scalar theory of diffraction is mostly insufficient. As geometries get more and more complex, the pragmatic approach to tackle the problem is by numerical methods, rather than by analytical formulations. From the several ways of numerically solving Maxwell's equations, one of the most important is finite difference in time domain [96], (FDTD) [97].

In FDTD, Maxwell's equations are represented in central-difference equations, as shown in Eq. 2.38. The electric field is solved at a given instant in time, then the magnetic field is solved at the next time instant. This process is repeated iteratively many times. If we consider the curl of  $\vec{E}$  and  $\vec{H}$  from Eq. (2.7), we can immediately appreciate that the time derivative of the  $\vec{E}$  field is proportional to the curl of the  $\vec{H}$  field. This means that the new value of  $\vec{E}$  at point in space and time can be obtained from the value of  $\vec{E}$  in the previous time instant and the value of  $\vec{H}$  around  $\vec{E}$  in space. The curl equations of Eq. (2.7)

can be rewritten in terms of the vector components in Cartesian coordinates as,

$$\begin{aligned}
 \frac{\partial H_x}{\partial t} &= \frac{1}{\mu} \left( \frac{\partial E_y}{\partial z} - \frac{\partial E_z}{\partial y} - \rho' H_x \right), \\
 \frac{\partial H_y}{\partial t} &= \frac{1}{\mu} \left( \frac{\partial E_z}{\partial x} - \frac{\partial E_x}{\partial z} - \rho' H_y \right), \\
 \frac{\partial H_z}{\partial t} &= \frac{1}{\mu} \left( \frac{\partial E_x}{\partial y} - \frac{\partial E_y}{\partial x} - \rho' H_z \right), \\
 \frac{\partial E_x}{\partial t} &= \frac{1}{\epsilon} \left( \frac{\partial H_z}{\partial y} - \frac{\partial H_y}{\partial z} - \sigma E_x \right), \\
 \frac{\partial E_y}{\partial t} &= \frac{1}{\epsilon} \left( \frac{\partial H_x}{\partial z} - \frac{\partial H_z}{\partial x} - \sigma E_y \right), \\
 \frac{\partial E_z}{\partial t} &= \frac{1}{\epsilon} \left( \frac{\partial H_y}{\partial x} - \frac{\partial H_x}{\partial y} - \sigma E_z \right).
 \end{aligned} \tag{2.38}$$

These equations are solved in finite time differences using the Yee's algorithm[98]. In this algorithm, the Maxwell's curl equations are solved by using a set of finite difference equations. Each electric field component in 3-D is surrounded by four circulating magnetic field components and vice-versa. All the electric field components are computed at a particular time using the magnetic field at the previous time instant and vice-versa for the magnetic fields. Throughout this thesis we use a commercial FDTD software (Lumerical Solutions Inc. Vancouver, Canada) to verify the experimental results.

## 2.2 Light-matter interaction in the sub-wavelength scale: to create, to manipulate and detect local fields

Understanding the interaction of light with matter at sub-wavelength scales beyond the diffraction limit is essential for potential instrumentation, sensing and imaging applications. This study requires the understanding of generation, manipulation and detection of the elusive near-field in the vicinity of structures. However before going in depth, we discuss the broad aspects and motivation which emphasised the importance of the study of sub-wavelength structures.

### 2.2.1 “There’s plenty of room at the bottom”

Richard Feynman, in his legendary lecture [99] at the American Physical Society meeting at Caltech in 1959 proposed, for the first time, the idea of miniaturized matter in the sub-wavelength scales. He talked about the possibilities of “manipulating and controlling things on a small scale”[100] and predicted the endless possibilities associated with what we know today as “nanotechnology” [101]. With the advent of different possibilities of nano- and micro- fabrication, sample sizes were reduced dramatically, giving rise to new studies of light-matter interaction in sub-wavelength scales.

As suggested by Feynman, focussed electron beams have been used in the recent past to write nanoscale samples, what we know today as electron beam lithography [102]. He suggested the use of electron beams for imaging atoms, which was the idea behind the development of electron microscopes [103]. His ideas regarding complex, active nanoscale mechanisms in biology forms the basis of recent techniques used in state-of-the-art biotechnology. A major driving force behind the trend towards nano-science and nano-technology was originally for miniaturization and integration of electronic circuits for the computer industry. More recent shift of focus in this field is fueled by the fact that as we move towards smaller scales, new physics becomes more prominent with the promise of exploitation in future technologies.

A large part of this technology is inspired by examples in nature. Some examples include the efficient photosynthetic membranes in leaves for harvesting solar energies and channeling it to neighboring proteins, diffractive nano-structures used by butterflies to render beautiful colors, nano-scale structures found in the retina of various insects which acts as anti-reflection coatings, to name a few. Over the years, we have successfully harvested some of nature's creations and functionalized several devices based on their working principles. We have used single molecules to probe the local distribution electromagnetic fields [104], resonant sub-wavelength structures as sensors [105], localized sources of photons for high-resolution microscopy [106], sub-wavelength cavities with extremely high quality factors for enhanced non-linear responses [107], surface-plasmon waveguides for guiding light in sub-wavelength scales [108], photonic bandgap systems to suppress light propagation at specific frequencies [109] etc.

As mentioned earlier, the very basis of these advances and the implementation of these techniques to miniaturization of devices relies on the study of light-matter interactions in sub-wavelength scales. A systematic study can be divided into the following three parts: first, the one which deals with the generation of electromagnetic waves in the sub-wavelength regime. Secondly, the study of manipulation and interaction of these fields with structures and finally, the microscopic detection of the response from these interactions in sub-wavelength scales.

### 2.2.2 Creation of local fields: evanescent fields and field enhancements

In this section we describe the angular spectral decomposition of an electromagnetic field propagating in a homogeneous medium. Any arbitrary electromagnetic field propagating in a homogeneous medium can be considered as a series expansion of plane (and evanescent) waves with variable amplitudes and propagation directions. Let us consider  $E(\vec{r})$  is the field at a point in a plane  $z=\text{const}$  after being scattered by an arbitrary object as shown in Fig. 2.7. In this plane the 2-D Fourier transform of  $E$  can be written as,

$$\hat{E}(k_x, k_y; z) = \frac{1}{4\pi^2} \int_{-\infty}^{\infty} \bar{E}(x, y, z) e^{-i[k_x x + k_y y]} dx dy, \quad (2.39)$$

where  $x$  and  $y$  are transverse Cartesian coordinates and  $k_x$  and  $k_y$  are the corresponding wave-vectors in the reciprocal space. Similarly, the inverse Fourier transform reads,

$$\bar{E}(x, y, z) = \int_{-\infty}^{\infty} \hat{E}(k_x, k_y; z) e^{i[k_x x + k_y y]} dk_x dk_y, \quad (2.40)$$

If we assume that the transverse plane in the medium is homogeneous, isotropic, linear and source-free, the time harmonic optical field satisfies the vector form of the Helmholtz equation in Eq. (2.16). The conservation of momentum requires

$$k_z = \sqrt{(k^2 - k_x^2 - k_y^2)} \quad \text{with} \quad \text{Im}\{k_z\} \geq 0. \quad (2.41)$$

The Fourier spectrum  $\hat{E}$  evolves in  $z$  as,

$$\hat{E}(k_x, k_y; z) = \hat{E}(k_x, k_y; 0) e^{\pm i k_z z}. \quad (2.42)$$

The  $\pm$  sign indicates the superposition of two solutions which are propagating waves in positive and negative directions. The factor  $e^{\pm i k_z z}$  propagates the Fourier spectrum at  $z = 0$  to the plane at  $z = \text{constant}$  and is known as a propagator in reciprocal space. Hence combining Eq. (2.40) and Eq. (2.42) we arrive at,

$$\bar{E}(x, y, z) = \int \int_{-\infty}^{\infty} \hat{E}(k_x, k_y; 0) e^{i[k_x x + k_y y \pm k_z z]} dk_x dk_y. \quad (2.43)$$

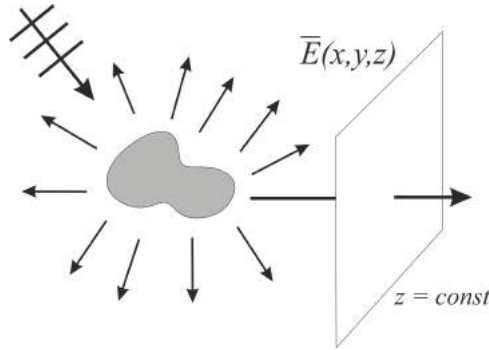


**Figure 2.7:** Wave propagation after being scattered by an object.

This equation along with its magnetic field counterpart is known as the *angular spectrum representation* of an electromagnetic field along the propagation direction. For the electric and the magnetic fields to be solutions of Maxwell's equation, they need to be divergence free, i.e.,  $\nabla \cdot \bar{E} = 0$ . This restricts the  $k$ -vectors to have directions perpendicular to the spectral amplitudes. For a purely dielectric medium,  $k_z$  can have either real or imaginary values. This implies that the propagator  $e^{\pm i k_z z}$  has an oscillatory nature or an exponentially decaying, i.e., *evanescent*, nature. Thus for certain values of  $(k_x, k_y)$  two

distinct set of solutions can be defined,

$$\text{Plane waves: } e^{i[k_x x + k_y y]} e^{\pm i k_z |z|}, \quad k_x^2 + k_y^2 \leq k^2, \quad (2.44)$$

$$\text{Evanescent waves: } e^{i[k_x x + k_y y]} e^{-|k_z||z|}, \quad k_x^2 + k_y^2 \geq k^2. \quad (2.45)$$

Hence, we see that the angular spectrum of an electromagnetic field is indeed a superposition of plane waves and evanescent waves. This means that if we consider propagation of an arbitrary electromagnetic field, the larger the angle between the  $k$ -vector with the  $z$ -axis, the larger are the  $k_x$  and  $k_y$  components. For the first limiting case, we can consider the mode propagating along the  $z$ -axis. This mode has  $k_x^2 + k_y^2 = 0$ . The other limiting case is the mode which travels at perpendicular direction to the  $z$ -axis and has the maximum transverse oscillation, i.e.  $k_x^2 + k_y^2 = k^2$ . This is illustrated in Fig. 2.8(a). However, for higher spatial frequencies, the modes are evanescent, as shown in Fig. 2.8(b). As the spatial frequencies increase the evanescent modes decay faster along the  $z$ -axis, which sets a practical limit to the angular bandwidth of an electromagnetic wave. It can be seen from Fig. 2.8 that since, the  $k$ -vectors inside the circle propagate, an image formed in the far-field is only a low-pass filtered version of the original source. The high spatial frequencies that lie outside the circle are filtered out as the evanescent waves do not propagate to the far-field. Hence there is always a loss of information on propagation from near- to far-field. The direct consequence of this is that any object which has dimensions lesser than  $1/k$  can not be imaged in far-field with enough accuracy. This makes the study of electric as well as magnetic fields in the near-field or the Fresnel zone very important.

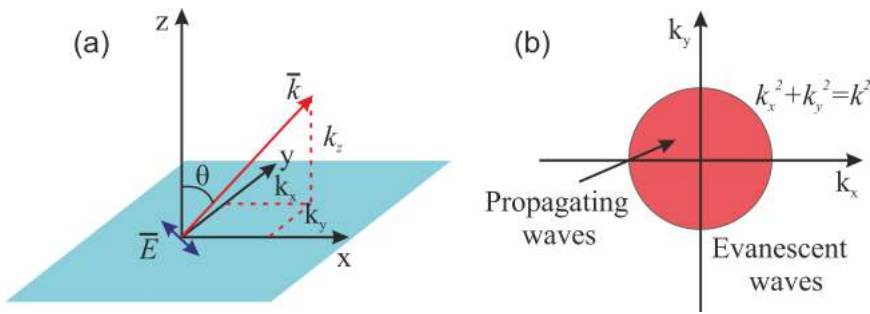


**Figure 2.8:** (a) Represents the wave propagating along angle  $\theta$  with  $z$ -axis. The blue line indicates the polarization of the plane wave, the red line indicates the  $k$ -vector and the dotted-red lines indicate the components of the  $k$ -vector. (b) Propagating waves have sum of squares of  $x$ - and  $y$ -components of the  $k$ -vector smaller than or equal to the  $k$ -vector squared, i.e., they lie inside the red circle, while the evanescent fields lie outside the circle throughout the  $k$ -space.

### 2.2.3 Manipulation of local fields: plasmons and surface waves

The interaction of light with conducting materials is largely dictated by the free charge carriers. The response of metals to light is described by the Drude-Sommerfeld model [110],

which states that the free electrons oscillate  $\pi$  radians out of phase relative to the driving field. This free electron cloud can sustain surface charge density oscillations, which have distinct resonant frequencies, as shown in Fig. 2.9(a). These oscillations are known as *surface plasmon polaritons* [111]. It is to be noted that response of materials near the surface plasmon polariton frequency can not be replicated in other spectral ranges using scale invariance of Maxwell's equations, as material properties are frequency dependent. The surface charge density associated with surface plasmons in a material at the interface with dielectric can generate strongly enhanced optical near-fields that are spatially confined near the interface. The surface plasmon polaritons, besides being confined to the interface, are dispersive and highly dissipative. In case of structured conducting particles this oscillation of electrons is confined by the particle geometry. In this case, the coherent oscillation of the free electrons is known as the *Localized Surface Plasmon Resonance* (LSPR) [112, 113], as illustrated in Fig 2.9(b). By structuring conductive matter, electromagnetic near-fields can be manipulated and enhanced. This makes the study of surface plasmon polaritons and LSPRs significantly important for understanding the interaction of light with matter at sub-wavelength scales.

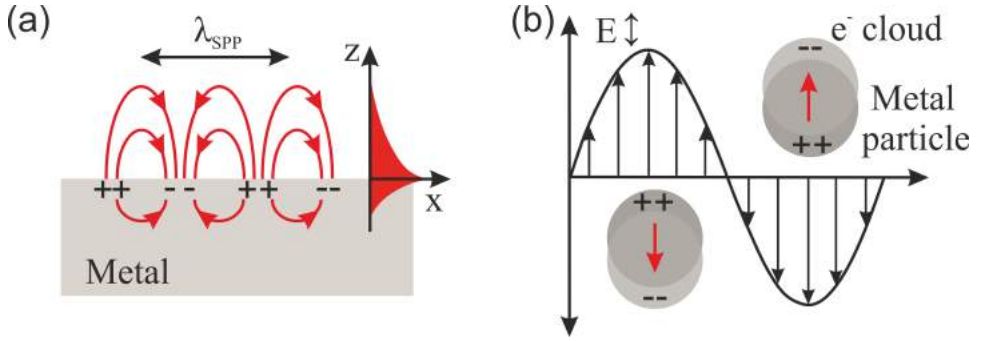


**Figure 2.9:** (a) Surface plasmon polariton on a metal-air interface. The red arrows denote the electric field lines generated by the plasmonic oscillations. (b) Localized surface plasmon polaritons oscillating out of phase with the incident electric field bound by the boundaries of the particle. The red arrow denote the electric displacement vector due to the plasmonic oscillations in the particle.

The Drude-Sommerfeld model was proposed by Paul Drude in 1900. The model approximates conduction electrons in metal-like matter as a gas of freely moving spheres. This movement is assumed to be intrinsically random and the external field acts as a source of acceleration of the electrons in between internal collisions among them. This acceleration leads to a small drift for the electrons. As a result a net drift current is generated, which is proportional to the complex conductivity of the material and the applied field. The complex conductivity is expressed as,

$$\tilde{\sigma} = \frac{\omega_p^2 \tau \epsilon_0}{1 - i\omega\tau}, \quad (2.46)$$

where  $\omega_p$  is the plasma frequency, given by  $\omega_p = (Ne^2/\epsilon_0 m^*)^{1/2}$ , where  $N$  is the free

charge carrier density,  $m^*$  the effective mass of the carriers,  $e$  is the electronic charge,  $\tau$  is the average time between two consecutive collisions of the charge carriers and  $\epsilon_0$  is the vacuum permittivity.

When the frequency of the incident electromagnetic radiation is much lower than the plasma frequency of the metal, its dielectric response can be approximated as relatively invariant with frequency. This is the case of noble metals like gold and silver at THz frequencies. At THz frequencies the imaginary component of the complex dielectric response of noble metals dominates over the real component. This is indicative of a high absorption constant of THz radiation in noble metals. High absorption constant indicates low skin depth, i.e., similar to the case of a good conductor. The skin depth at THz frequencies can be approximated by the following expression,

$$\delta = \frac{1}{\alpha/2} \approx \frac{c}{\sqrt{2\pi\sigma_0\omega}}, \quad (2.47)$$

where  $\alpha$  is the absorption constant and  $\sigma_0 = \omega_p \tau \epsilon_0$  is the Drude dc-conductivity under the approximation,  $\omega\tau \ll 1$  and  $c$  is the speed of light in vacuum. From Eq. (2.47), at 1 THz, the skin depth of gold is approximately  $\lambda/4000$  which is almost negligible. In this thesis, we largely deal with gold structures at THz frequencies. In view of previous arguments, gold can be approximated as a perfect electric conductor at THz frequencies. Thus, localized resonances in resonant gold structures can be described by multipolar antenna resonances at THz frequencies.

A typical example of a dipolar antenna is shown in the Fig. 2.10, illustrating the current, created by the motion of the charge distribution and the voltage distribution, created by the transient spatial density of the charges distribution. It is the frequency associated with the oscillatory motion of the free charges which is responsible for the far-field distribution from these structures. The potential, or the strength of the oscillations, determines the field distribution in the near-field. This results in the formation of near-field “hotspots” at positions where the concentration of charges are maximum, near the edges of the conductor for the resonant frequency. The maximum current is at the center of the rod, where the near-field intensity is the minimum.

Based on the fact that conducting structures can scatter and localize electromagnetic radiation, arranging these structures or simply bringing them close enough with respect to each other can result in the manipulation of fields around them. When the distinct modes of the electromagnetic fields overlap spatially and spectrally, they couple to each other. Efficient far-field coupling can be achieved through ordering the structures in a periodic lattice. This was first discovered in the year 1902, when Wood reported the formation of distinct dark and bright bands in the reflection spectrum of a diffraction grating[114]. The nature of these bands, however, were not understood and they came to be known as *Wood's anomalies*. Lord Rayleigh, came up with the explanation a few years later. He postulated that the anomalous distribution seen by Wood can be related to the condition where a diffracted order is radiated at an grazing angle to the surface of the grating[115]. In another paper [116], he derived the relation between the incident and the scattered wave vectors in a grating, which is known as the Rayleigh anomaly condition. Mathematically

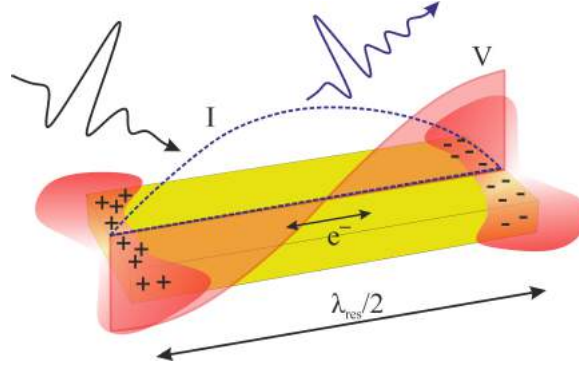


**Figure 2.10:** Schematic representation of a dipolar oscillation in a gold rod when illuminated by a THz radiation. The red and the blue curves indicates the voltage and current distribution respectively at the peak of one half cycle of the wave with resonant frequency. The near-field distributions are indicated in red “hotspots” and the radiated far-field is shown in blue transient.

this is as follows,

$$\bar{k}_{\parallel}^{out} = \bar{k}_{\parallel}^{in} \pm \bar{G}, \quad (2.48)$$

where  $\bar{k}_{\parallel}^{in}$  is the component of the incident field wave vector parallel to the grating, while  $\bar{k}_{\parallel}^{out}$  is the same for the outgoing wave and  $\bar{G}$  is the reciprocal lattice vector. Equation (2.48) is known as the *Rayleigh anomaly* (RA) condition. When we consider a sample of resonant scatterers in a periodic configuration, the Rayleigh anomalies enhance the radiative coupling between the scatterers. This coupling results in a modification of the resonant response of the individual scatterers into a collective resonant behavior that can be significantly different. In case of an array of resonant metallic particles, this is known as the *Surface Lattice Resonances* (SLR)[117–128] and are discussed in detail in Chapter 5. Besides modifying the spectral response of individual scatterers, SLRs enhance the local fields in the near-field region of the scatterers. Figure 2.11(s) illustrates the schematic of this mechanism.

Another way of manipulating local fields of individual scatterers is by coupling them in the near-field, i.e., by bringing them very close to each other such that the evanescent tails of the near-field distributions overlap with each other [129–131]. For efficient coupling, the distances between the individual scatterers has to be very small compared to the wavelength of the incident light. A system showing near-field coupling is demonstrated in Chapter 6. The schematic of near-field coupling is shown in Fig. 2.11(b).

## 2.2.4 Detection of local fields: near-field microscopy techniques

Near-field microscopy offers the possibility of detecting evanescent fields and, therefore breaking the diffraction limit. This implies that the mechanisms of interaction between light and matter at sub-wavelength scales can be visualized. This motivation has led to

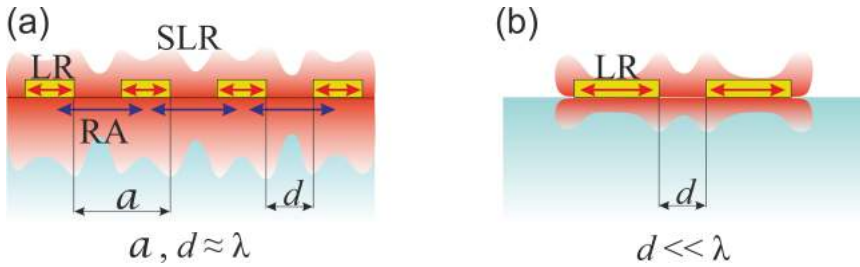


**Figure 2.11:** (a) Schematic representation of a surface lattice resonance. The red arrows indicate the localized resonances of the individual particles, the blue arrows indicate the radiative mode under the Rayleigh anomaly condition. The electromagnetic field distribution of the surface lattice resonance is shown in red. (b) Schematic representation of near-field coupling of resonant structures.

many complex instruments, which can capture the illusive near-field. The most challenging aspect of a near-field microscope, which made the instrumentation difficult to realize, is the coupling of source or detector to the sample which is to be imaged. This coupling is not an issue for the conventional far-field techniques as the light source or detection is not affected by the sample. The original proposition of a near-field optical microscope was given by Edward Hutchinson Synge in 1928 [132]. His idea for an instrument became the inspiration for modern scanning optical near-field microscopes. He proposed an illumination from a minute aperture in very close proximity to a sample, such that this illumination is not diffraction limited, as shown in Fig 2.12. The transmitted light is then collected by a microscope, and a photoelectric cell measures the intensity. In order to image the object the aperture can be moved laterally in small increments and the process can be repeated. Thus the resolution of the image should only be limited by the size of the aperture.

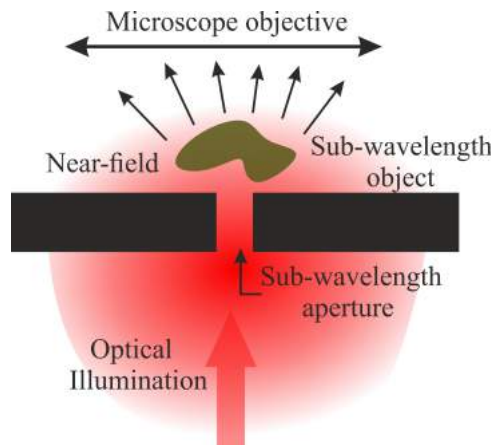


**Figure 2.12:** Schematic of the near-field microscope suggested by Synge in 1928

## 2.3 Near-field measurement techniques

Following up on the original ideas of Synge, successful experimental attempts to measure and characterize near-fields were reported in 1972 by Ash and Nicholls in the microwave regime [15]. They realized a microwave microscope with the spatial resolution of  $\lambda/60$ . Experimental techniques to observe the near-fields in the optical domain were realized in 1980s in a patent by Pohl and co-workers using an aperture based method [16]. This paved the way for more advanced techniques like the one introduced by E. Betzig using scanning fibers [17], photon scanning tunneling microscopy by three different groups in 1989 [133–135], near-field rendering of spatial maps of field distribution using heterodyne interferometric detection by M. Balistreri [136], light intensity measurement of propagating plasmon along nanowires by H. Ditlbacher [137], to name a few. Recent developments to study the individual components of the local fields near photonic and plasmonic structures were achieved both in optical and near-infrared frequencies [138–141].

Following the research at optical frequencies, there were significant advances in near-field microscopy at THz frequencies. The earliest study of THz near-field measurement was in 1998 when Hunche and co-workers demonstrated near-field imaging with broadband THz pulses by focussing the radiation on a tapered metal tip and scanning the sample in the near-field [142]. They showed a spatial resolution of up to  $\lambda/4$ . Many research groups around the world soon followed up with THz near-field techniques of their own. A few examples of the techniques developed are THz near-field imaging with optical gating beam on semiconductor wafer [143], apertureless THz near-field spectroscopy to measure temporal profile of the near-field pulse with spatial resolutions of 50 microns [144], apertureless THz microscopy with resolutions of 150 nm [145], THz nanoscopy of mobile charge carriers in nanodevices with resolutions of 30 nm with scattering from AFM tips [146]. Other techniques which were able to probe different spatial components of the near-field from sub-wavelength structures were also developed using electro-optic techniques on semiconductor surfaces [147, 148], photoconductive apertures [149] and photoconductive microprobe tips [150]. Some other notable techniques with similar capabilities were also developed [125, 151–153].

## 2.4 THz near-field micro-spectrometer

In this thesis, we developed a near-field micro-spectroscopy setup, shown in Fig 2.13, based on photoconductive microprobe probe tips, which are commercially available [150]. The setup is driven by a femtosecond IR oscillator operating at 800 nm with a pulse duration of 20 fs and a repetition rate of 80 MHz. The output train of pulses from this oscillator is divided in two beams. The first beam, which carries most of the power ( $\sim 350$  mW), goes through a delay stage and is incident on a photo-conductive (PC) antenna which generates broadband THz radiation [154]. This radiation is weakly focussed onto the sample position by a pair of off-axis parabolic mirrors. The other beam carries a small amount of power ( $\sim 5$  mW), and is used to bias the detector. This detector is a commercially available micro-probe-tip [150], which operates on the principle of photo-

conductive sampling [155], as explained in the previous chapter. The tip is a PC antenna downsized to sub-wavelength volumes ( $10 \mu\text{m}^2$ ). The orientation of the PC gap in the tip defines the electric near-field component that it probes. This is explained in detail in Chapter 3. The capabilities and uniqueness of this setup is explained in more detail in Chapter 3.

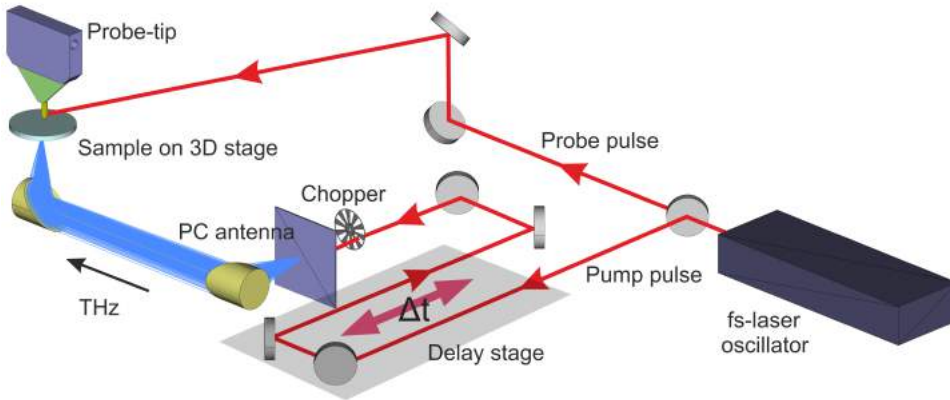


**Figure 2.13:** THz near-field micro-spectroscopy setup

The near-field micro-spectroscopy setup measures the electric field in the near-field region of a sample as shown in Fig. 2.14(a) for each position on the sample. This transient field is Fourier transformed to generate the spectral composition of the signal measured as shown in Fig. 2.14(b). Furthermore, the sample is mounted on a 3D stage which enables us to measure the near-field on all spatial positions on the sample on the near-field region. A typical measurement consists of such transients measured on a x-y plane in the vicinity of a sample at a fixed height ( $z=\text{const.}$ ). This forms a data cube of electric near-field slices as a function of spatial coordinates and time, which can be Fourier transformed to extract the frequency slices of amplitude and phase as a function of spatial coordinates. This is schematically shown in Fig. 2.14(c).

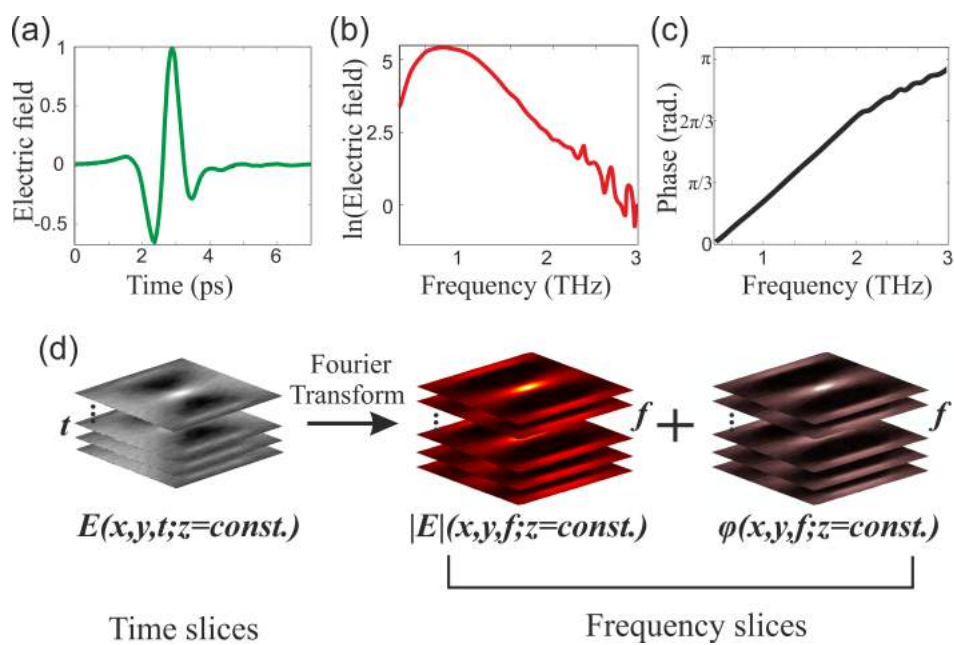


**Figure 2.14:** Schematic of the analysis of the data collected with the THz near-field micro-spectrometer. (a) shows the measured electric near-field transient at a point on the sample, (b) represents the electric field intensity spectrum of the transient, (c) the phase spectrum and, (d) represents the data cube measured and derived from a full measurement for many spatial positions on a sample.



## CHAPTER 3

# VECTORIAL MAPPING OF COMPLEX ELECTRIC NEAR-FIELD NEAR THZ RESONATORS

---

*Using micro-structured photo-conducting antennas, we demonstrate full vectorial mapping of the complex electric fields at subwavelength scales in the near-field region of a resonant structure at THz frequencies. The structure represents the simplest case of a resonator: a metallic rod. We show electric field amplitude as well as phase maps for the all the three field components at the dipolar resonance condition of the rod. The amplitude as well as the phase distributions are in excellent agreement with our physical understanding of local electric-field distributions in the vicinity of dipolar structures and are validated by numerical simulations. These measurements can be a platform for performance optimization of the emerging field of photonic and plasmonic devices with complex sub-wavelength structures at THz frequencies.*

### 3.1 Introduction

As explained in Chapter 2, the angular spectral decomposition of an electromagnetic wave leads to two terms: a collection of propagating plane waves (far-field) and a distribution of spatially inhomogeneous non-propagating evanescent waves (near-field). At sub-wavelength distances from the source, the contribution due to the near-field is significant compared to the far-field. These distances are referred to as the near-field region [77, 156]. The initial motivation to measure the near-field was an attempt to break the 'diffraction-limit' of far-field imaging [132]. This study led to the feasibility of accessing and probing directly the electromagnetic field formation near sub-wavelength structures. Advances in near-field microscopy opened the world of manipulation of light in sub-wavelength volumes leading to several promising applications in the field of photonics [157–162]. Attempts to measure and characterize near-fields were done first at optical frequencies, which paved the way for near-field detection techniques at THz frequencies [142, 144–150, 163–166].

Owing to the relatively long wavelengths of THz radiation ( $\sim 100$ 's of microns), the creation of highly confined THz local fields in small volumes is critical for enhancing the interaction of THz waves with matter. The use of resonant structures for this purpose has been the topic of many interesting studies, especially for spectroscopy of deep-subwavelength structures [126, 167–173]. For these studies, it is important that the vectorial electromagnetic fields around these resonant structures are fully characterized both in frequency and space to ensure optimal performance. This characterization becomes more relevant owing to the significant frequency shift between resonances measured in the far- and the near-field [174, 175]. This shift has been recently shown to reach values comparable to the line-width of the resonance at THz frequencies due to the Fano interference in the far-field between the incident and scattered fields [176]. Therefore, the sole characterization of the far-field is not sufficient to describe resonant THz structures.

In the past, several groups have shown vectorial mapping of in-plane electric near-fields in optical and infrared frequencies by scattering polarization resolved techniques [138–141]. These techniques offer a high spatial resolution but the detected field at different positions are a superposition of different field components [177]. Vectorial mapping of near electromagnetic fields at THz frequencies offers the potential to gather full information as local fields rather than intensity, which can be measured as a function of time. Several schemes have been developed for this purpose. Vectorial mapping of near-field components of resonant structures has been measured on top of non-linear crystals, using electro-optic detection [151, 178, 179]. This approach is limited by the necessity of having the sample on top of the high refractive index crystal and thus, modifies the intrinsic near-field distribution of the investigated structure. Another approach uses electro-optic crystals as external near-field probe [153]. This technique is limited by low sensitivity as well as partial invasiveness to the near-fields. Out-of-plane magnetic near-fields calculated from measurements of in-plane electric near-fields have been shown using photo-conductive antennas on substrates [125, 152]. Direct measurement of magnetic fields in the near-field region has also been demonstrated [180].

In this chapter, we use photoconductive switches (explained in Chapter 2) imprinted on 1- $\mu\text{m}$ -thin low-temperature-grown GaAs micro-probe tips [150], to measure all the individual components of the complex electric near-field in three dimensions near a gold rod resonant at THz frequencies. It has been already shown that these tips show negligible invasiveness to resonant structures [176, 181]. Also, as the signal-to-noise ( $\sim 10^4$  in intensity) and the rejection ratio for cross polarizations ( $\sim 10^3$  in intensity) in our measurements are high, we can characterize both the spatial distributions of spectral intensity and phase of all the electric field components with high accuracy. These results are in very good agreement with the basic understanding of local field distributions at resonances and are further validated by numerical simulations.

To demonstrate the spatial distribution of the near-field components of the electric field, we used the simplest sample geometry: a micro-rod resonant at THz frequencies. The sample consists of a rectangular rod made of gold on a quartz substrate. The dimensions of the rod are 100  $\mu\text{m}$  along the long axis and 40  $\mu\text{m}$  along the short axis. The thickness of the rod is 100 nm. The fabrication was done using UV lithography in combination with standard gold evaporation and subsequent lift-off techniques. A single rod was made on the substrate to avoid perturbation of the near-field due to the presence of other scatterers.

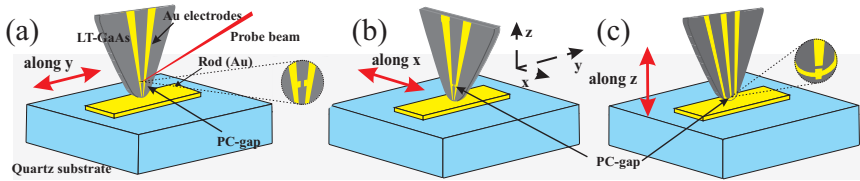


**Figure 3.1:** Schematic representation of the probe-tips (TeraSpike TD-800-X-HR, Protemics GmbH) for measuring the different near-field components. (a) shows the PC-gap oriented along the long axis (Y) of the rod. Zoomed image of the PC gap is shown. (b) shows the same probe-tip oriented along the X axis, and (c) shows another probe-tip (TeraSpike TD-800-Z-N, Protemics GmbH) for measuring the Z-component of the near-field. The red arrows indicate the orientations of the PC-gaps in the probe-tips and hence the measured field component of the electric near field. The sample is illuminated by a broadband THz source from below. The THz polarization is along the long axis of the rod in all the cases, i.e. along Y-axis.

## 3.2 Terahertz near-field imaging

The technique for measuring the THz electric near-field around the rod is explained in Chapter 2 in section 2.4. All the near-field measurements were done on a plane with tip-to-sample distance of 1  $\mu\text{m}$ . The polarization of the incident THz radiation was oriented along the Y axis. The long axis of the gold rod was also oriented with the Y-axis such that the length of the rod is parallel to the polarization of the THz beam. For measuring the in-plane (Y and X) field components of the electric field we used the same probe-tip (TeraSpike TD-800-X-HR, Protemics GmbH) in parallel and crossed configurations as

shown in Fig. 3.1(a) and (b). For measuring the out-of-plane (Z) component we used a different probe-tip (TeraSpike TD-800-Z-N, Protemics GmbH) which has the PC gap oriented along the Z axis as shown in Fig. 3.1(c). Figure 3.2(a) shows the different components of the electric field transients measured by the probe-tips as a function of time delay at one of the corners of the gold rod. The field strength for the Y component (green open circles) is the highest as the incident field is along Y-axis. The X-component (blue open triangles) of the electric field in the same figure is multiplied by a factor of 5 and the Z component (red open inverted triangles) by a factor of 10 to elucidate their temporal responses compared to the Y-component at the same position on the sample. Figure 3.2(b) shows the spectra derived from the transients of Fig. 3.2(a) by Fourier transformation. There is a clear resonant response at around 0.7 THz for all the field components. When the rod is illuminated by a broadband THz excitation, the charges near the surface of the rod are set into coherent oscillations. This forms a surface wave, which travels back and forth along the long axis of the rod (along Y). This oscillations of surface charges give rise to a scattered field as well as an evanescent distribution of local fields around the rod. The local fields around the rods are highly enhanced near the sharp corners of the rod due to a large density of surface charges (lightning-rod effect). The frequency response of the surface charges is shaped by the geometry of the rod (also by the intrinsic losses) which gives rise to the resonant behavior at a well defined frequency. The local- or near-field intensity reaches its maximum at approximately the wavelength that corresponds to twice the dimension ( $l$ ) of the rod which is oriented to the incident polarization. This is known as the  $\lambda/2$  resonance as shown in Fig. 3.2(b). Higher order resonances in the response (not shown here) are also generated following the progression  $l \approx n\lambda/2$  where  $n$  is the order of the resonance. As the polarization of the incident THz radiation is along the Y-axis and this sets the electrons into a coherent oscillation,  $E_y$  is the dominant field component near the corners of the rod (X-component of the electric near-field intensity has been multiplied by 100 and corresponding Z-component by 500). This behavior is elucidated later when we analyze the spatial maps of the different components of the near-field at resonance. Note, that the near-field spectra of the measured field components represent a product of response from the structure with the spectrum of the incident field as well as the response of the probe-tip itself. The pure spectral response from the structure can be extracted by referencing these measurements with similar measurements on a bare substrate under same conditions. However, measurements of orthogonal components of the near-field for a certain incident polarization on a bare substrate are physically meaningless as they vanish, i.e. the X- and the Z-components can not be referenced. In order to keep the definition of the near-field amplitude consistent, the Y-component was also not referenced. Furthermore, both the response of the probe as well as the substrate are non-dispersive in the bandwidth of interest, which means that the resonant behavior in the spectra of Fig. 3.2(b) are indeed due to the gold rod.

The physics behind the mechanism of the resonance can be best explained by the the spectral analysis of the data. As the near field transients are measured at all the points around the rod at a fixed sample-to-probe distance, the data extracted is in the form of a 3D matrix with in-plane spatial coordinates along the two axis and temporal delay along the third axis. Fourier transform allows us to get two more data-matrices of the electric

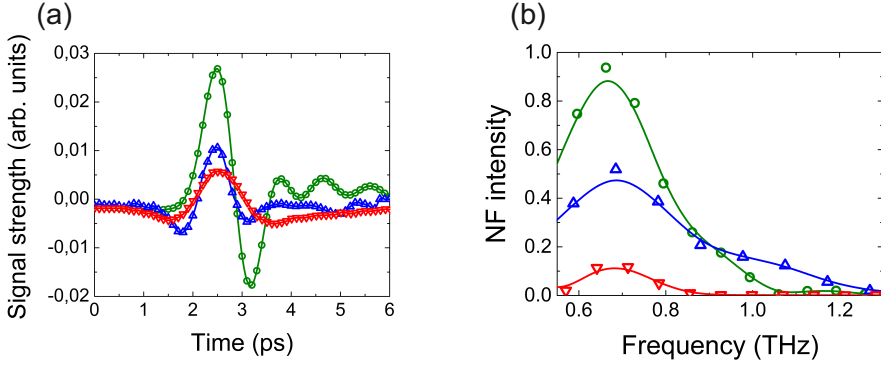


**Figure 3.2:** (a) Transient response of each component of the electric near-field  $1 \mu\text{m}$  above a corner of the Au rod when irradiated with broadband THz pulses. The green open circles shows the Y-component (parallel to incident polarization) of the detected electric field. In blue open triangles is the X-component (crossed with the incident polarization) and in red open inverted triangles is the Z-component (out-of-plane). The X-field is multiplied by a factor of 5 and the Z-field by a factor of 10. Symbols indicate measured data, whereas, the solid curves are guides to the eye. (b) Spectral response of three different electric near-field components in intensity. The color schemes are same as in (a). The X-component in this case has been multiplied by 100 and the Z-component by 500 to show their spectral behavior compared to the dominant Y-component.

field amplitude and phase as a function of spatial coordinates and frequency. We have obtained the spatial maps of the field amplitude and the phase at the resonance frequency for the three electric field components. These maps are shown in Fig. 3.3, where panels (a) and (d) represent the measured amplitude and phase of the Y-component of the electric near-field at 0.7 THz. Panels (b) and (e) show the maps of the X-component and (c) and (f) are the near-field maps of the Z-component. The boundaries of the rod are marked on Fig. 3.3 by the white dashed rectangles.

### 3.3 Numerical simulations

To verify our results, we have simulated, using the Finite difference in time domain method (FDTD), the local fields in the vicinity of a rod. The rod has the same dimensions as explained earlier and it is illuminated by a broadband THz pulse similar to the experiments. Gold at THz frequencies behaves almost like a perfect electric conductor. Therefore, in our simulation we define the material of the rod as a perfect electric conductor. The simulation volume, containing a single rod, has boundaries that are perfectly matched in impedance to the environment. Figure 3.4 shows the spatial distributions of amplitude ((a), (c), (e)) and phase ((b), (d), (f)) of the different components of the simulated electric field at the resonant frequency of 0.7 THz at a height of  $1 \mu\text{m}$  above the rod. The simulated field profiles qualitatively match the measured profiles. However, the features seen in the simulated field distributions are much sharper. This

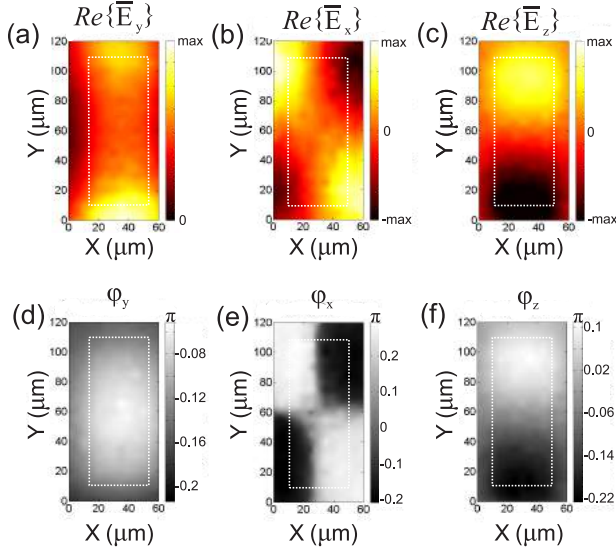


**Figure 3.3:** (a), (b) and (c) show the spatial distribution of the real component of the different electric near-field components (Y, X and Z respectively) around the gold rod at the resonant frequency, i.e. 0.7 THz. Panels (d), (e) and (f) show the spatial distribution of phase at the resonant frequency around the gold rod. The dotted white rectangles indicate the boundaries of the gold-rod.

discrepancy is due to the fact that in the simulations we used a field monitor which has an infinitesimal resolution (10 nm), whereas, the micro-probe tips in the measurements have a finite resolution ( $\sim 10 \mu\text{m}$ ). Hence, in the measurements, the fields are averaged over a larger sampling area, which results into a smeared out signal, i.e. the real field distributions are convolved with the spatial resolution of the tip.

To elucidate further the unique amplitude and phase distributions associated with the individual field components near the rod, we have simulated the same rods as before, however, this time illuminated by a monochromatic THz light (See Fig. 3.5). The frequency of this radiation was chosen to be precisely the resonance frequency of the rod, i.e. 0.7 THz. We define two electric field monitors: the first detects the field in the XY plane at a height of  $1 \mu\text{m}$  above the rod, while the second detects the field in the YZ plane in the middle of the rod, i.e.  $X=0$ . The rod is denoted by the green rectangle in the in-plane (XY) and by the green line in the out-of-plane (YZ) electric field maps. The white arrows represents the electric field vectors. The magnitude of the local field intensity is shown by the color scale. We define the two times,  $t_1$  and  $t_2$ , which represents two phases of the incident field at which the incident field amplitude reaches the positive and negative maxima in adjacent half cycles of one oscillation. Figures 3.5(a) and (c) represent the in-plane and out-of-plane electric field distributions respectively in the vicinity of the rods at  $t = t_1$ . In Figs. 3.5(b) and (d) the same information is shown for  $t = t_2$ . If we project the electric field vectors in Figs. 3.5(a) and (b) along X and Y, it becomes evident that  $E_y$

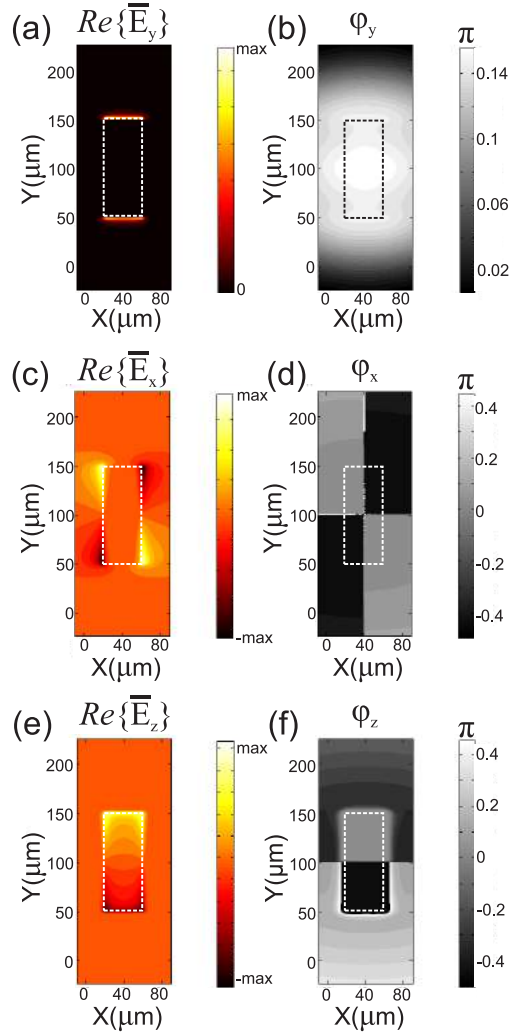


**Figure 3.4:** (a), (c) and (e) show the spatial distribution of the simulated real component of the different electric near-field components (Y, X and Z respectively) around the perfect electric conductor rod at the resonant frequency, i.e. 0.7 THz. Panels (b), (d) and (f) show the spatial distribution of simulated phase at the resonant frequency around the rod. The dotted rectangles indicate the boundaries of the rod.

at both the ends of the rod have equal magnitude and direction, which gets shifted by  $\pi$  radians in the next half cycle of the illuminating field. This explains the measured field distribution of Fig. 3.3(a). The uniform phase distribution of Fig. 3.3(d) is also described by the simulations because for all the edges of the rod  $E_y$  oscillates in-phase with the driving field. We see in Fig. 3.5(a) that the projection of the electric field vectors along X results in opposite orientation of  $E_x$  in the adjacent corners of the rod. This explains the formation of electric field 'hotspots' of opposite signs in the adjacent corners of the rod as shown in Fig. 3.3(b).  $E_x$  at the four corners of the rods oscillate with the driving field, but phase-shifted with respect to the adjacent corners, which gives rise to the phase distribution of  $E_x$  in Fig. 3.3(e). It is worth mentioning that along the long and the short axes of the rod, the

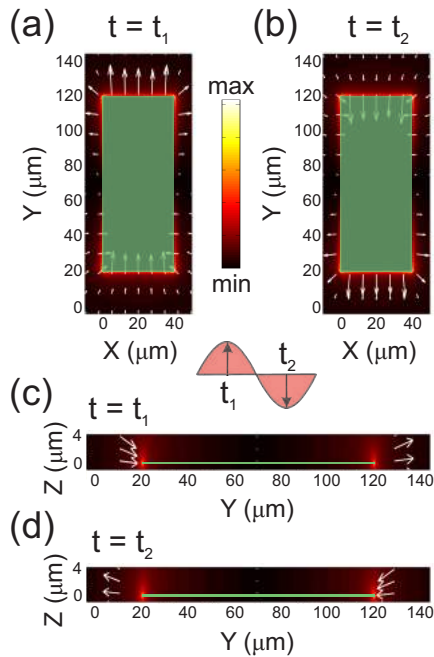


**Figure 3.5:** Simulated electric field distribution near a gold rod (in green). The times  $t_1$  and  $t_2$  indicate the phase of the incident electric field at which the field amplitude reaches the positive and negative maxima, respectively. Panel (a) shows the in-plane electric field vectors (white arrows) thereby elucidating the in-plane field components,  $E_x$  and  $E_y$ , at  $t = t_1$ . Panel (b) shows the in-plane distribution of the electric field vectors at  $t = t_2$ . Panel (c) and (d) shows the out-of-plane (cross-cut through the long axis of the rod) electric field vectors showing the  $E_y$  and  $E_z$  along the rod at  $t = t_1$  and  $t = t_2$ , respectively. The color scale indicates the intensity of the local field in the maps.

magnitude of  $E_x$  goes to zero. The phase is not defined along these axes, which define lines of phase singularities. The phase singularity lines are clearly seen in the measurements of Fig. 3.3(e).

By analyzing Figs. 3.5(c) and (d), with similar reasoning, we can explain the field and phase distributions of  $E_z$  in Figs. 3.3(c) and (f). Again we see the formation of a phase

singularity along the short axis of the rod. The field profiles in the measured maps in Fig. 3.3 are in excellent agreement with the explanation based on the simulated maps in Fig. 3.5

## **3.4 Conclusions**

In this chapter, we have shown a complete characterization of near-fields generated near a resonator at THz frequencies. The field profiles were explained and supported by numerical simulations. The full vectorial characterization of the THz near-field will serve for the optimization of emerging photonic and plasmonic devices at THz frequencies.



## CHAPTER 4

# LARGE NEAR-TO-FAR SPECTRAL SHIFTS FOR THZ RESONANCES

---

*We have performed far-field extinction measurements and near electric field measurements on gold bowtie resonators at THz frequencies. These measurements show a very large shift between the resonant frequencies of the near-field and the far-field spectra. We used the established damped-driven harmonic oscillator model for resonators to model the far-field response of the bowtie resonators from the near-field spectrum and show that there is a large discrepancy between the predicted and measured far-field response. We are able to explain this discrepancy by improving the oscillator model with a Fano model. This large shift makes the prediction of the near-field response of resonant structures at THz frequencies very imprecise, provided that only information of the far-field response is available and establishes the necessity of measuring near-fields for a correct and accurate characterization of these structures.*

## 4.1 Introduction

We have already seen in Chapter 2, that when metallic structures are illuminated with electromagnetic radiation, the free charges are driven into a periodic motion following the excitation field. This oscillation of free charges can result into the generation of highly enhanced and confined local electric fields in the vicinity of the structure that are referred to as near-field 'hotspots' [158]. At visible and infrared frequencies the hotspots are caused by localized surface plasmon polaritons or the coherent oscillation of charges in the metallic particle. The generation of these hotspots enables the manipulation of electromagnetic fields in deep sub-wavelength volumes [157, 159, 160, 162], which opens up the possibility of imaging and spectroscopy of small objects [17, 182–185]. This concept has been also proposed and demonstrated at THz frequencies [167, 186–189]. Therefore, there is the necessity of optimizing the intensity of confined fields as well as the frequency response for real applications, which is achieved by designing the structure in such a way that it is resonant at the frequency of interest. This resonant behavior is usually characterized with far-field measurements.

Since the interaction of the near-fields with sub-wavelength objects determines the spectral response of the system, it is of utmost importance to characterize the near-field response of the resonant structures. The relation between the near-field response of a structure and its far-field spectrum has been the subject of several studies that have consistently reported a small, yet distinct shift between the near- and far-field resonant frequencies [175, 190–193]. The origin of this shift is ascribed to the intrinsic damping of the structure and has been modeled using the damped-driven oscillator model [192]. Zuloaga *et al.* have shown that the oscillator amplitude is related to the induced near-field by the surface plasmon polariton and the oscillator dissipated power to the far-field extinction. In a more recent publication by Kats *et al.* [194], it is shown that there are two distinct loss channels by which the localized plasmon mode decays: internal damping via free carrier absorption and emission of radiation or scattering to free space. Using this simple model it was shown that the calculations were in excellent agreement with the numerical simulations in the infrared range. Thus, this result suggests the conjecture that we can accurately predict the near-field spectral response from a far-field measurement, which is intrinsically much easier to perform.

In this chapter we show experimentally that there can be an anomalously large shift between the near- and far-field resonances, which can not be explained entirely by the oscillator model. We have performed measurements of the THz near-electric field and of the THz far-field extinction of the gold bowtie resonators. Our results show that the frequency shift is comparable to the FWHM of the resonance. Even though our findings are in qualitative agreement with previous studies, the observed spectral shift is significantly larger than what has been previously reported and calculated. We ascribe this discrepancy to the fact that the measured far-field is not just the scattered field from the structures but its interference with the incident field. This spectral interference, described by a Fano model,[195] explains the total response of the system and should be taken into account when designing plasmonic structures for subwavelength spectroscopy.

## 4.2 Sample description

To study the interaction of THz waves with scattering structures, both in the near- and far-field, we use bowtie resonators made of gold which are designed to resonate at THz frequencies. A bowtie resonator consists of two isosceles triangles with pointed tips facing each other and separated by a small gap. These structures are interesting because they combine two distinct electromagnetic effects: the lightning rod effect due to the sharp metallic tips, which leads to high electric field accumulation in the gap and resonant response to the driving field which results from the size and shape of the bowtie. As a result, they do not only create highly enhanced and localized fields in the gap between the two triangles [187, 196–199] but also give precise spectral and spatial control over the response with relatively large bandwidths [200]. These structures have been used in the optical range to study effects like single molecule fluorescence [197], two-photon photoluminescence [196], surface-enhanced Raman scattering [201] or as sensors in the THz regime [167].

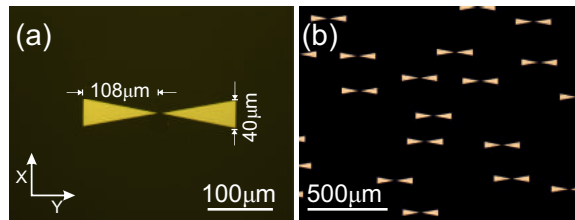


**Figure 4.1:** Optical microscope images of two samples. (a) shows a single bowtie resonator on a quartz substrate, and (b) shows a random array of resonators on a quartz substrate.

The gold resonators were fabricated on quartz substrates using e-beam lithography in combination with standard gold evaporation and lift-off process. Both triangles of the bowtie are 108 μm long with a base of 40 μm each and a gap of 5 μm between them as shown in Fig. 4.1(a). The bowties are ~100 nm thick. In this work, we have used two different samples. For the near-field measurements, we have fabricated single isolated bowtie structures, as shown in Fig 4.1(a), to avoid any distortion of the near-field signal by neighboring resonators. For measuring the far-field response we have made a random array of bowties (surface filling fraction 5%) with the same orientation of the long axes, so that all of them are aligned with the polarization of the driving THz field. A microscope image of the sample used for the far-field measurements is shown in Fig. 4.1(b). The random spatial distribution of the bowties cancels out the effects of radiative coupling between neighboring structures. Moreover, the resonators were placed sufficiently far from each other to avoid any significant near-field coupling between them.

The measurement of the near-field was done with the THz near-field microspectrometer as explained in Chapter 2 section 2.4 at a distance of 1 μm above the gap between the bowtie triangles. The far-field measurements were done with conventional electro-optic sampling techniques, also explained in Chapter 2.

### 4.3 Experimental results

We define two quantities for comparing the near-field to the far-field measurements. First, the near-field intensity spectrum,  $\mathcal{S}_{NF}$ , of the bowtie resonator is defined as,  $\mathcal{S}_{NF}(\bar{r}, \nu) = \left| \frac{E^{NF}(\bar{r}, \nu)}{E_{ref}^{NF}(\bar{r}, \nu)} \right|^2$ , where  $E^{NF}(\bar{r}, \nu)$  is the electric near-field at frequency  $\nu$  and position  $\bar{r}$  in the proximity of the bowtie resonator and  $E_{ref}^{NF}(\bar{r}, \nu)$  is the electric field at the same position and frequency but without the resonator. For now, we define this quantity at the gap between the triangles of the resonator. The second quantity is the far-field extinction spectrum,  $\mathcal{S}_{FF}$ , of the sample. The extinction is defined as  $\mathcal{S}_{FF}(\nu) = 1 - \left| \frac{E^{FF}(\nu)}{E_{ref}^{FF}(\nu)} \right|^2$ , where  $E^{FF}(\nu)$  is the transmitted electric field through the sample with the random array of the bowtie at frequency  $\nu$  and  $E_{ref}^{FF}(\nu)$  is the transmitted field without the bowties, i.e. the bare substrate.

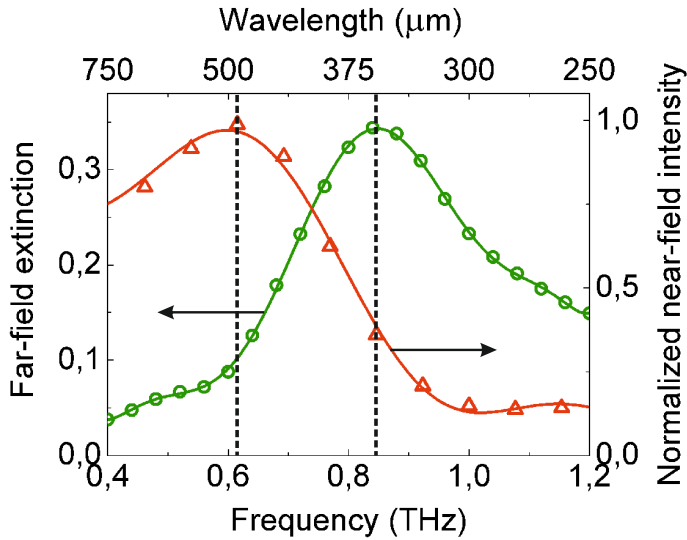


**Figure 4.2:** Near-field spectrum measured at the gap of a gold bowtie resonator (red triangles) and far-field extinction spectrum (green circles). The solid curves are guide to the eye. The vertical dashed lines indicate the resonant frequencies in the near- and far-field.

The measured near- and the far-field spectra are shown in Fig. 4.2. The triangles represent the near-field spectrum in the gap of the single bowtie resonator at a height of  $1 \mu\text{m}$  above the substrate and the circles correspond to the far-field extinction of the random array of bowtie resonators. Both spectra show a resonant behavior but not at the same frequencies. For the near-field spectrum, the resonant frequency is at  $0.62 \text{ THz}$ . The far-

field spectrum is remarkably blue-shifted from the near-field, with the resonant frequency at 0.85 THz. As it is discussed in the following section, the observed shift in our measurements can not be explained by the extensively used driven-damped oscillator model that approximates the response of the bowtie [191, 194].

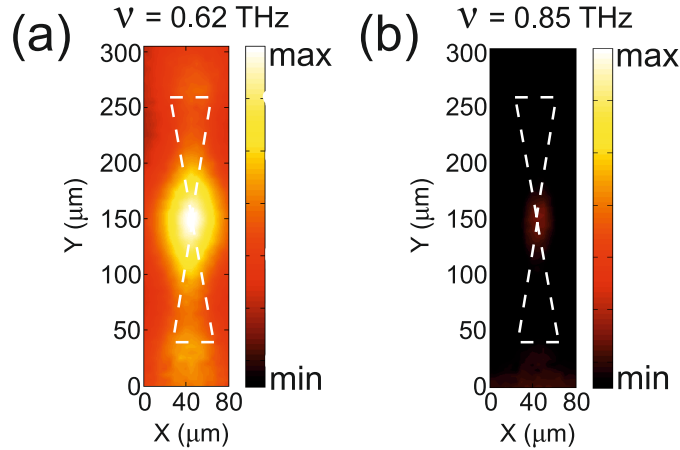


**Figure 4.3:** (a) Electric field intensity map measured at 0.62 THz and at a height of  $1\ \mu\text{m}$  above the bowtie resonator. (b) Electric field intensity map at 0.85 THz. The color scales are kept the same. In both panels the dashed lines indicate the boundaries of the bowtie resonator.

To investigate the spectral properties of the near-field around the bowtie resonators, we have measured spatial maps of the near-field at two different frequencies marked by the dotted lines in Fig. 4.2. The first line at 0.62 THz indicates the resonant frequency of the near-field and the second line at 0.85 THz corresponds to the resonant frequency of the far-field spectrum. Figure 4.3 shows the spatial maps of near-field intensities around the bowtie resonator at these frequencies. The color scale is kept the same in both the measurements to facilitate a direct comparison. These measurements show the local intensity enhancement in the gap of the bowtie at 0.62 THz (Fig. 4.3(a)). The sharp tips give rise to localized electromagnetic fields, whereas, the spectral resonance due to the dimensions of the bowtie enhances these fields. The field is pronouncedly less enhanced at 0.85 THz (Figure 4.3(b)) inspite of this being the resonant frequency of the far-field.

## 4.4 Numerical Simulations

We have performed numerical simulations using the Finite-Difference in Time-Domain method (FDTD) to model the response of a single bowtie resonator. Since gold is a very good conductor at THz frequencies we can approximate the material as a perfect electric conductor. The excitation is done with a broadband THz source similar to the experiments. The simulation volume contains a single bowtie resonator and the boundary

conditions are perfectly impedance matched layers to the surroundings. Both the near-field and the far-field of the bowtie are calculated by referencing the power of the total field by the power of the total field without the resonator. Similar to the experiments, the illumination is done from the side of the quartz substrate.

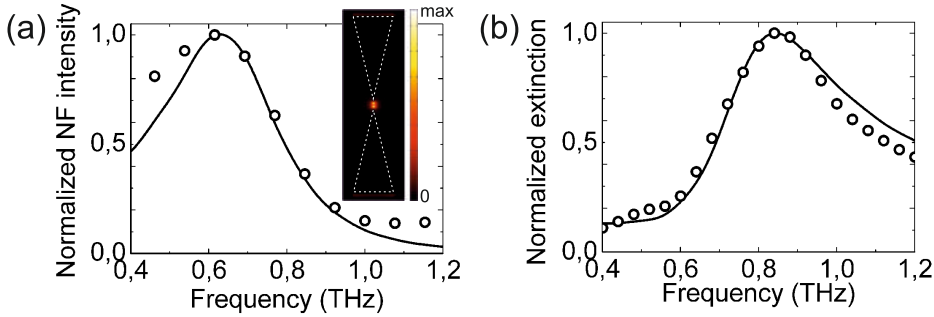


**Figure 4.4:** (a) The circles represent the measured near-field spectrum of the bowtie resonator on the gap between the two triangles at a height of  $1 \mu\text{m}$ , while the solid black curve is the simulated spectrum. The inset shows the near-field intensity map at 0.62 THz. (b) The circles represent the extinction spectrum of the random array of bowtie resonators and the solid black curve is the simulated far-field extinction spectrum.

We have simulated the far-field extinction spectrum and the near-field intensity spectrum at a height of  $1 \mu\text{m}$  above the resonator and at the center of the gap. Figure 4.4(a) displays the measured near-field (open circles) together with the simulation (solid curve). The experimental data and the simulation results are in an excellent agreement. From this result we can conclude that the probe-tip used for the measurements does not perturb the near-fields significantly. The inset of Fig. 4.4(a) illustrates the near-field intensity map at the resonance frequency of 0.62 THz. The maximum enhancement in the near-field intensity is, as expected, in the gap. Figure 4.4(b) shows the measurements (open circles) and the simulations (solid curve) of the far-field extinction, illustrating also the excellent agreement between the measurement and the simulation. The small discrepancy at high frequencies is most likely due to the fact that the experiments were performed with a weakly focused beam, whereas in the simulations a perfect collimated beam is used. Also we have used perfect electric conductor instead of gold in the simulations.

## 4.5 Driven-damped Harmonic Oscillator Model

The relation between the near- and the far-field response of resonant metallic structures has been approximated in the literature by driven-damped harmonic oscillator model. This analogy is often justified by the fact that the dynamics of free electrons in a conducting structure under the influence of a driving electric field follows an harmonic oscillation which is damped by Ohmic losses in the metal and by radiation damping from the accelerated charges. The resonant nature of the harmonic oscillator is determined primarily from the geometry of the structure. The oscillatory motion of the electrons in the

bowtie can be affected due to the capacitive coupling between the two resonant elements of the bowtie resonator, i.e., the gold triangles. A comparison between the simulations of individual triangles of the bowtie (not shown here) with the whole bowtie structure establishes that although there is a very weak coupling between the triangles of the bowtie, both responses are similar. Thus, without the loss of generality we can approximate the bowtie resonator as a single damped oscillator.

The spectral amplitude of the near-field close to the gap of the bowtie depends on the localization of charges accumulated at the two tips of the bowtie structure. Due to the symmetry of the structure, we can assume that both charge distributions are the same. Using the model described in Refs. [191] and [194] we can describe the motion of free charges using the equation of motion of a damped harmonic oscillator,

$$\frac{d^2Q}{dt^2} + 2\pi\nu_0\Gamma_a \frac{dQ}{dt} + (2\pi\nu_0)^2 Q = A_0(\nu)e^{-2\pi i\nu t} + 2\pi\nu_0\Gamma_s \frac{d^3Q}{dt^3}, \quad (4.1)$$

where  $Q(\nu, t)$  is the charge distribution as a function of time,  $A_0(\nu)$  is the harmonic driving field,  $\nu_0$  is the natural frequency of the oscillator,  $\Gamma_a$  is the internal damping constant and  $\Gamma_s = (1/\nu_0)Q_{tot}^2/6\pi\epsilon_0c^3$  is the radiation reaction coefficient also known as Abraham-Lorentz force, which represents the force that the free charges feel when they emit radiation [202]. The  $1/\nu_0$  is the scaling factor and  $Q_{tot}$  is the total number of free charges contributing to the damped oscillation. The value of  $Q_{tot}$  is estimated from the number of free electrons present in the structure, which is calculated by taking into account the free-electron density of gold ( $\mathcal{N}_{Au} = 5.9 \cdot 10^{22} \text{cm}^{-3}$ ) and the effective volume of the resonator by considering the penetration of the driving THz electric field is approximately equal to the height of the bowtie resonators. The harmonic charge oscillation is determined by solving Eq. (4.1) and is given by,

$$Q(\nu, t) = \sqrt{\mathcal{S}_{NF}(\nu)} e^{-i(2\pi\nu t + \phi(\nu))}, \quad (4.2)$$

where,

$$\mathcal{S}_{NF}(\nu) = \left| \frac{1}{\sqrt{(2\nu\nu_0(\Gamma_a + \nu^2\Gamma_s))^2 + (\nu^2 - \nu_0^2)^2}} \right|^2, \quad (4.3)$$

is the frequency dependent near-field intensity response with  $\Gamma_a + \nu^2\Gamma_s$  as the frequency dependent damping term and,  $\phi(\nu)$  is the corresponding phase response of the damped harmonic oscillator, both referenced with respect to the source.

By fitting the calculated  $\mathcal{S}_{NF}(\nu)$  to the near-field measurements as shown in Fig. 4.5(a), we can extract the natural frequency and damping constant of the oscillator, which are  $\nu_0 = 0.683 \pm 0.004$  THz and  $\Gamma_a = 0.302 \pm 0.018$  respectively. With these parameters the harmonic oscillator model fits excellently the experimental near-field intensity.

The time averaged scattered and absorbed power spectra by the oscillator can be cal-

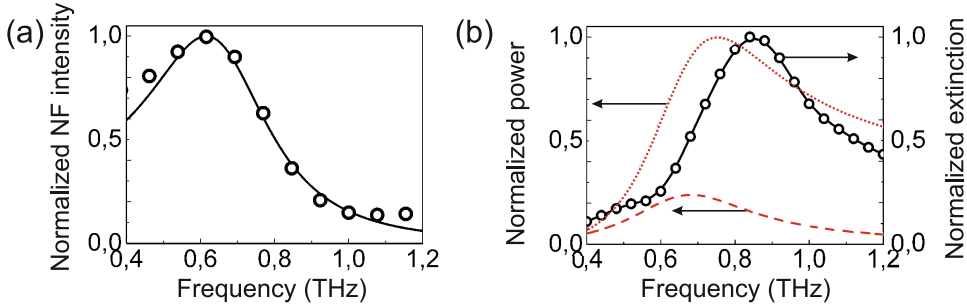


**Figure 4.5:** (a) The open circles represent the measured normalized near-field intensity, while the solid line is the fit to the measurements using the damped oscillator model. (b) Absorption and scattering spectral powers calculated from the harmonic oscillator model using the same parameters as in (a). The red dotted curve shows the scattering spectrum and the absorption spectrum is shown by the red dashed curve. Both the scattering and the absorption spectra have been normalized to the maximum of the scattering spectrum. The absorption spectrum is multiplied by a factor of 10 after normalization to elucidate its spectral response. The black line with circles represents the measured extinction spectrum from the random bowtie sample normalized to its maximum.

culated using the following expressions [194],

$$P_{abs}(\nu) = \nu^2 v_0 \Gamma_a \mathcal{S}_{NF}(\nu), \quad (4.4)$$

$$P_{scat}(\nu) = \nu^4 v_0 \Gamma_s \mathcal{S}_{NF}(\nu). \quad (4.5)$$

These spectra are shown in Fig. 4.5(b) with a dashed (absorption) and dotted (scattering) red curves, where we can appreciate that both the absorption and scattering spectra are blue-shifted with respect to the near-field intensity spectrum. The absorption spectrum peaks at the natural frequency of 0.68 THz, whereas the peak of the scattering spectrum is around 0.75 THz. Similar shifts have been reported in Ref. [194]. The use of a good conductor at THz frequencies is manifested in the fact that the spectral absorption is far lesser than the scattering. Gold behaves close to a perfect electric conductor in this frequency range and the absorption is low. Thus, we can conclude that the extinction spectrum of these structures in the far-field is dominated by scattering.

If we compare both the measured extinction (black circles in Fig. 4.5(b)) and the calculated scattering (red dotted line), we see a discrepancy in the resonant frequencies. The resonance of the scattering spectrum is at 0.75 THz, whereas the resonance of the extinction spectrum is at 0.85 THz. A quantitative description of this discrepancy is given in the next section.

## 4.6 Fano model

In order to explain the discrepancy between the experimental extinction and the oscillator model, we need to consider the incident field in the extinction. The incident field that is

not perturbed by the bowtie, interferes with the scattered far-field defining the extinction. This interference is not considered by the simple harmonic oscillator model and it is the origin of the discrepancy between this model and the extinction measurements. This interference effect can be described with a Fano model[195, 203], which defines a distinctly asymmetric line-shape with the functional form

$$F(\nu) = \frac{(q\nu_D\Gamma + \nu - \nu_D)^2}{(\nu - \nu_D)^2 + \nu_D^2\Gamma^2}, \quad (4.6)$$

where  $\nu_D$  and  $\Gamma$  are the frequency and line-width of a discrete state with a Lorentzian resonance profile that interferes with a continuum. The phenomenological shape parameter,  $q$ , is defined as the ratio between spectral amplitude of the discrete state and the continuum. In the limit  $|q| \rightarrow \infty$  the resonance is dominated by the lineshape of the discrete state (Lorentzian resonance), whereas at values close to unity ( $q \sim 1$ ) the discrete state and the continuum have equal strengths and the resonance profile shows an asymmetric lineshape similar to the one observed in the far-field extinction spectrum of the bowtie resonators (Fig. 4.2).

In the far-field extinction measurements the measured quantity is the total field, which corresponds to the interference of the scattered (discrete state) and the incident field (continuum). Therefore, it is expected that these fields give rise to a Fano-like resonance. The pronounced shift of the resonance frequency can be ascribed to the relative strength of the incident field in the interference effect.

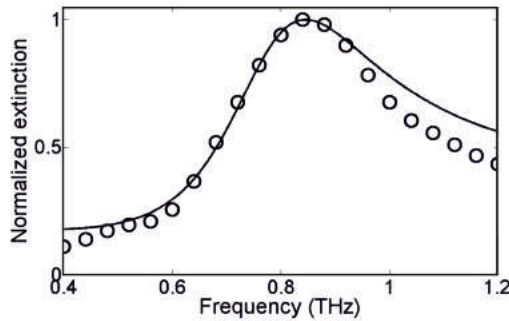


**Figure 4.6:** The black circles represent the measured and normalized extinction spectrum, while the solid line is a Fano fit to the measurements using the Fano model.

To verify the asymmetric nature of the far-field resonance and the consequent shift of extinction peak from calculated values, we have fit Eq.(4.6) to the measured extinction spectrum using the parameters extracted from the fit of the oscillator model to the near-field intensity spectrum, i.e.,  $\nu_D = 0.75$  THz (the resonant frequency of the scattering spectrum) and  $\Gamma = (\nu_0/\nu_D)(\Gamma_a + \nu^2\Gamma_s)$  (the frequency dependent damping term from the oscillator model with proper scaling factor) with  $q=2.02\pm 0.05$  as the only fit parameter. This result is shown in Fig. 4.6, where the circles illustrate the far-field extinction measure-

ments and the solid curve is the fit. The small deviation of the fit at high frequencies can be attributed to the approximation of the broad THz source as a continuum.

The relatively low value of  $q$  obtained from the fit indicates that the transmitted unperturbed field amplitude is marginally smaller than the scattered field by the bowtie. With this value of  $q$  the anomalous shift of the resonant frequency in the experiments can be explained. This shift is related to the ratio between the field strengths of the scattered and the incident fields, which depends on several factors. The most important one is the ratio between the total spectral powers integrated over all frequencies of the scattered and the incident field. The filling fraction of the bowtie resonators forming the sample also determines the ratio of the scattered to incident fields, and as a result, contributes to this Fano-like resonance and the consequent anomalous shift. Therefore, the far-field spectrum depends not only on the size and shape of the resonant structures and on their surface filling fraction of the sample, but also on the properties of the incident field.

The model presented above should be valid in all frequency ranges provided that material resonances are far from the spectral window of interest. However, this spectral interference effect should not affect substantially the spectrum of the near-fields in the confined hotspots mostly due to the fact that the electric fields in these regions are enhanced with respect to the incident field amplitude, hence approximating the condition  $q \rightarrow \infty$ . In this limit, the spectrum is dominated by the lineshape of the near-field and the measured near-field resonance will be at the same frequency as the predicted resonance by the oscillator model. This results establishes the necessity of measuring the near-field for an accurate characterization of resonant structures.

## 4.7 Conclusions

In this chapter we have shown that the far-field extinction spectrum of resonant structures at THz frequencies can have very large spectral blue-shifts with respect to the near-field intensity spectra. These shifts can be comparable to the FWHM of the resonance and can not be solely attributed to the intrinsic nature of the structures. Rather, the incident field plays an important role in defining the far-field spectral response of these structures. The large shifts can be explained analytically by using a Fano model that improves the driven-damped harmonic oscillator model extensively used to describe these structures. An important consequence of these results is that the characterization of resonant structures based solely on their far-field response can lead to misleading results that suggest field enhancements at frequencies at which the near-field is not changed significantly. Therefore, near-field measurements are necessary for an accurate description of resonant structures.

## CHAPTER 5

# DIFFRACTION ENHANCED TRANSPARENCIES AND SLOW THZ LIGHT

---

*In this chapter we demonstrate that a periodic lattice of detuned resonators can suppress the THz extinction at the central resonant frequency, leading to an enhanced transparency due to diffraction. The system consists of metallic rods of two different sizes, each of them supporting a strong half-wavelength ( $\lambda/2$ ) resonance, which are spatially displaced within the unit cell of the lattice. Using a coupled dipole model we show that the Diffraction Enhanced Transparency (DET) window has its origin in the interference between two surface lattice resonances, arising from the diffractively enhanced radiative coupling of the  $\lambda/2$  resonances in the lattice. Group-index measurements show that the THz field is strongly delayed by more than four orders of magnitude at the transparency window. Since DET does not involve the near-field coupling of resonators, the fabrication tolerance to imperfections is expected to be very high. This remarkable response renders these systems as very interesting components for THz communication.*

## 5.1 Introduction

Small metallic particles are among the simplest electromagnetic resonators. The resonances in these scatterers depend on the particle size, shape, orientation and material [204], and are usually broad due to radiative losses [205]. Ensembles of scatterers have properties that depend on the individual scatterers, as well as their relative arrangement. As shown in Chapter 2, bringing two metallic nanoparticles close together in dimer [206–208] or more elaborate [209] configurations can have a significant effect on the resonance frequency due to overlap of the local electromagnetic fields and consequent coupling between them. An important recent development in nanophotonics involves the generation of transparency windows induced by coupling of electromagnetic resonances [210–212]. This phenomenon usually involves a bright (dipolar) resonance that can couple to the radiation field and a dark (multipolar) resonance that couples to the bright resonance through its near field. [211] The coupling and interference of the two resonances leads to a frequency window in which the transmission is close to unity, while local fields are enhanced [213, 214]. These transparency windows are analogous to the electromagnetically induced transparencies (EIT) observed in atomic systems coupled to light fields [215]. The most important characteristic of these systems is that they can slow light to extremely low group velocities while having a transmission close to unity. Bozhevolnyi and coworkers have recently demonstrated the existence of a transparency window in the transmission spectrum of a system of two coupled particles of different dimensions, such that their dipolar resonant frequencies are detuned from each other at optical frequencies [216–218]. The mechanism leading to this transparency window is the radiative coupling between the two resonators and the destructive interference of the electromagnetic fields radiated into the far-field, and can be described as a coupled resonator induced transparency [219, 220]. Other examples include resonators coupled to a waveguide [221, 222], coupled microcavities [223] and ring resonators [224].

In this chapter, we demonstrate a spectral transparency window at THz frequencies with nearly perfect transmission in a periodic lattice of metallic rods with different dimensions. In contrast to previous works on detuned resonant particles, [216–218] we consider here a periodic lattice of detuned resonators, which supports surface lattice resonances (SLRs). As explained earlier in Chapter 2, these resonances are the result of the enhanced radiative coupling of the localized resonances in the individual particles through diffraction orders in the plane of the array (Rayleigh Anomalies [117–128]). Periodic arrays of detuned dipoles have been recently considered by Humphrey et. al. as a means to reduce the line-width of surface lattice resonances [225]. Our experimental results show a highly enhanced group-index, i.e., reduced group velocities, in the transparency window. Since the periodic arrangement of particles are responsible for the enhanced transparency of the sample, we term this phenomenon as diffraction enhanced transparency (DET). These results are explained with a coupled dipole model, which describes the system as interfering SLRs. Slow THz light has been reported in several works [226–229]. In contrast to these works, our system of detuned-dipoles shows a simple approach to engineer frequency selective transparency windows with very large transmission and group velocity reduction. The group velocity reduction is significantly larger than in plasmonic induced trans-

parency systems [210, 211, 228]. The enhanced reduction of group velocity is a result of DET not relying on near-field coupling, but on the interference of surface waves, as shown in the chapter. These remarkable properties make these arrays interesting components for the emerging field of THz communication.

## 5.2 Sample description

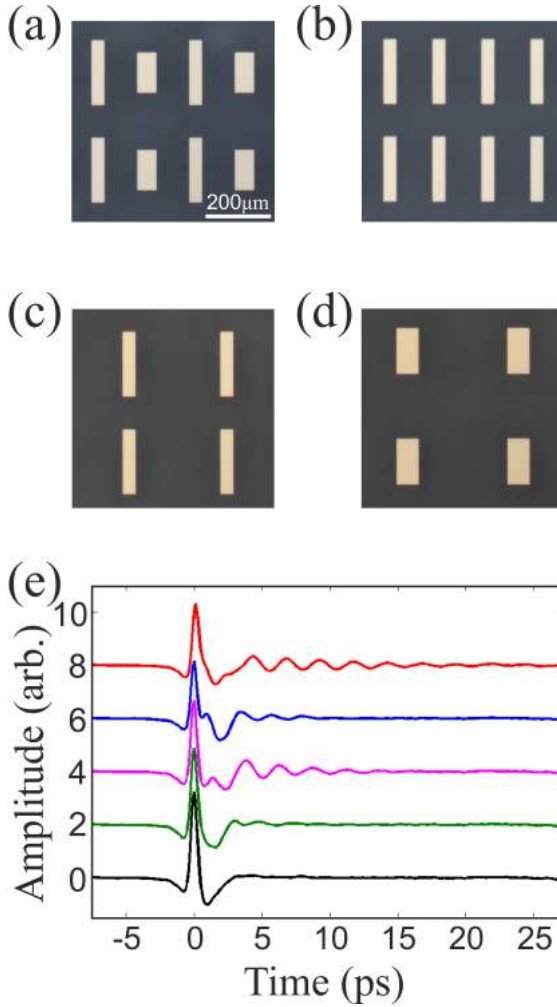
Using optical lithography, metal deposition and lift-off, we have fabricated samples containing 2D periodic lattices of gold rods on top of a 2 mm thick amorphous quartz substrate. Before the thermal evaporation of the 100 nm gold layer a 2 nm chromium adhesion layer was deposited.

Figure 5.1(a) shows an optical microscope image of the periodic lattice of detuned resonators. This sample consists of two gold rods with different sizes per unit cell of the lattice. The dimensions of the rods are  $200 \mu\text{m} \times 40 \mu\text{m}$  and  $125 \mu\text{m} \times 60 \mu\text{m}$ , and are referred to as the ‘long’ and ‘short’ rods, respectively. Both type of rods support resonances when illuminated with THz radiation, however the resonant frequencies are detuned from each other due to the different dimensions. Note that the width of the short rods in Figure 5.1(a) is larger than that of the long rods, which ensures a similar volume and surface coverage for the two types of rods. The lattice has a square symmetry with a period of  $300 \mu\text{m}$  in both directions. The separation between the detuned resonators is  $150 \mu\text{m}$  along the short axis of the rods.

A similar sample was prepared in which the short rods were replaced by the long rods in each unit cell. An optical microscope image of this sample is shown in Figure 5.1(b). We refer to this sample as the array of identical resonators. Two other samples are shown in Figures 5.1(c) and 5.1(d). These samples represent the periodic arrays of the individual long and short rods in each unit cell respectively. The periodicity of all the samples is the same as in the array of detuned resonators. The samples shown in Figure 5.1(b), (c) and (d) are control samples to understand the underlying mechanism of DIT in the sample of the detuned resonators. To study the effect of periodicity on the response of these samples we have also made samples where each of the detuned, identical, long and short resonators respectively are randomly distributed over the substrate.

## 5.3 Experimental results

The experiments were carried out using a commercial THz time domain spectrometer (Menlo Systems GmbH) based on photo-conductive generation and detection techniques as explained in Chapter 2. Figure 5.1(e) displays the transients of the THz transmission in the forward direction through the periodic arrays containing the detuned (red curve), the identical (blue curve), the individual long (magenta) and the individual short (green) resonators. The polarization of the THz electromagnetic field is set parallel to the long axes of the rods, and the THz beam propagates at normal incidence through the sample. The black curve in Figure 5.1(e) corresponds to a reference measurement taken through a quartz substrate without any rods. This reference shows the single-cycle THz pulse. The



**Figure 5.1:** Optical microscope images of square periodic arrays of (a) detuned, (b) identical, (c) long and (d) short gold rods defining THz resonators with a period of  $300 \mu\text{m}$  on top of a quartz substrate. The dimensions of the long rods are  $200 \mu\text{m} \times 40 \mu\text{m}$ , and those of the short rods are  $125 \mu\text{m} \times 60 \mu\text{m}$ . (e) THz transients of the forward transmission measured for the periodic arrays of detuned (red curve), identical (blue curve) long (magenta curve) and short (green curve) rods respectively, as well as the reference (black curve) measured through a quartz substrate without rods are shown. The transients are displaced vertically for clarity.

thickness of 3 mm of the substrate leads to a first reflection which is delayed by 40 ps with respect to the main THz pulse, i.e., outside the time window of the measurements. The transient measured through the array of identical resonators shows some oscillations (blue curve in Fig. 5.1(e)) after the main peak. For the long resonators, the oscillations (the magenta curve in Fig. 5.1(e)) extend to later times up to around 12 ps and for the array of shorter resonators the oscillations (the green curve in Fig. 5.1(e)) vanish within 6-7 ps. The main peaks in the transients at 0 ps correspond to the fraction of the THz amplitude that is not scattered or absorbed by the array. The rapid vanishing of the THz amplitude is an indication of a limited resonant interaction of the THz pulse with the array. The THz transient of the transmission through array of detuned resonators is pronouncedly different although the metal filling fractions of both samples are very similar. For the array of detuned resonators we observe that the THz transient contains a harmonic damped oscillation (red curve in Fig. 5.1(e)) which extends up to 25 ps. Such strong dispersion due to a periodic system is a characteristic behavior of diffraction enhanced transparency (DET). The harmonic THz signal at long time delays indicates the reduction of the group velocity in a narrow frequency window, as we show next.

The THz transients can be Fourier transformed to obtain the extinction of the arrays and the phase spectra of the transmitted signal. The complex transmitted field through the sample of detuned resonators can be written as  $E(\nu) \exp(i\phi'(\nu))$ , where  $E(\nu)$  is the transmitted amplitude and  $\phi'(\nu)$  the phase. The transmitted field through the bare substrate is given by  $E_{ref}(\nu) \exp(i\phi_{ref}(\nu))$ . The resulting amplitude transmission can be expressed as

$$t = \frac{E(\nu)e^{i\phi'(\nu)}}{E_{ref}(\nu)e^{i\phi_{ref}(\nu)}} = \frac{E(\nu)}{E_{ref}(\nu)} e^{i\Delta\phi(\nu)}, \quad (5.1)$$

where  $\Delta\phi(\nu) = \phi'(\nu) - \phi_{ref}(\nu)$  is the phase delay spectrum. We define the THz extinction spectra of the samples as

$$\mathcal{S} = 1 - |t|^2. \quad (5.2)$$

The extinction spectra are shown in Figure 5.2(a), where the blue curve corresponds to the extinction of the array of identical resonators and the red curve to the extinction of the arrays of detuned resonators. The former is characterized by a broad resonance with a maximum extinction at 0.45 THz. This resonance in the extinction corresponds to the resonant absorption and mainly to the resonant scattering of the  $\lambda/2$  resonance along the long axis of the rods. The THz electric field drives an electrical current along this axis that resonates over the length of the rods at this particular frequency. Note, that the resonance wavelength (667  $\mu\text{m}$ ) is longer than 2 times of the physical length of the rods, which can be attributed to the presence of the quartz substrate, the impedance at the edges of the rods [156], and diffractive coupling with the other rods in the array. The extinction spectrum changes drastically when one of the rods in the unit cell is replaced by the shorter one (red open circles in figure 5.2(a)). A window in which the extinction vanishes (the DET window) appears at 0.45 THz, and an additional maximum in the extinction appears at 0.4 THz. The vanishing extinction corresponds to a nearly full transmission at this particular frequency (Transmission =  $99.2 \pm 0.5$  %). In the next section we show, using

a coupled dipole model, that the DET window is the result of the interference of surface lattice resonances in the array of detuned resonators. The period of the lattice, which plays a crucial role, was chosen such that the DET is the largest in the frequency range of maximum sensitivity of the THz spectrometer.

The frequency-dependent phase delay,  $\Delta\phi(\nu)$ , obtained from the Fourier transform of the THz pulses transmitted through the arrays are displayed on Fig. 5.2(b). The phase delay for the array of identical resonators (blue open squares) presents the characteristic dispersion of a damped oscillator, with a change of sign in the phase at the resonant frequency of maximum extinction (marked by the vertical dashed line in the figure). The phase delay dispersion for the array of detuned oscillators (red open circles in Figure 5.2(b)) is pronouncedly different. The phase changes sign at the frequency of maximum extinction, but recovers its positive values at the transparency frequency (marked with the dashed line in the figure), where the system is highly dispersive in spite of the vanishing extinction. The phase delay, as defined earlier, can be written as,

$$\Delta\phi(\nu) = \phi'(\nu) - \phi_{ref}(\nu) = (\phi(\nu) + \phi_{quartz}(\nu)) - (\phi_0(\nu) + \phi_{quartz}(\nu)), \quad (5.3)$$

where,  $\phi(\nu)$  is the phase introduced solely by the array of the detuned resonators,  $\phi_{quartz}(\nu)$  is the phase introduced by the quartz substrate (which is the same for sample and the reference) and  $\phi_0(\nu)$  is the phase introduced by the layer of air with the same thickness as the lattice of detuned resonators. Therefore,

$$\Delta\phi(\nu) = (k(\nu) - k_0(\nu))L, \quad (5.4)$$

where  $k(\nu)$  is the wave vector in the array of the detuned dipole and  $k_0(\nu) = 2\pi\nu/c$  is the wave vector in air and  $L$  is the thickness of the array of resonators. The group index can be determined from the phase delay using the following expression[230, 231]

$$n_g(\nu) = \frac{c_0}{v_g(\nu)} = c_0 \frac{dk(\nu)}{d\nu} = \frac{c_0}{L} \frac{d\Delta\phi(\nu)}{d\nu} + 1, \quad (5.5)$$

where  $c_0$  is the speed of light in vacuum and  $v_g(\nu)$  is the group velocity, and phases are in units of  $2\pi$  radians. In figure 5.2(c) we plot the dependence of the group index on the frequency for both arrays of detuned (red open circles) and identical (blue open circles) resonators. The group index has a maximum value of more than  $6 \times 10^4$  for the array of detuned resonators. This remarkably large change in group index, corresponds to a group velocity of  $5 \times 10^3$  m/s at 0.45 THz, i.e., at the frequency of full transmission. At this frequency the wave is delayed by scattering within the array and is re-radiated in the forward direction. In comparison, it can be seen that no such dramatic increase in the group index is observed for the array of identical dipoles.

We have performed more measurements to elucidate the mechanism of such a unique spectral behavior. First, we have measured a random array of the detuned resonators to illustrate the influence of the periodic array on the DET. We see from Figure 5.3(a)(red open circles), that although there is a window of partial reduction of the extinction, it does not reach very low values at that frequency. This indicates that the periodicity in the array of the detuned resonators plays an important role in the DET. The spectral response

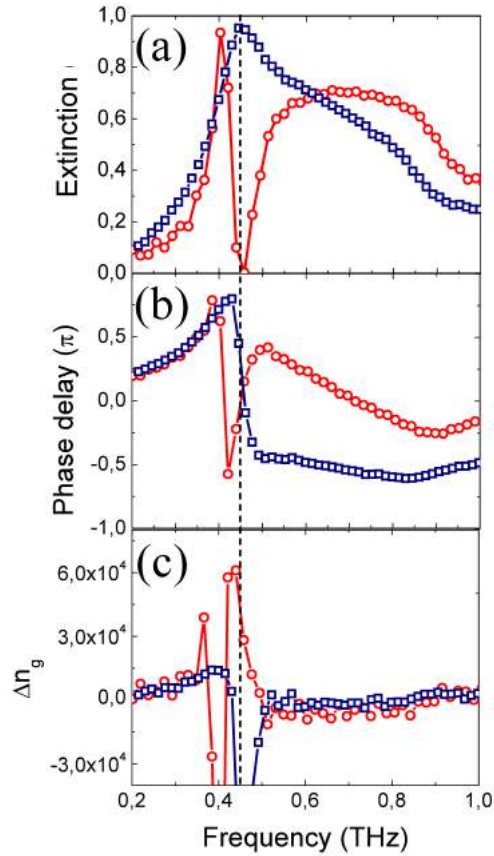


**Figure 5.2:** Extinction (a), phase delay (b), and group index (c) spectra of the arrays of detuned (red open circles) and identical (blue open squares) resonators corresponding to the transients shown in figure 5.1(e). The reference sample is an empty quartz substrate. The vertical dotted line at 0.45 THz indicates the frequency of induced transparency for the array with the detuned resonators.

from the random array of the identical resonators is also shown in Figure 5.3(a) (blue open squares). The different curves in Fig. 5.3(b) show the extinction due to the periodic array of the individual long rods (magenta open circles), the periodic array of the individual short rods (green open triangles), the random array of the long rods (magenta solid) and the random array of short rods (green dashes). The measurements in random arrays are done to elucidate the spectral responses of the individual rods keeping in mind that the randomness averages out any effect due to diffractive coupling between individual rods. Hence, the extinction of the random arrays of the short and the long rods are proportional to their individual spectral responses. We can appreciate in Fig. 5.3(b) that the spectral responses of the periodic arrays of both the short and long rods are different from the response of the random arrays of similar rods. This difference is the result of the radiative coupling of the rods. This coupling is enhanced through diffraction in the periodic array. In particular, when the wave-vector of the scattered wave is equal to an integer number times the inverse of the lattice constant of the array, the condition for in-plane diffraction is fulfilled. This condition known as the Rayleigh anomaly, leads to an increased scattered intensity along the plane of the array, which causes an enhanced coupling between the rods. This enhanced coupling is known as surface lattice resonances[119, 120, 122, 126] and gives rise to the red-shift and narrowing of the resonance. Note that the values of the extinctions of the arrays of long and short resonators (Figure 5.2(a)) do not reach zero around the DET frequency of 0.45 THz. Therefore, the incoherent sum of the two extinctions will never vanish at the DET window. This finite extinction of the arrays of equal resonators supports the interpretation that the response of the array of detuned resonators is the result of the coherent interference of the amplitudes of the two SLRs. The physics behind the formation of SLRs and their interference can be explained by considering the rods as radiatively coupled resonant dipoles. Therefore, in the following section we use the coupled dipole model to elucidate the underlying mechanism of DET.

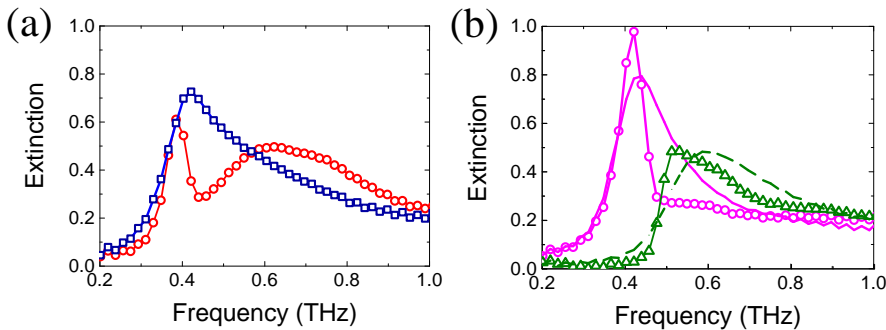


**Figure 5.3:** (a) Extinction through a random array of detuned resonators (red open circles) and through a random sample of identical resonators (blue open squares). (b) Extinction through periodic array of individual long rods (magenta open circles), periodic array of individual short rods (green open triangles), random array of individual long rods (magenta solid) and random array of individual short rods (green dashes).

## 5.4 Coupled dipole model

We have used a coupled dipole model to elucidate the underlying mechanism that gives rise to DET. For simplicity we have considered a 1D chain of dipoles embedded in a homogeneous environment with the refractive index of quartz ( $n=2$ ). These approximations facilitate the interpretation of the results, without reducing their generality.

The extinction cross section of an ensemble of metallic scatterers is related to the amount of work an incident electromagnetic wave does while driving the conducting electrons of these scatterers. This cross section can be expressed in terms of the wavenumber  $k$ , the polarization  $\mathbf{p}_i$  of the  $i^{\text{th}}$ -scatterer and the incident field  $\mathbf{E}_i^{\text{inc}}$  according to the following equation,[232]

$$C_{\text{ext}} = 4\pi k \sum_i \frac{\text{Im}(\mathbf{E}_i^{\text{inc}} \cdot \mathbf{p}_i)}{|\mathbf{E}_i^{\text{inc}}|^2}. \quad (5.6)$$

The polarization in turn depends on the incident field, the properties of the scatterer like material and shape and, for an ensemble of scatterers, their relative arrangement. The properties of the scatterer are described by the polarizability tensor  $\underline{\underline{\alpha}}$  which relates the polarization and the local field as  $\mathbf{p}_i = \underline{\underline{\alpha}}_i \mathbf{E}_i^{\text{loc}}$ . In an ensemble of scatterers the local field at each scatterer  $i$  is the sum of the incident field,  $\mathbf{E}_i^{\text{inc}}$ , and the field scattered by all other scatterers,  $\mathbf{E}_i^{\text{sca}}$ :

$$\mathbf{p}_i = \underline{\underline{\alpha}}_i \mathbf{E}_i^{\text{loc}} = \underline{\underline{\alpha}}_i (\mathbf{E}_i^{\text{inc}} + \mathbf{E}_i^{\text{sca}}). \quad (5.7)$$

The interaction through scattering between two sub-wavelength scatterers as a function of their respective distance  $\mathbf{r}$  can be approximated with the dipole-dipole interaction tensor  $\underline{\underline{G}}(\mathbf{r})$ [233]. Considering the sum over all dipoles gives

$$\mathbf{E}_i^{\text{sca}} = \sum_{j \neq i} \underline{\underline{G}}(\mathbf{r}_i - \mathbf{r}_j) \mathbf{p}_j. \quad (5.8)$$

In an infinite periodic lattice that is illuminated by a plane-wave, the behavior of all unit cells is identical over the full array and similar scatterers will have similar polarizations. When each unit cell contains two -not necessarily similar- scatterers the sum over all dipoles in Eq. (5.8) can be split in two contributions: one accounting for the interaction with all like dipoles, and the other accounting for the interaction with all unlike dipoles. If we label the dipoles either  $\circ$  or  $\bullet$ , we can express the polarization of Eq. (5.7) as

$$\mathbf{p}_\circ = \underline{\underline{\alpha}}_\circ \left[ \mathbf{E}_\circ^{\text{inc}} + \sum_{j \in \circ} \underline{\underline{G}}_{\circ,j} \mathbf{p}_\circ + \sum_{j \in \bullet} \underline{\underline{G}}_{\circ,j} \mathbf{p}_\bullet \right], \quad (5.9)$$

and

$$\mathbf{p}_\bullet = \underline{\underline{\alpha}}_\bullet \left[ \mathbf{E}_\bullet^{\text{inc}} + \sum_{j \in \bullet} \underline{\underline{G}}_{\bullet,j} \mathbf{p}_\bullet + \sum_{j \in \circ} \underline{\underline{G}}_{\bullet,j} \mathbf{p}_\circ \right]. \quad (5.10)$$

Equations (5.9) and (5.10) can be re-written in matrix form  $\mathbf{E}^{\text{inc}} = M \cdot \mathbf{P}$ , where the matrix  $M$  accounts for the diffractive coupling. More explicitly,

$$\begin{pmatrix} \mathbf{E}_\circ^{\text{inc}} \\ \mathbf{E}_\bullet^{\text{inc}} \end{pmatrix} = \begin{pmatrix} \underline{\underline{\alpha_\circ}}^{-1} - \underline{\underline{S_{\circ\circ}}} & -\underline{\underline{S_{\circ\bullet}}} \\ -\underline{\underline{S_{\bullet\circ}}} & \underline{\underline{\alpha_\bullet}}^{-1} - \underline{\underline{S_{\bullet\bullet}}} \end{pmatrix} \begin{pmatrix} \mathbf{P}_\circ \\ \mathbf{P}_\bullet \end{pmatrix}. \quad (5.11)$$

Each of the  $\underline{\underline{S}}$  matrices contains a lattice sum, which is defined as

$$\underline{\underline{S}}_{AB} = \sum_{j \in B} \underline{\underline{G}}_{A,j} \mathbf{P}_B, \quad (5.12)$$

where  $A$  and  $B$  correspond to either  $\circ$  or  $\bullet$ .

The dipole interaction tensor takes a simple scalar form,  $G(\mathbf{r})$ , when a 1D chain of dipoles is considered and the polarization is orthogonal to the direction of the chain. The scalar approximation is justified since, as a result of symmetry, the polarization of the particles is always parallel with the polarization of the incident field. The interaction tensor can be simplified to [234]

$$G(r) = \exp(ikr) \left( \frac{ik}{r^2} - \frac{1}{r^3} + \frac{k^2}{r} \right), \quad (5.13)$$

in which  $r$  is the distance between the respective dipoles. Solving the above equations for  $\mathbf{P}$ , and applying Eq. (5.6), the total extinction cross section of the array can be expressed as

$$C_{\text{ext}} = 4\pi k \text{Im} \left( \frac{2S_{\circ\bullet} - 2S_{\circ\circ} + \alpha_\circ^{-1} + \alpha_\bullet^{-1}}{S_{\circ\circ}^2 - S_{\circ\bullet}^2 - (\alpha_\circ^{-1} + \alpha_\bullet^{-1})S_{\circ\circ} + \alpha_\circ^{-1}\alpha_\bullet^{-1}} \right). \quad (5.14)$$

The periodic array of the long rods is a limiting case of this equation in which we have  $\alpha_\bullet = 0$ . In this case Eq. 5.14 is reduced to

$$C_\circ = 4\pi k \text{Im} \left( \frac{1}{\alpha_\circ^{-1} - S_{\circ\circ}} \right). \quad (5.15)$$

For the calculations the rods are approximated as perfect electric conductors, i.e., the permittivity of the metal is  $-\infty$ . The polarizability of the particles is calculated assuming that they have an ellipsoidal shape [235] and using the modified long wavelength approximation described in Ref. [232], which accounts for a finite size dynamic polarization and radiative damping. This results in

$$\alpha_\circ = \frac{1}{\frac{3F}{V} - \frac{2}{3}ik^3 - \frac{2k^2}{d}}, \quad (5.16)$$

where  $V$  is the volume,  $d$  the length and  $F$  the form factor of the rods for a wave vector  $k$ . Figure 5.4(a) shows the calculated extinctions of the periodic array of the long rods (magenta solid curve) and of one individual isolated long rod (magenta dotted curve) as a function of frequency. Diffraction from the lattice modifies the extinction spectrum of the localized resonance, with a reduction at the Rayleigh anomaly frequency and an

enhancement at lower frequency, which leads to a narrowing of extinction spectrum. This is the characteristic line shape of surface lattice resonances. Figure 5.4(b) shows the lattice sum of the array of the long rods (black curve) as well the inverse polarizability (magenta curve) of the individual long rods. The frequency of maximum extinction is indicated with the vertical dashed line in the figure, and it occurs when  $\alpha_0^{-1}$  equals  $S_{00}$ , as shown in Figure 5.4(b). At this frequency the denominator in Eq. 5.15 vanishes. The dotted line at 0.5 THz corresponds to the frequency of the Rayleigh anomaly condition, where a diffraction order propagates along the plane of the array. Constructive interference of the scattered amplitudes by the array gives rise to the suppression of extinction in the forward direction at the Rayleigh anomaly, which corresponds to the divergence of the lattice sum,  $S$ .

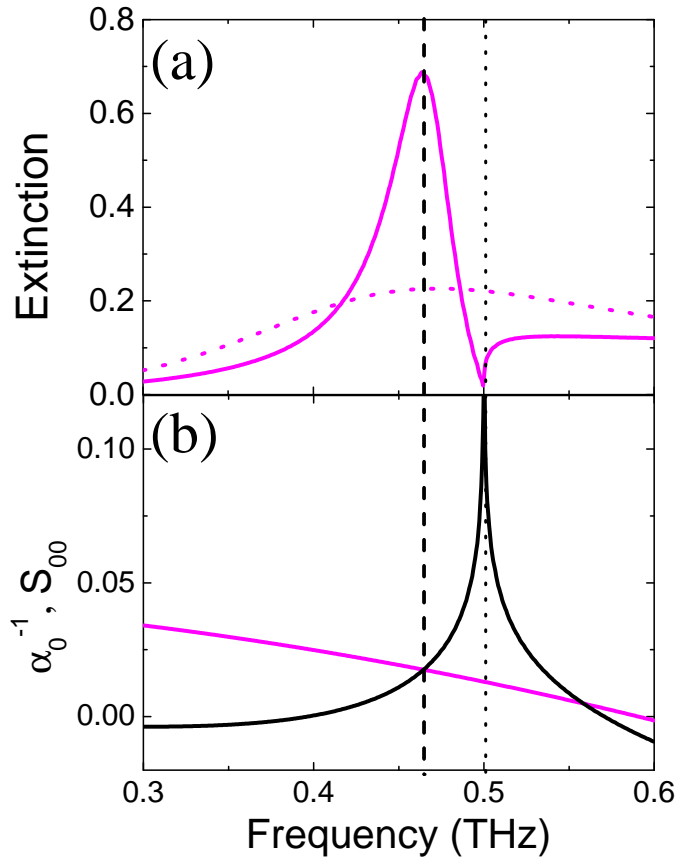


**Figure 5.4:** (a) Coupled dipole model calculation of extinction for an 1D array of long rods (magenta solid curve) and a single isolated long rod (magenta dotted curve), and (b) the real components of the lattice sum  $S_{00}$  and the inverse polarizability tensor,  $\alpha_0^{-1}$  of each rod. Both the quantities are in units of inverse volume.

Figure 5.5(a) displays the calculated spectrum using Eq. 5.14 for arrays of detuned dipoles with dimensions similar to those used in the experiments. This spectrum shows a sharp resonance with an enhanced extinction followed by a window of diffraction induced transparency at 0.45 THz. This window, indicated by the vertical dotted line in Fig. 5.5(a), qualitatively reproduces the main characteristics from the experimental response of the detuned dipoles as shown in Fig. 5.2(a).

The interference of the fields scattered in the plane of the array by the individual lattices of the detuned resonators, indicated by the lattice sum  $S_{\bullet\bullet}$ , is essential for explaining Fig. 5.5. If we consider  $S_{\bullet\bullet} = 0$  in Eq. 5.14, the equation is reduced to

$$C_{\text{ext}} = 4\pi k \text{Im} \left( \frac{1}{\alpha_{\circ}^{-1} - S_{\circ\circ}} + \frac{1}{\alpha_{\bullet}^{-1} - S_{\bullet\bullet}} \right) = C_{\circ} + C_{\bullet}. \quad (5.17)$$

This expression corresponds to the incoherent sum of the extinctions of the two individual lattices of long and short rods. Both  $C_{\circ}$  and  $C_{\bullet}$  are SLRs which have finite and positive extinctions for frequencies lower than the Rayleigh anomaly. Therefore, the incoherent sum can not vanish. This situation is represented in the measurements of Fig. 5.3(b) by the black dotted curve and is distinctly different from the diffraction induced transparency shown by the red open circles in Fig. 5.2(a). The necessity to include  $S_{\bullet\bullet}$  in our analysis confirms that DET is the result of the interference of the electromagnetic fields scattered in the plane of the array defined by the lattice sum of equal and unequal scatterers.

Figure 5.5(b) shows the calculated real components of  $S_{\circ\circ}$  (black solid curve),  $S_{\bullet\bullet}$  (black dashed curve),  $\alpha_{\circ}^{-1}$  (magenta curve), and  $\alpha_{\bullet}^{-1}$  (green curve). The lattice sums ( $S_{\circ\circ}$  and  $S_{\bullet\bullet}$ ) diverge at the Rayleigh anomaly condition, i.e. at 0.5 THz, but the corresponding extinction is still finite at this frequency because of their similar values and opposite signs. The opposite signs of the lattice sums can be attributed to the fact that the distances between the like dipoles follow the progression  $|\vec{r}| = a, 2a, 3a, \dots$ , whereas for the unlike dipoles  $|\vec{r}| = \frac{a}{2}, \frac{3a}{2}, \frac{5a}{2}, \dots$ , where  $a$  is the period of the lattice. Hence, the periodicity is the same for both lattice sums, which explains the divergence at the same frequencies; However, they are out of phase, which explains the opposite signs. The large group index, i.e., low group velocity, described in the previous section with the measurements can be understood by the delay in the wave propagation introduced by scattering into the surface modes of the array. We note that the experimental results do not show a strong reduction of the extinction due to Rayleigh anomalies for single SLRs (open circles and triangles in Fig. 5.3(b)). This discrepancy with the calculations can be explained by the presence of air-quartz interface in the experiments. This interface leads to an inhomogeneous surrounding around the particle array. However, the inhomogeneous surrounding does not suppress the DET window introduced by the array of detuned resonators in the measurements, which confirms the robustness of these structures for the realization of induced transparencies.

The dependence of the extinction with displacement between the two detuned dipoles within the unit cell is shown in Fig. 5.6. Figure 5.6(a) shows the spectra calculated for three different displacements: 150  $\mu\text{m}$  (red curve), 100  $\mu\text{m}$  (black curve) and 75  $\mu\text{m}$  (blue curve). The curves are vertically offset to elucidate the spectral features with respect to each other. The Rayleigh anomaly, which is represented by the dash-dotted vertical line at 0.5 THz, is

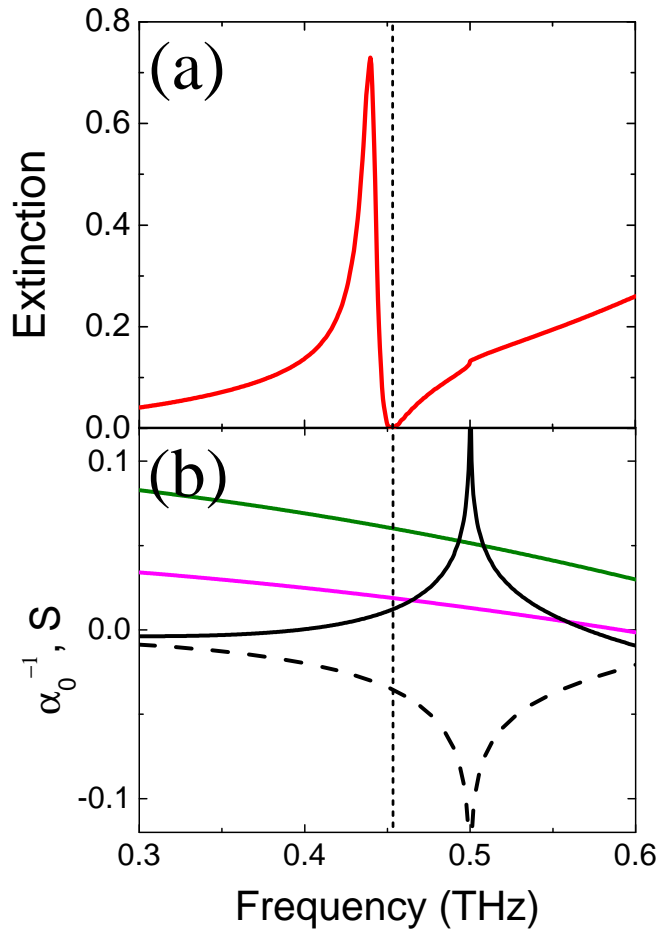


**Figure 5.5:** Coupled dipole model calculation for a 1D chain of 2000 unit cells of an array of detuned dipoles. (a) Extinction spectrum (b) real components of  $S_{oo}$  (black solid curve),  $S_{oo}$  (black dashed curve),  $\alpha_o^{-1}$  (magenta curve) and  $\alpha_s^{-1}$  (green curve) as presented in Eq. 5.14.

fixed for all the calculations. However, for the three different cases the spectral response is very different. By changing the displacement between the two detuned dipoles, it is possible to tune the transparency window in the response of the array. This indicates that even though the individual SLRs do not change, it is the interference between the two SLRs that is modified due to the relative displacement between the dipoles. Figure 5.6(b) shows the extinction due to the lattice of detuned dipoles as a function of frequency and displacement between the two dipoles. The three cases shown in Fig. 5.6(a) are marked by the three horizontal lines at 150, 100 and 75  $\mu\text{m}$  displacement. The Rayleigh anomaly is indicated by the vertical white dash-dotted line at 0.5 THz. The transparency window is symmetric on both sides of the horizontal line at 150  $\mu\text{m}$  where the window is the widest. This is the result of rotational symmetry at this displacement, as the pitch of the array is 300  $\mu\text{m}$ .

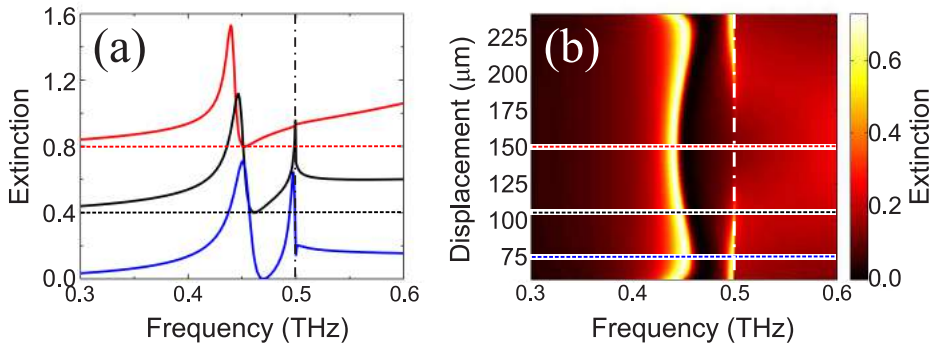


**Figure 5.6:** (a) Extinction spectra for two detuned dipoles in a 1D lattice with a pitch of 300  $\mu\text{m}$ . The three cases represent the different displacements between the dipoles; from top, 150  $\mu\text{m}$  (in red), 100  $\mu\text{m}$  (in black) and 75  $\mu\text{m}$  (in blue). The dimensions of the dipoles are the same as before. The spectra are displaced vertically to elucidate the behavior clearly. The dash-dotted vertical line marks the position of the Rayleigh anomaly. (b) Extinction spectra for the lattice of detuned dipoles as a function of frequency and displacements between them. The Rayleigh anomaly condition is indicated by the white dash-dotted vertical line. The three cases shown in (a) are represented by the three horizontal lines at 150, 100 and 75  $\mu\text{m}$  with same color coding.

## 5.5 THz near-field imaging

While the coupled dipole model elucidates the underlying physics behind the mechanism of the diffraction induced transparency, we measured the THz near-field distribution of the detuned resonator to validate this understanding. Figure 5.7 shows the near-field distribution of the real part of the electric field (normalized to individual maxima) around the rods at three distinct frequencies. Figure 5.7(a) shows the near-field map at 0.39 THz. At this frequency, the detuned resonator array shows a distinct peak in the extinction in

Fig. 5.2(a). From the resonant response of the long resonator in the near-field map, it is evident that this peak corresponds to the SLR in the long resonator. Note that this spectral peak (in the detuned resonator) is a bit red-shifted from the peak due to the SLR in the array of individual long resonators (Fig. 5.3). This red-shift is due to the fact that in the detuned resonator, the two SLRs (long and short) are coupled to each other. Figure 5.7(c) corresponds to the near-field of the SLR at 0.51 THz. At this frequency the high extinction observed in Fig. 5.2(a) corresponds to the extinction of the SLR of the short resonator. The most interesting case is seen in Figure 5.7(b) which corresponds to the near-field at the DET frequency, i.e., 0.45 THz. It can be deduced from the near-field map, that at this particular frequency, the dipole moments of both rods become equal in magnitude and with opposite phase. Such an orientation of dipole moments is due to the interference between the two SLRs. This explains the full transmission at the DET frequency. However, this process is not instantaneous, as it involves the resonant scattering and emission in the forward direction. Hence, this gives rise to the high group delay at this particular frequency which gives rise to the high group velocity dispersion.

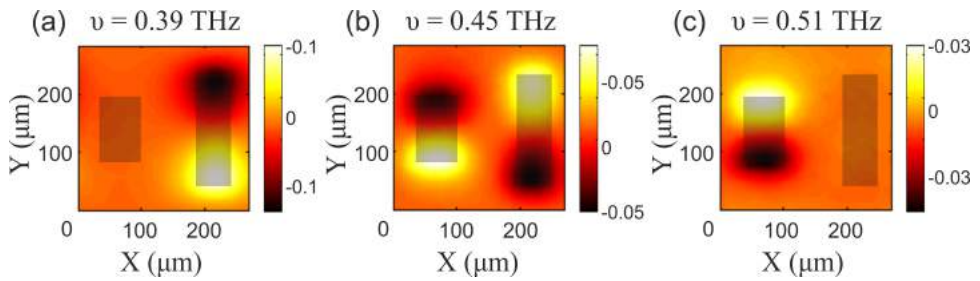


**Figure 5.7:** Near-field maps of the real electric field around one unit cell of the array of detuned resonators at (a)  $\nu = 0.39$  THz, (b)  $\nu = 0.45$  THz and (c)  $\nu = 0.51$  THz. The semi-transparent rectangles marks the position of the individual resonators.

## 5.6 Conclusions

In this chapter, we have demonstrated that a periodic array of scatterers with different dimensions can give rise to a narrow spectral transparency window with a transmission close to unity and very large group index. This transparency, which we have termed diffraction enhanced transparency (DET), is the result of the interference of collective resonances known as surface lattice resonances. The surface lattice resonances are the result of the enhanced diffractive coupling of localized resonances in the individual scatterers. The slow wave propagation (the group velocity is reduced by more than 4 orders of magnitude) due to the in-plane scattering and the near perfect transmission, makes DET an interesting phenomenon for the design of components for THz communication, such as delay elements. Our measurement of near-field maps of electric field in the vicinity of one unit cell of this array, further validates our understanding of the physics behind the DET window.



## CHAPTER 6

# VISUALIZING MODE HYBRIDIZATION IN THE NEAR-FIELD OF TERAHERTZ DOLMENS

---

*In this chapter we demonstrate that coupling between resonant structures in the near-field at length scales shorter than the wavelength can be exploited for modifying the electromagnetic radiation. Dolmens represent a geometry of significant interest, as they have been shown to exhibit electromagnetically induced transparency (EIT) through coupling between bright and dark modes, concurrently providing sharp spectral selectivity in transmission and a large reduction in group velocity. We use near-field terahertz scanning microscopy to map the electric fields in the vicinity of a metallic dolmen in both amplitude and phase i.e., the interaction between bright and dark modes in the time-domain, unraveling the physics resulting in EIT. We experimentally demonstrate the hybridization of bright and dark modes accompanying the near-field coupling, as well as the excitation of the dark mode at the frequency of the induced transparency.*

## 6.1 Introduction

Resonant structures provide useful building blocks for designing components to manipulate terahertz (THz) radiation [236, 237]. By exploiting the scattering properties of these structures, it is possible to fabricate THz modulators and filters as well as beam routing optics [238–241], where the thickness of these devices can reach only a fraction of the wavelength [242]. While the transfer function of optical components is typically evaluated in terms of the response to radiation incident from the far-field, for sub-wavelength scatterers those properties will depend sensitively on the near-fields in their vicinity [243, 244]. Moreover, these scatterers can consist of multiple elements placed in close proximity to one another, where near-field interactions between constituent elements can be exploited to manipulate the spectral behaviour [129–131]. Characterizing these interactions demands a probe with a resolution below the diffraction limit for uncovering the redistribution of electromagnetic radiation in the vicinity of coupled systems.

In this chapter, we present a study on dolmens, consisting of a horizontal rod with the long axis along the polarization of the incoming THz radiation and two orthogonal rods in close proximity to the two ends of the horizontal rod. In these structures near-field coupling leads to electromagnetically induced transparency (EIT) with successful implementations in two- and three dimensions [245, 246]. The near-field coupling occurs between bright and dark resonances, leading to the appearance of sharp peaks in the transmission spectrum accompanied by a large group velocity dispersion. These characteristics have potential applications in sensing or information processing [247]. Near-field measurements on plasmonic dolmens using scattering NSOM [248] and EELS/CL [249] have revealed the hybridization between bright and dark modes giving rise to so-called bonding and antibonding resonances which arise from near-field coupling [250]. Nevertheless, in spite of the impressive spatial resolutions achieved by these techniques, which probe structures at the deep subwavelength scale, they are restricted to measuring only intensity distributions unless combined with interferometry [251].

As explained in Chapter 2, investigating dolmen structures at THz frequencies, instead of optical, we gain the ability to measure the electric fields induced in the vicinity of the resonant structure in the time domain. The measurements presented in this work using THz near-field microscopy thus allow to directly characterize in both amplitude and phase the hybridization of modes giving rise to the far-field transparency window. We first introduce the structure and sample preparation for our experiments including a far-field spectroscopic characterization of the constituent parts of the dolmen. We then present near-field spectral maps of the electric field distributions which give rise to the far-field spectral features. Finally we demonstrate the spatial dependence of the interaction between bright and dark resonances.

## 6.2 Experimental results

The dolmen geometry consists of two resonators and can be summarized as follows: a resonant structure, here a horizontal gold rod oriented along the polarization of the incoming

radiation, is placed in close proximity to a pair of orthogonally oriented rods which constitute the second resonator. The horizontal rod supports a bright dipolar-like resonance, which couples to the incident field, while the vertical rod pair supports a quadrupolar resonance which does not couple to the incident plane wave radiation for symmetry reasons, and is thus dark and spectrally narrow from the absence of radiative losses.

By bringing the two resonators forming the dolmen into close proximity, the bright mode of the dipolar rod drives the dark mode through capacitive coupling across the gap separating them. This coupling is enhanced by minimizing the gap, and subsequently leads to the hybridization of modes in the structures, leading to a lower energy or bonding mode, and a higher energy or antibonding mode. The energy shifts result from attractive and repulsive interactions of charges across the gap, as shown in Fig. 6.1(a). In the spectral region between the bonding and antibonding modes, interference leads to the suppression of scattering in the forward direction, giving rise to EIT. Other geometries have been conceived by extension of this design principle, using various combinations of radiant and subradiant modes to obtain sharp and dispersive spectral features [252–255].

The dolmen structures were fabricated following standard photolithography procedures. Substrates were first cleaned and their surfaces activated using oxygen plasma, after which a layer of photoresist (MAN-1400, thickness  $1\mu\text{m}$ ) was deposited by spincoating. The structures were imprinted onto the resist using a positive mask. The unexposed areas of the photoresist were then removed using a developing solution (MAD-533S). Gold was deposited onto the structured resist with a thickness of roughly  $100\text{ nm}$ , with subsequent lift-off in acetone. The top rod has a length of  $150\mu\text{m}$  and width of  $40\mu\text{m}$ , corresponding to the lowest fundamental resonance of  $\sim 0.5\text{ THz}$  along the long axis, while the vertical rods have lengths of  $140\mu\text{m}$  and widths of  $40\mu\text{m}$ .

To characterize the resonances supported by the samples using far-field spectroscopy, we prepared arrays of structures arranged in a quasi-random fashion, such that the extinction can be measured while avoiding interferences related to diffractive coupling. The results shown here correspond to arrays with filling fractions ranging from  $\sim 7\text{-}20\%$ , corresponding to the total area covered by metal. The spectra are collected using a commercial THz-TDS setup (Menlo Systems GmbH) using photo-conductive detection technique as explained in Chapter 2. The far-field transmission measurements are shown in Fig. 6.1. In panel (b), time domain measurements of the transmitted electric field reveal the presence of a resonance supported by the top resonator for this polarization, and the effect of bringing the two resonators together: the THz transients for the substrate (grey) and vertical rods (black) are very similar, showing no resonant behaviour, while the transient associated with the sample of horizontal rods exhibits an overdamped resonance and attenuated trace corresponding to the excitation of its fundamental mode. For the dolmen sample (blue), the transient exhibits an underdamped component arriving at delayed times corresponding to the sample becoming transmissive at certain frequencies as compared to the horizontal rods by themselves.

By Fourier transformation of these transients and referencing to the transmission of the bare substrate, we compute the intensity extinction spectra for these samples as shown in Fig. 6.1(c). The sample of horizontal rods supports a strong and broad resonance centred at  $\nu = 0.55\text{ THz}$  (red curve in Fig. 6.1(c)). This resonance corresponds to the funda-

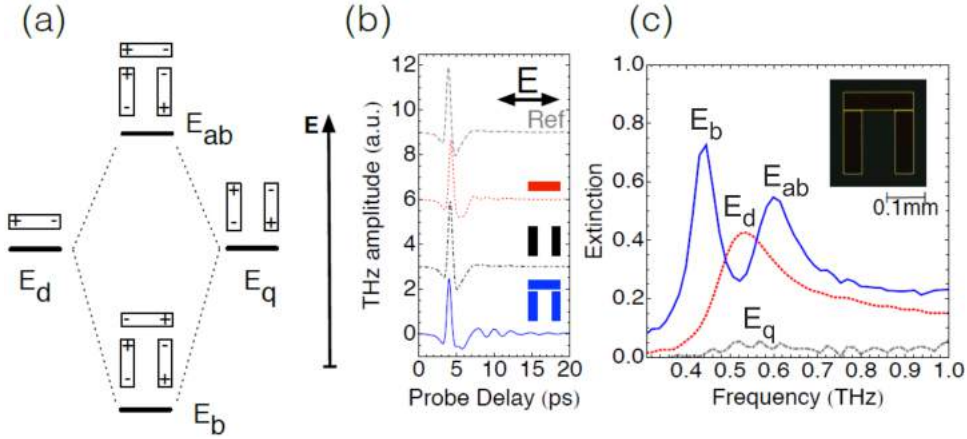


**Figure 6.1:** (a) Illustration of the formation of hybrid modes and excitation of a dark quadrupolar resonance as a result of near-field coupling in a dolmen.  $E_d$ ,  $E_q$ ,  $E_b$ , and  $E_{ab}$  represent the energies of the dipolar, quadrupolar, bonding, and antibonding resonances, respectively. (b) Time domain transients corresponding to the reference THz pulse transmitted through the substrate (grey, dashed), the pulse transmitted through a random array of dipolar rods (red, dotted), quadrupolar rod pairs (black, dot-dashed), and dolmens (blue, solid). (c) Extinction measurements corresponding to transients in panel (a), where the filling fractions are 5%, 12% and 12% for the dipolar rods, quadrupolar rods and dolmens, respectively. The frequency resolution is 15 GHz. Inset: dark-field microscope image of dolmen at 20 $\times$  magnification).

mental (dipole-like or  $\lambda/2$ ) resonance along the length of the rod. For the vertical rod pair we observe a featureless far-field spectrum since for this polarization the fundamental resonance along the short axis occurs at higher frequencies. For the dolmen we observe a splitting of the bright mode into two peaks (blue curve), corresponding to the aforementioned bonding and antibonding modes.

To support the assignment of these modes and ascertain the near-field distributions giving rise to the transparency observed in Fig. 6.1(c), we probe an isolated dolmen in the THz near-field microscope explained in Chapters 2 section 2.4 to measure the electric fields surrounding the dolmen. For these measurements, we collect the local fields polarized out-of-the-plane of the sample ( $E_z$ ) using a tip (TD-800-Z-WT, Protemics GmbH) with a spatial resolution on the order of 5  $\mu\text{m}$  [150].

The results of these scans for a dolmen with a 1  $\mu\text{m}$  gap separating the horizontal and vertical rods are shown in Fig. 6.2, where we plot the real part of  $E_z$ . Beginning with the measurement for  $\nu = 0.47$  THz (Fig. 6.2(a)), the near-fields in the horizontal rod assume a dipolar shape corresponding to the  $\lambda/2$  resonance of the rod. Similarly, the two vertical rods also exhibit dipolar field distributions, with opposite phases, leading to an overall quadrupolar character for the dark mode. For this frequency of radiation the relative phases of the electric field across the gap separating the resonators are opposite, giving rise to the so-called bonding mode corresponding to the lower energy resonance observed in the far-field. At 0.53 THz (Fig. 6.2(b)), the near-fields in the vicinity of the horizon-

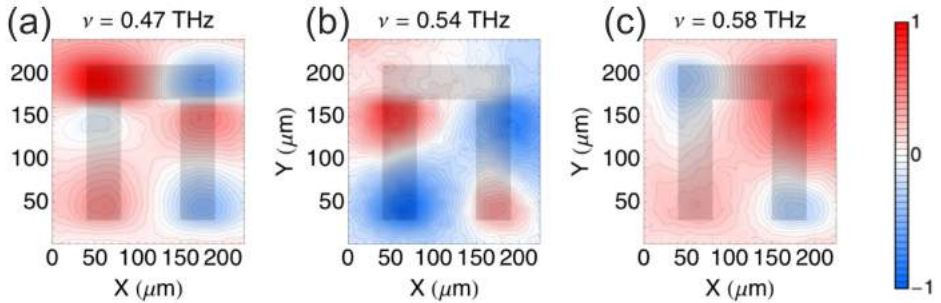


**Figure 6.2:** Measured real part of the out-of-plane component of the near-field, corresponding to an excited dolmen with a gap of  $1 \mu\text{m}$  separating bright and dark resonators at selected frequencies. Each spectral map is normalized to its own maximum value, with contours given at 5%. (a) and (c) correspond to the bonding and antibonding modes, respectively, while (b) reveals the excitation of the dark mode with a quadrupolar field profile.

tal rod vanish. These fields are enhanced entirely in the vicinity of the vertical rod pair, consistently with the reduction of extinction observed in the far-field spectrum for those frequencies. Finally, at 0.58 THz (Fig. 6.2(c)) we observe a change in the relative phase of the horizontal resonator, corresponding to the antibonding mode where repulsive interactions between horizontal and vertical resonators.

The spectral location at which the near-fields corresponding to the bright resonance are minimized (see Fig. 6.2(b)) is in very good agreement with the location of the transparency window in the far-field. The spectral locations of the bonding and anti-bonding modes as shown in Fig. 6.2 are somewhat shifted relative to their maxima as observed in Fig. 6.1(b), although not dramatically within the spectral resolution of the measurement. While a discrepancy between near- and far-field features in dolmen structures has previously been predicted for plasmonic dolmens [129], these spectral shifts arise largely to the material losses in the metal acting to damp the motion of charges induced by the driving field. For THz frequencies this effect is minimized by the fact that gold behaves approximately as a perfect electrical conductor, and the resonances are broadened by radiative losses. Moreover, the absolute peak positions in the far-field results in Fig. 6.1b may be shifted relative to their near-field equivalents due to interference between the incident and scattered fields resulting from the high scattering efficiency of the sample at the filling fractions employed [176].

The near-field maps for a gap of  $1 \mu\text{m}$ , corresponding approximately to  $\lambda/600$ , demonstrate strong hybridization between the different resonances in the structure. Increasing the gap allows to tune the strength of the near-field coupling. Through fabrication of dolmens possessing larger gap sizes, we show in Fig. 6.3 the gap dependence on the spectral features discussed thus far. The extinction spectra highlight that for gaps on the order of  $20 \mu\text{m}$  or larger, near-field coupling becomes negligible leading to unresolved bonding

and antibonding modes and little induced transparency. For a gap of  $20\ \mu\text{m}$  the extinction already resembles that of the dipolar-like resonance.

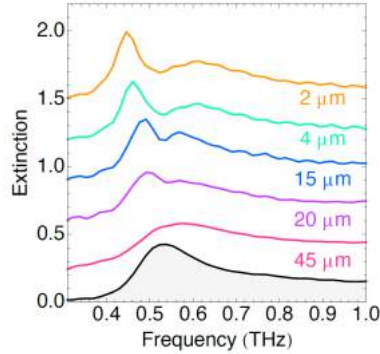


**Figure 6.3:** Extinction measurements on random arrays of dolmens (12% filling fraction) as a function of gap size separating resonators, with traces shifted by 0.3 for clarity. For reference, the extinction spectrum of the bright mode is shown in shaded grey.

By monitoring the frequencies of the hybrid modes in Fig. 6.4(a), we confirm that once the structures are brought to within a distance of approximately  $20\ \mu\text{m}$  the effects of near-field coupling become important, and that for larger gaps no hybridization takes place. This distance over which the two coupled modes will interact strongly can be understood from the spatial decay of the bright mode. In panel (b) we show the distribution of electric near-field around an isolated rod at the dipolar-like resonance frequency, i.e., the bright mode. By taking a line profile across the width of the rod as in panel (c), we recover the decay of the electric field at the position where the vertical rods are placed in the dolmen samples. We find that the field decays by approximately 80% relative to its maximum value within a  $20\ \mu\text{m}$  distance from the edge in the lateral direction, consistently with the onset of hybridization measured in the far-field spectra for those gap sizes. This distance is perhaps an overestimate, due to the finite spatial resolution of the near-field tips, but corroborates the spectral features and gap size dependence observed in the accompanying measurements. These results also provide an intuitive link between the measured gap dependence in extinction and the properties of the constituent elements of the dolmen.

## 6.3 Conclusions

Using THz spectroscopy in the near- and far-field we have investigated electromagnetically induced transparencies at THz frequencies in a gold dolmen structure. Near-field scanning microscopy was used to map out the field distributions of the modes which are formed via near-field coupling within the dolmen structure, where the bonding and antibonding modes which arise due to hybridization of bright and dark modes was revealed in both amplitude and phase. By varying the geometry of the structures, the coupling strength between bright and dark modes was tuned with accompanying variation in hy-

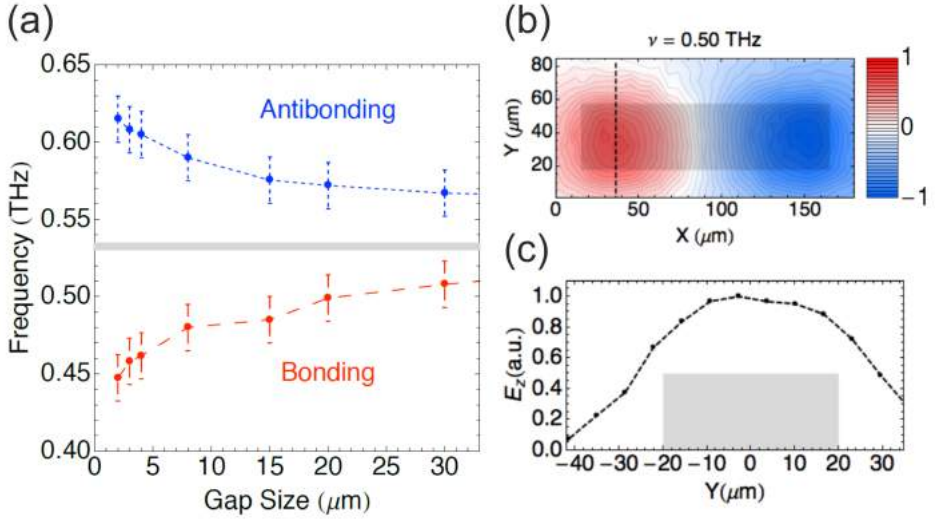


**Figure 6.4:** (a) Frequencies of bonding and antibonding modes as a function of gap size. Error bars given by the frequency resolution in the measurement. Shaded grey area indicates the resonance frequency of the bright mode. (b) Near-field map of an isolated rod taken at the resonant frequency. Amplitudes are normalized to the maximum value, and contours are given at 5%, with shape of rod given in grey overlay. (c) Line profile of the near-field map, showing the decay of the field in the Y direction. The cross-section of rod shown in grey, for illustration.

bridization and induced transparency. Moreover, near-field microscopy on the bright resonator revealed the minimum distance required for observation of effective coupling between bright and dark modes. These results highlight the underlying physics in this structure of two interacting resonators, resolving the coupling which gives rise to the transparency by measuring the near-field excitation of the dark mode at the frequency where extinction is suppressed in the far field. This technique can be easily extended to probe more complex metamaterial structures, or combined with near-field excitation to interrogate dark modes directly. Finally, by extension of this approach to materials for THz plasmonics or photoactive THz materials we can explore the near-field dynamics and couplings associated with carrier dynamics in semiconductor microstructures, to provide input for the design of active devices for THz photonics applications.



# REFERENCES

---

- [1] *The Cambridge Companion to Arabic Philosophy*.
- [2] N. El-Bizri, *A PHILOSOPHICAL PERSPECTIVE ON ALHAZEN'S OPTICS*, *Arabic Sciences and Philosophy* **15**, 189 (2005).
- [3] M. Caspar and C. D. Hellman, *Kepler*, Courier Corporation, 1993, Google-Books-ID: 0r68pggBSbgC.
- [4] R. Descartes, *Discourse on Method, Optics, Geometry, and Meteorology*, Hackett Publishing, 2001, Google-Books-ID: XKVvclclrnwC.
- [5] I. Newton, *Opticks: A treatise of the reflections, refractions, inflexions and colours of light. Also two treatises of the species and magnitude of curvilinear figures*, London : Printed for Sam Smith, and Benj. Walford, printers to the Royal Society, at the prince's Arms in St. paul's Church-yard, 1704.
- [6] R. Hooke, *Micrographia - the Original Classic Edition*, Emereo Pty Limited, 2012, Google-Books-ID: d\_dZLwEACAAJ.
- [7] C. Huygens, *Traité de la lumière: où sont expliquées les causes de ce qui luy arrive dans la reflexion, & dans la refraction, et particulièrement dans l'étrange refraction du Cristal d'Islande*, Pierre Vander Aa, 1690, Google-Books-ID: No8PAAAAQAAJ.
- [8] T. Young, *A course of lectures on natural philosophy and the mechanical arts. By Thomas Young.*, Printed for J. Johnson,, London :, 1807.
- [9] H. Crew, C. Huygens, T. Young, A. J. Fresnel, and F. F. Arago, *The wave theory of light; memoirs of Huygens, Young and Fresnel*, New York, Cincinnati American Book Company, 1900.
- [10] J. C. Maxwell, *A treatise on electricity and magnetism*, Oxford : Clarendon Press, 1873.
- [11] M. Planck and Physics, *The Theory of Heat Radiation*, Dover Publications, New York, first thus used edition edition, 2011.

## References

---

- [12] A. Einstein, *Über einen die Erzeugung und Verwandlung des Lichtes betreffenden heuristischen Gesichtspunkt*, *Annalen der Physik* **322**, 132 (1905).
- [13] A. V. Helden, S. Dupré, R. v. Gent, and H. Zuidervaart, editors, *The Origins of the Telescope*, Amsterdam University Press, Amsterdam, 2011.
- [14] H. C. King and T. Space, *The History of the Telescope*, Dover Publications, Mineola, N.Y, 2011.
- [15] E. A. Ash and G. Nicholls, *Super-resolution Aperture Scanning Microscope*, *Nature* **237**, 510 (1972).
- [16] D. W. Pohl, W. Denk, and M. Lanz, *Optical stethoscopy: Image recording with resolution  $\lambda/20$* , *Applied Physics Letters* **44**, 651 (1984).
- [17] E. Betzig, A. Harootunian, A. Lewis, and M. Isaacson, *Near-field diffraction by a slit: implications for superresolution microscopy*, *Appl. Opt.* **25**, 1890 (1986).
- [18] B. Albert, B. Johannes, and A. Van Gorcum, *Reflecting type telescope having a spherical mirror*, 1950, US Patent 2,504,383.
- [19] M. F. *Astronomical telescope*, 1943, US Patent 2,326,552.
- [20] H. Wolter, *Mirror systems with grazing incidence as image-forming optics for x-rays*, *Mirror systems with grazing incidence as image-forming optics for X-rays* Transl. into ENGLISH from *Ann. Phys.(Leipzig)*, ser. 6, v. 10, 1952 p 94-114 **1**, 94 (1975).
- [21] F. Galton, *Composite Portraits, Made by Combining Those of Many Different Persons Into a Single Resultant Figure.*, *The Journal of the Anthropological Institute of Great Britain and Ireland* **8**, 132 (1879).
- [22] A. A. Michelson, *The relative motion of the earth and of the luminiferous ether*, *American Journal of Science* , 120 (1881).
- [23] L. Mach, *Ueber einen interferenzrefraktor*, *Zeitschrift für Instrumentenkunde* **12**, 89 (1892).
- [24] W. Ritchie, *XXXII. On a new Photometer, founded on the Principles of Bouguer*, *Transactions of the Royal Society of Edinburgh* **10**, 443 (1826).
- [25] L. Laurent, *Ein Projectionssaccharimeter*, *Zeitschrift für analytische Chemie* **28**, 81 (1889).
- [26] J. v. Fraunhofer, *Bestimmung des Brechungs- und Farbenzerstreuungs-Vermögens verschiedener Glasarten, in Bezug auf die Vervollkommnung achromatischer Fernrohre*, Franz, 1817, Google-Books-ID: 4nFamGEACAAJ.
- [27] R. G. Gould, *The LASER, light amplification by stimulated emission of radiation*, in *The Ann Arbor conference on optical pumping, the University of Michigan*, volume 15, page 128, 1959.

- 
- [28] J. Nishizawa and K. Suto, *Terahertz wave generation and light amplification using Raman effect*, in *Physics of semiconductor devices*, edited by K. N. Bhat and A. DasGupta, page 27, Narosa Publishing House, New Delhi, 2004.
- [29] M. Borner, *Electro-optical transmission system utilizing lasers*, 1974, US Patent 3,845,293.
- [30] M. Dignonnet and H. J. Shaw, *Wavelength multiplexing in single-mode fiber couplers*, *Appl. Opt.* **22**, 484 (1983).
- [31] S. Alexander, *Wavelength division multiplexed optical communication systems employing uniform gain optical amplifiers*, 1997, US Patent 5,696,615.
- [32] C. Yeh, *Applied Photonics*, Elsevier, 2012, Google-Books-ID: 1kTInFpx8m8C.
- [33] R. S. Quimby, *Photonics and Lasers: An Introduction*, John Wiley & Sons, 2006.
- [34] T. H. Maiman, *Stimulated Optical Radiation in Ruby*, *Nature* **187**, 493 (1960).
- [35] O. Losev, *Luminous carborundum [silicon carbide] detector and detection with crystals*, *Telegrafiya i Telefoniya bez Provodov* **44**, 485 (1927).
- [36] R. Hall, *Stimulated emission semiconductor devices*, 1966, US Patent 3,245,002.
- [37] J. Shive, *Photoresistive translating device*, 1951, US Patent 2,560,606.
- [38] G. N. van den Hoven, R. J. I. M. Koper, A. Polman, C. van Dam, J. W. M. van Uffelen, and M. K. Smit, *Net optical gain at 1.53  $\mu\text{m}$  in Er-doped  $\text{Al}_2\text{O}_3$  waveguides on silicon*, *Applied Physics Letters* **68** (1996).
- [39] V. Berger, *Nonlinear photonic crystals*, *Physical review letters* **81**, 4136 (1998).
- [40] M. Notomi, *Theory of light propagation in strongly modulated photonic crystals: Refractionlike behavior in the vicinity of the photonic band gap*, *Physical Review B* **62**, 10696 (2000).
- [41] T. Baba, *Slow light in photonic crystals*, *Nature photonics* **2**, 465 (2008).
- [42] V. V. G. Veselago, *The electrodynamics of substances with simultaneously negative values of  $\epsilon$  and  $\mu$* , *Soviet Physics Uspekhi* **10**, 509 (1968).
- [43] A. V. Kildishev, A. Boltasseva, and V. M. Shalaev, *Planar photonics with metasurfaces*, *Science* **339**, 1232009 (2013).
- [44] N. Yu and F. Capasso, *Flat optics with designer metasurfaces*, *Nature materials* **13**, 139 (2014).
- [45] D. J. Kane and R. Trebino, *Single-shot measurement of the intensity and phase of an arbitrary ultrashort pulse by using frequency-resolved optical gating*, *Optics letters* **18**, 823 (1993).

## References

---

- [46] C. Iaconis and I. A. Walmsley, *Spectral phase interferometry for direct electric-field reconstruction of ultrashort optical pulses*, Opt. Lett. **23**, 792 (1998).
- [47] M. L. M. Balistreri, H. Gersen, J. P. Korterik, L. Kuipers, and N. F. van Hulst, *Tracking Femtosecond Laser Pulses in Space and Time*, Science **294**, 1080 (2001).
- [48] B. Xu, J. M. Gunn, J. M. D. Cruz, V. V. Lozovoy, and M. Dantus, *Quantitative investigation of the multiphoton intrapulse interference phase scan method for simultaneous phase measurement and compensation of femtosecond laser pulses*, JOSA B **23**, 750 (2006).
- [49] M. Tonouchi, *Cutting-edge terahertz technology*, Nature photonics **1**, 97 (2007).
- [50] R. de L. Kronig, *On the Theory of Dispersion of X-Rays*, J. Opt. Soc. Am. **12**, 547 (1926).
- [51] M. C. Beard, G. M. Turner, and C. A. Schmuttenmaer, *Subpicosecond carrier dynamics in low-temperature grown GaAs as measured by time-resolved terahertz spectroscopy*, Journal of Applied Physics **90**, 5915 (2001).
- [52] M. Liu, M. B. Johnston, and H. J. Snaith, *Efficient planar heterojunction perovskite solar cells by vapour deposition*, Nature **501**, 395 (2013).
- [53] X. Miao, S. Tongay, M. K. Petterson, K. Berke, A. G. Rinzler, B. R. Appleton, and A. F. Hebard, *High efficiency graphene solar cells by chemical doping*, Nano letters **12**, 2745 (2012).
- [54] M.-L. Tsai, S.-H. Su, J.-K. Chang, D.-S. Tsai, C.-H. Chen, C.-I. Wu, L.-J. Li, L.-J. Chen, and J.-H. He, *Monolayer MoS<sub>2</sub> heterojunction solar cells*, Acs Nano **8**, 8317 (2014).
- [55] G. P. Williams, *Filling the THz gap—high power sources and applications*, Reports on Progress in Physics **69**, 301 (2005).
- [56] S. Matsuura, M. Tani, and K. Sakai, *Generation of coherent terahertz radiation by photomixing in dipole photoconductive antennas*, Applied Physics Letters **70**, 559 (1997).
- [57] A. Rice, Y. Jin, X. Ma, X.-C. Zhang, D. Bliss, J. Larkin, and M. Alexander, *Terahertz optical rectification from <110> zinc-blende crystals*, Applied physics letters **64**, 1324 (1994).
- [58] A. Nahata, A. S. Weling, and T. F. Heinz, *A wideband coherent terahertz spectroscopy system using optical rectification and electro-optic sampling*, Applied Physics Letters **69**, 2321 (1996).
- [59] P. Gu and M. Tani, *Terahertz radiation from semiconductor surfaces*, in *Terahertz Optoelectronics*, pages 63–98, Springer, 2005.
- [60] V. Apostolopoulos and M. Barnes, *THz emitters based on the photo-Dember effect*, Journal of Physics D: Applied Physics **47**, 374002 (2014).

- 
- [61] D. J. Cook and R. M. Hochstrasser, *Intense terahertz pulses by four-wave rectification in air*, Opt. Lett. **25**, 1210 (2000).
- [62] M. Kress, T. Löffler, S. Eden, M. Thomson, and H. G. Roskos, *Terahertz-pulse generation by photoionization of air with laser pulses composed of both fundamental and second-harmonic waves*, Opt. Lett. **29**, 1120 (2004).
- [63] K. Y. Kim, A. J. Taylor, J. H. Glowina, and G. Rodriguez, *Coherent control of terahertz supercontinuum generation in ultrafast laser-gas interactions*, Nat Photon **2**, 605 (2008).
- [64] G. P. Williams, *FAR-IR/THz radiation from the Jefferson Laboratory, energy recovered linac, free electron laser*, Review of Scientific Instruments **73** (2002).
- [65] M. Abo-Bakr, J. Feikes, K. Holldack, P. Kuske, W. B. Peatman, U. Schade, G. Wüstefeld, and H.-W. Hübers, *Brilliant, Coherent Far-Infrared (THz) Synchrotron Radiation*, Phys. Rev. Lett. **90**, 094801 (2003).
- [66] R. Köhler, A. Tredicucci, F. Beltram, H. E. Beere, E. H. Linfield, A. G. Davies, D. A. Ritchie, R. C. Iotti, and F. Rossi, *Terahertz semiconductor-heterostructure laser*, Nature **417**, 156 (2002).
- [67] B. S. Williams, *Terahertz quantum-cascade lasers*, Nat Photon **1**, 517 (2007).
- [68] S. Kono, M. Tani, P. Gu, and K. Sakai, *Detection of up to 20 THz with a low-temperature-grown GaAs photoconductive antenna gated with 15 fs light pulses*, Applied Physics Letters **77**, 4104 (2000).
- [69] M. Bass, P. Franken, J. Ward, and G. Weinreich, *Optical rectification*, Physical Review Letters **9**, 446 (1962).
- [70] A. Nahata, A. S. Weling, and T. F. Heinz, *A wideband coherent terahertz spectroscopy system using optical rectification and electro-optic sampling*, Applied Physics Letters **69**, 2321 (1996).
- [71] T. Zentgraf, R. Huber, N. C. Nielsen, D. S. Chemla, and R. A. Kaindl, *Ultrabroadband 50-130 THz pulses generated via phase-matched difference frequency mixing in LiIO<sub>3</sub>*, Opt. Express **15**, 5775 (2007).
- [72] K. L. Vodopyanov, M. M. Fejer, X. Yu, J. S. Harris, Y.-S. Lee, W. C. Hurlbut, V. G. Kozlov, D. Bliss, and C. Lynch, *Terahertz-wave generation in quasi-phase-matched GaAs*, Applied Physics Letters **89** (2006).
- [73] T. Tanabe, K. Suto, J. Nishizawa, K. Saito, and T. Kimura, *Tunable terahertz wave generation in the 3- to 7-THz region from GaP*, Applied Physics Letters **83** (2003).
- [74] X.-C. Zhang, X. F. Ma, Y. Jin, T.-M. Lu, E. P. Boden, P. D. Phelps, K. R. Stewart, and C. P. Yakymyshyn, *Terahertz optical rectification from a nonlinear organic crystal*, Applied Physics Letters **61** (1992).

## References

---

- [75] X.-C. Zhang, B. B. Hu, J. T. Darrow, and D. H. Auston, *Generation of femtosecond electromagnetic pulses from semiconductor surfaces*, Applied Physics Letters **56** (1990).
- [76] P. Gu, M. Tani, S. Kono, K. Sakai, and X.-C. Zhang, *Study of terahertz radiation from InAs and InSb*, Journal of Applied Physics **91** (2002).
- [77] J. W. Goodman, *Introduction to Fourier Optics*, McGraw-Hill, San Francisco, 1968.
- [78] M. Born and E. Wolf, *Principles of optics: electromagnetic theory of propagation, interference and diffraction of light*, CUP Archive, 2000.
- [79] A. Yariv and P. Yeh, *Photonics: Optical Electronics in Modern Communications*, Oxford University Press, Oxford, 6 edition, 2007.
- [80] P. Mouroulis and J. Macdonald, *Geometrical optics and optical design*, Oxford University Press, USA, 1997.
- [81] F. M. Grimaldi, *Physico-mathesis de lumine, coloribus, et iride, aliisque adnexis libri duo: opus posthumum*, 1665, Google-Books-ID: FzYVAAAAQAAJ.
- [82] C. Huygens, *Traite de la lumière*, 1678.
- [83] G. Kirchhoff, *Zur theorie der lichtstrahlen*, Annalen der Physik **254**, 663 (1883).
- [84] E. Wolf and E. W. Marchand, *Comparison of the Kirchhoff and the Rayleigh-Sommerfeld Theories of Diffraction at an Aperture*, J. Opt. Soc. Am. **54**, 587 (1964).
- [85] G. Green, *An Essay on the Application of Mathematical Analysis to the Theories of Electricity and Magnetism*, author, 1828, Google-Books-ID: GwYXAAAAYAAJ.
- [86] L. Eyges, *The classical electromagnetic field*, Courier Corporation, 1980.
- [87] F. Kottler, *Zur theorie der beugung an schwarzen schirmen*, Annalen der Physik **375**, 405 (1923).
- [88] J. Stratton and L. Chu, *Diffraction theory of electromagnetic waves*, Physical Review **56**, 99 (1939).
- [89] N. Mukunda, *Consistency of Rayleigh's diffraction formulas with Kirchhoff's boundary conditions*, Air Force Office of Scientific Research, United States Air Force, 1962.
- [90] W. Southwell, *Validity of the Fresnel approximation in the near field*, JOSA **71**, 7 (1981).
- [91] K. Patorski, *Fraunhofer diffraction patterns of titled planar objects*, Journal of Modern Optics **30**, 673 (1983).

- 
- [92] J. F. W. Herschel, *Treatises on physical astronomy, light and sound contributed to the Encyclopaedia metropolitana*, London, R. Griffin.
- [93] G. B. Airy, *On the Diffraction of an Object-glass with Circular Aperture*, Transactions of the Cambridge Philosophical Society **5**, 283 (1835).
- [94] L. R. E.R.S., *XXXI. Investigations in optics, with special reference to the spectroscope*, Philosophical Magazine Series **5**, 261 (1879).
- [95] C. M. Sparrow, *On spectroscopic resolving power*, The Astrophysical Journal **44**, 76 (1916).
- [96] C. Grossmann, H.-G. Roos, and M. Stynes, *Numerical treatment of partial differential equations*, Springer, 2007.
- [97] F. Zhen, Z. Chen, and J. Zhang, *Toward the development of a three-dimensional unconditionally stable finite-difference time-domain method*, IEEE Transactions on Microwave Theory and Techniques **48**, 1550 (2000).
- [98] K. S. Yee et al., *Numerical solution of initial boundary value problems involving Maxwell's equations in isotropic media*, IEEE Trans. Antennas Propag **14**, 302 (1966).
- [99] R. P. Feynman, *There's plenty of room at the bottom*, Engineering and science **23**, 22 (1960).
- [100] K. E. Drexler, *Nanosystems: molecular machinery, manufacturing, and computation*, John Wiley & Sons, Inc., 1992.
- [101] D. K. Eric, *Engines of Creation. The Coming Era of Nanotechnology*, 1986.
- [102] R. Pease, *Electron beam lithography*, Contemporary Physics **22**, 265 (1981).
- [103] D. Gabor et al., *A new microscopic principle*, Nature **161**, 777 (1948).
- [104] A. Kinkhabwala, Z. Yu, S. Fan, Y. Avlasevich, K. Müllen, and W. Moerner, *Large single-molecule fluorescence enhancements produced by a bowtie nanoantenna*, Nature Photonics **3**, 654 (2009).
- [105] M. E. Stewart, C. R. Anderton, L. B. Thompson, J. Maria, S. K. Gray, J. A. Rogers, and R. G. Nuzzo, *Nanostructured plasmonic sensors*, Chemical reviews **108**, 494 (2008).
- [106] S. T. Hess, T. P. Girirajan, and M. D. Mason, *Ultra-high resolution imaging by fluorescence photoactivation localization microscopy*, Biophysical journal **91**, 4258 (2006).
- [107] S.-H. Kwon, J.-H. Kang, C. Seassal, S.-K. Kim, P. Regreny, Y.-H. Lee, C. M. Lieber, and H.-G. Park, *Subwavelength plasmonic lasing from a semiconductor nanodisk with silver nanopan cavity*, Nano letters **10**, 3679 (2010).

## References

---

- [108] S. A. Maier, P. G. Kik, H. A. Atwater, S. Meltzer, E. Harel, B. E. Koel, and A. A. Requicha, *Local detection of electromagnetic energy transport below the diffraction limit in metal nanoparticle plasmon waveguides*, *Nature materials* **2**, 229 (2003).
- [109] F. Couny, P. Light, F. Benabid, and P. S. J. Russell, *Electromagnetically induced transparency and saturable absorption in all-fiber devices based on  $12\text{C}_2\text{H}_2$ -filled hollow-core photonic crystal fiber*, *Optics communications* **263**, 28 (2006).
- [110] P. Drude, *Zur Elektronentheorie der Metalle*, *Annalen der Physik* **306**, 566 (1900).
- [111] R. Ritchie, *Plasma losses by fast electrons in thin films*, *Physical Review* **106**, 874 (1957).
- [112] W. Holland and D. Hall, *Surface-plasmon dispersion relation: Shifts induced by the interaction with localized plasma resonances*, *Physical Review B* **27**, 7765 (1983).
- [113] K. Arya, Z. Su, and J. L. Birman, *Localization of the surface plasmon polariton caused by random roughness and its role in surface-enhanced optical phenomena*, *Physical review letters* **54**, 1559 (1985).
- [114] R. W. Wood, *On a remarkable case of uneven distribution of light in a diffraction grating spectrum*, *Proceedings of the Physical Society of London* **18**, 269 (1902).
- [115] L. Rayleigh, *III. Note on the remarkable case of diffraction spectra described by Prof. Wood*, *Philosophical Magazine Series 6* **14**, 60 (1907).
- [116] L. Rayleigh, *On the Dynamical Theory of Gratings*, *Proceedings of the Royal Society of London. Series A* **79**, 399 (1907).
- [117] E. M. Hicks, S. Zou, G. C. Schatz, K. G. Spears, R. P. Van Duyne, L. Gunnarsson, T. Rindzevicius, B. Kasemo, and M. Käll, *Controlling plasmon line shapes through diffractive coupling in linear arrays of cylindrical nanoparticles fabricated by electron beam lithography*, *Nano letters* **5**, 1065 (2005).
- [118] F. J. G. de Abajo, J. J. Sáenz, I. Campillo, and J. S. Dolado, *Site and lattice resonances in metallic hole arrays*, *Opt. Express* **14**, 7 (2006).
- [119] F. J. García de Abajo, *Colloquium: Light scattering by particle and hole arrays*, *Reviews of Modern Physics* **79**, 1267 (2007).
- [120] B. Auguie and W. Barnes, *Collective Resonances in Gold Nanoparticle Arrays*, *Physical Review Letters* **101**, 1 (2008).
- [121] V. Kravets, F. Schedin, and a. Grigorenko, *Extremely Narrow Plasmon Resonances Based on Diffraction Coupling of Localized Plasmons in Arrays of Metallic Nanoparticles*, *Physical Review Letters* **101**, 087403 (2008).
- [122] G. Vecchi, V. Giannini, and J. Gómez Rivas, *Surface modes in plasmonic crystals induced by diffractive coupling of nanoantennas*, *Phys. Rev. B* **80**, 201401 (2009).

- 
- [123] S. R. K. Rodriguez, A. Abass, B. Maes, O. T. A. Janssen, G. Vecchi, and J. Gómez Rivas, *Coupling Bright and Dark Plasmonic Lattice Resonances*, Phys. Rev. X **1**, 021019 (2011).
- [124] T. V. Teperik and A. Degiron, *Design strategies to tailor the narrow plasmon-photonic resonances in arrays of metallic nanoparticles*, Phys. Rev. B **86**, 245425 (2012).
- [125] A. Bitzer, J. Wallauer, H. Helm, H. Merbold, T. Feurer, and M. Walther, *Lattice modes mediate radiative coupling in metamaterial arrays*, Optics Express **17**, 758 (2009).
- [126] B. Ng, S. M. Hanham, V. Giannini, Z. C. Chen, M. Tang, Y. F. Liew, N. Klein, M. H. Hong, and S. a. Maier, *Lattice resonances in antenna arrays for liquid sensing in the terahertz regime*, Optics Express **19**, 14653 (2011).
- [127] R. Singh, C. Rockstuhl, and W. Zhang, *Strong influence of packing density in terahertz metamaterials*, Applied Physics Letters **97**, 241108 (2010).
- [128] M. Schaafsma and J. Gómez Rivas, *Semiconductor plasmonic crystals: active control of THz extinction*, Semiconductor Science and Technology **28**, 124003 (2013).
- [129] B. Gallinet and O. J. F. Martin, *Relation between near-field and far-field properties of plasmonic Fano resonances*, Optics Express **19**, 22167 (2011).
- [130] P. K. Jain and M. A. El-Sayed, *Plasmonic coupling in noble metal nanostructures*, Chemical Physics Letters **487**, 153 (2010).
- [131] J. B. Lassiter, H. Sobhani, M. W. Knight, W. S. Mielczarek, P. Nordlander, and N. J. Halas, *Designing and Deconstructing the Fano Lineshape in Plasmonic Nanoclusters*, Nano letters **12**, 1 (2012).
- [132] E. Synge, *XXXVIII. A suggested method for extending microscopic resolution into the ultra-microscopic region*, The London, Edinburgh, and Dublin Philosophical Magazine and Journal of Science **6**, 356 (1928).
- [133] D. Courjon, K. Sarayedine, and M. Spajer, *Scanning tunneling optical microscopy*, Optics Communications **71**, 23 (1989).
- [134] R. C. Reddick, R. J. Warmack, and T. L. Ferrell, *New form of scanning optical microscopy*, Phys. Rev. B **39**, 767 (1989).
- [135] F. de Fornel, J. P. Goudonnet, L. Salomon, and E. Lesniewska, *An Evanescent Field Optical Microscope*, Proc. SPIE **1139**, 77 (1989).
- [136] M. Balistreri, J. Korterik, L. Kiupers, and N. van Hulst, *Phase mapping of optical fields in integrated optical waveguide structures*, Lightwave Technology, Journal of **19**, 1169 (2001).
- [137] H. Ditlbacher, A. Hohenau, D. Wagner, U. Kreibig, M. Rogers, F. Hofer, F. R. Aussenegg, and J. R. Krenn, *Silver Nanowires as Surface Plasmon Resonators*, Phys. Rev. Lett. **95**, 257403 (2005).

- [138] J. A. Veerman, A. M. Otter, L. Kuipers, and N. F. van Hulst, *High definition aperture probes for near-field optical microscopy fabricated by focused ion beam milling*, Applied Physics Letters **72** (1998).
- [139] K. G. Lee, H. W. Kihm, J. E. Kihm, W. J. Choi, H. Kim, C. Ropers, D. J. Park, Y. C. Yoon, S. C. Choi, D. H. Woo, J. Kim, B. Lee, Q. H. Park, C. Lienau, and D. S. Kim, *Vector field microscopic imaging of light*, Nat Photon **1** (2007).
- [140] A. E. Klein, N. Janunts, M. Steinert, A. Tünnermann, and T. Pertsch, *Polarization-Resolved Near-Field Mapping of Plasmonic Aperture Emission by a Dual-SNOM System*, Nano Letters **14**, 5010 (2014).
- [141] P. Sarriugarte, M. Schnell, A. Chuvilin, and R. Hillenbrand, *Polarization-Resolved Near-Field Characterization of Nanoscale Infrared Modes in Transmission Lines Fabricated by Gallium and Helium Ion Beam Milling*, ACS Photonics **1**, 604 (2014).
- [142] S. Hunsche, M. Koch, I. Brener, and M. Nuss, *THz near-field imaging*, Optics Communications **150**, 22 (1998).
- [143] Q. Chen, Z. Jiang, G. X. Xu, and X.-C. Zhang, *Near-field terahertz imaging with a dynamic aperture*, Opt. Lett. **25**, 1122 (2000).
- [144] K. Wang, D. M. Mittleman, N. C. J. van der Valk, and P. C. M. Planken, *Antenna effects in terahertz apertureless near-field optical microscopy*, Applied Physics Letters **85**, 2715 (2004).
- [145] G. C. Cho, H.-T. Chen, S. Kraatz, N. Karpowicz, and R. Kersting, *Apertureless terahertz near-field microscopy*, Semiconductor Science and Technology **20**, S286 (2005).
- [146] A. J. Huber, F. Keilmann, J. Wittborn, J. Aizpurua, and R. Hillenbrand, *Terahertz Near-Field Nanoscopy of Mobile Carriers in Single Semiconductor Nanodevices*, Nano Letters **8**, 3766 (2008).
- [147] A. J. Adam, J. M. Brok, P. C. Planken, M. A. Seo, and D. S. Kim, *THz near-field measurements of metal structures*, Comptes Rendus Physique **9**, 161 (2008).
- [148] F. Blanchard, A. Doi, T. Tanaka, H. Hirori, H. Tanaka, Y. Kadoya, and K. Tanaka, *Real-time terahertz near-field microscope*, Opt. Express **19**, 8277 (2011).
- [149] O. Mitrofanov, M. Lee, J. W. P. Hsu, I. Brener, R. Harel, J. F. Federici, J. D. Wynn, L. N. Pfeiffer, and K. W. West, *Collection-mode near-field imaging with 0.5-THz pulses*, IEEE Journal of Selected Topics in Quantum Electronics **7**, 600 (2001).
- [150] M. Wächter, M. Nagel, and H. Kurz, *Tapered photoconductive terahertz field probe tip with subwavelength spatial resolution*, Applied Physics Letters **95** (2009).
- [151] J. R. Knab, A. J. L. Adam, M. Nagel, E. Shaner, M. A. Seo, D. S. Kim, and P. C. M. Planken, *Terahertz Near-Field Vectorial Imaging of Subwavelength Apertures and Aperture Arrays*, Opt. Express **17**, 15072 (2009).

- 
- [152] A. Bitzer, A. Ortner, and M. Walther, *Terahertz near-field microscopy with subwavelength spatial resolution based on photoconductive antennas*, *Appl. Opt.* **49**, E1 (2010).
- [153] D.-J. Lee, N.-W. Kang, J.-H. Choi, J. Kim, and J. F. Whitaker, *Recent Advances in the Design of Electro-Optic Sensors for Minimally Destructive Microwave Field Probing*, *Sensors* **11**, 806 (2011).
- [154] E. R. Brown, F. W. Smith, and K. A. McIntosh, *Coherent millimeter-wave generation by hetrodyne conversion in low-temperature-grown GaAs photoconductors*, *Journal of Applied Physics* **73**, 1480 (1993).
- [155] J. Kim, S. Williamson, J. Nees, S. Wakana, and J. Whitaker, *Photoconductive sampling probe with 2.3-ps temporal resolution and 4- $\mu$ V sensitivity*, *Applied Physics Letters* **62**, 2268 (1993).
- [156] L. Novotny, *Chapter 5 The history of near-field optics*, volume 50 of *Progress in Optics*, pages 137 – 184, Elsevier, 2007.
- [157] J. R. Krenn, A. Dereux, J. C. Weeber, E. Bourillot, Y. Lacroute, J. P. Goudonnet, G. Schider, W. Gotschy, A. Leitner, F. R. Aussenegg, and C. Girard, *Squeezing the Optical Near-Field Zone by Plasmon Coupling of Metallic Nanoparticles*, *Phys. Rev. Lett.* **82**, 2590 (1999).
- [158] H. Xu, J. Aizpurua, M. Käll, and P. Apell, *Electromagnetic contributions to single-molecule sensitivity in surface-enhanced Raman scattering*, *Phys. Rev. E* **62**, 4318 (2000).
- [159] M. L. Brongersma, J. W. Hartman, and H. A. Atwater, *Electromagnetic energy transfer and switching in nanoparticle chain arrays below the diffraction limit*, *Phys. Rev. B* **62**, R16356 (2000).
- [160] S. A. Maier, M. L. Brongersma, P. G. Kik, S. Meltzer, A. A. G. Requicha, and H. A. Atwater, *Plasmonics-A Route to Nanoscale Optical Devices*, *Advanced Materials* **13**, 1501 (2001).
- [161] N. N. Lepeshkin, A. Schweinsberg, G. Piredda, R. S. Bennink, and R. W. Boyd, *Enhanced Nonlinear Optical Response of One-Dimensional Metal-Dielectric Photonic Crystals*, *Phys. Rev. Lett.* **93**, 123902 (2004).
- [162] F. Svedberg, Z. Li, H. Xu, and M. Käll, *Creating Hot Nanoparticle Pairs for Surface-Enhanced Raman Spectroscopy through Optical Manipulation*, *Nano Letters* **6**, 2639 (2006).
- [163] *THz near-field optical imaging by a local source*, *Optics Communications* **262**, 125 (2006).
- [164] A. Bitzer and M. Walther, *Terahertz near-field imaging of metallic subwavelength holes and hole arrays*, *Applied Physics Letters* **92** (2008).

- [165] T. Cocker, J. Vedran, M. Gupta, S. Molesky, J. Burgess, G. Reyes, L. Titova, Y. Tsui, M. Freeman, and F. Hegmann, *An ultrafast terahertz scanning tunnelling microscope*, Nat. Photon. **7**, 620 (2013).
- [166] O. Mitrofanov, F. Dominec, P. Kužel, J. L. Reno, I. Brener, U.-C. Chung, C. Elissalde, M. Maglione, and P. Mounaix, *Near-field probing of Mie resonances in single TiO<sub>2</sub> microspheres at terahertz frequencies*, Opt. Express **22**, 23034 (2014).
- [167] A. Berrier, P. Albella, M. A. Poyli, R. Ulbricht, M. Bonn, J. Aizpurua, and J. G. Rivas, *Detection of deep-subwavelength dielectric layers at terahertz frequencies using semiconductor plasmonic resonators*, Optics Express **20**, 5052 (2012).
- [168] W. Withayachumnankul, H. Lin, K. Serita, C. M. Shah, S. Sriram, M. Bhaskaran, M. Tonouchi, C. Fumeaux, and D. Abbott, *Sub-diffraction thin-film sensing with planar terahertz metamaterials*, Opt. Express **20**, 3345 (2012).
- [169] A. Berrier, M. C. Schaafsma, G. Nonglaton, J. Bergquist, and J. G. Rivas, *Selective detection of bacterial layers with terahertz plasmonic antennas*, Biomed. Opt. Express **3**, 2937 (2012).
- [170] S. J. Park, J. T. Hong, S. J. Choi, H. S. Kim, W. K. Park, S. T. Han, J. Y. Park, S. Lee, D. S. Kim, and Y. H. Ahn, *Detection of microorganisms using terahertz metamaterials*, Scientific Reports **4**, 4988 (2014).
- [171] R. Singh, W. Cao, I. Al-Naib, L. Cong, W. Withayachumnankul, and W. Zhang, *Ultrasensitive terahertz sensing with high-Q Fano resonances in metasurfaces*, Applied Physics Letters **105** (2014).
- [172] K. Ueno, S. Nozawa, and H. Misawa, *Surface-enhanced terahertz spectroscopy using gold rod structures resonant with terahertz waves*, Opt. Express **23**, 28584 (2015).
- [173] S. R. J. Bhatt, P. Bhatt, P. Deshmukh, B. R. Sangala, M. N. Satyanarayan, G. Umesh, and S. S. Prabhu, *Resonant Terahertz InSb Waveguide Device for Sensing Polymers*, Journal of Infrared, Millimeter, and Terahertz Waves **37**, 795 (2016).
- [174] N. Yu, P. Genevet, F. Aieta, M. A. Kats, R. Blanchard, G. Aoust, J. P. Tetienne, Z. Gaburro, and F. Capasso, *Flat Optics: Controlling Wavefronts With Optical Antenna Metasurfaces*, IEEE Journal of Selected Topics in Quantum Electronics **19**, 4700423 (2013).
- [175] P. Alonso-González, P. Albella, F. Neubrech, C. Huck, J. Chen, F. Golmar, F. Casanova, L. E. Hueso, A. Pucci, J. Aizpurua, and R. Hillenbrand, *Experimental Verification of the Spectral Shift between Near- and Far-Field Peak Intensities of Plasmonic Infrared Nanoantennas*, Phys. Rev. Lett. **110**, 203902 (2013).
- [176] A. Bhattacharya, G. Georgiou, S. Sawallich, C. Matheisen, M. Nagel, and J. Gómez Rivas, *Large near-to-far field spectral shifts for terahertz resonances*, Phys. Rev. B **93**, 035438 (2016).

- 
- [177] T. Neuman, P. Alonso-González, A. Garcia-Etxarri, M. Schnell, R. Hillenbrand, and J. Aizpurua, *Mapping the near fields of plasmonic nanoantennas by scattering-type scanning near-field optical microscopy*, *Laser and Photonics Reviews* **9**, 637 (2015).
- [178] K. Yang, L. P. B. Katehi, and J. F. Whitaker, *Electro-optic field mapping system utilizing external gallium arsenide probes*, *Applied Physics Letters* **77** (2000).
- [179] M. A. Seo, A. J. L. Adam, J. H. Kang, J. W. Lee, S. C. Jeoung, Q. H. Park, P. C. M. Planken, and D. S. Kim, *Fourier-transform terahertz near-field imaging of one-dimensional slit arrays: mapping of electric-field-, magnetic-field-, and Poynting vectors*, *Opt. Express* **15**, 11781 (2007).
- [180] N. Kumar, A. C. Strikwerda, K. Fan, X. Zhang, R. D. Averitt, P. C. M. Planken, and A. J. L. Adam, *THz near-field Faraday imaging in hybrid metamaterials*, *Opt. Express* **20**, 11277 (2012).
- [181] Y. Xu, X. Zhang, Z. Tian, J. Gu, C. Ouyang, Y. Li, J. Han, and W. Zhang, *Mapping the near-field propagation of surface plasmons on terahertz metasurfaces*, *Applied Physics Letters* **107** (2015).
- [182] F. J. García-Vidal and J. B. Pendry, *Collective Theory for Surface Enhanced Raman Scattering*, *Phys. Rev. Lett.* **77**, 1163 (1996).
- [183] K. Kneipp, Y. Wang, H. Kneipp, L. T. Perelman, I. Itzkan, R. R. Dasari, and M. S. Feld, *Single Molecule Detection Using Surface-Enhanced Raman Scattering (SERS)*, *Phys. Rev. Lett.* **78**, 1667 (1997).
- [184] F. Neubrech, A. Pucci, T. W. Cornelius, S. Karim, A. García-Etxarri, and J. Aizpurua, *Resonant Plasmonic and Vibrational Coupling in a Tailored Nanoantenna for Infrared Detection*, *Phys. Rev. Lett.* **101**, 157403 (2008).
- [185] J. P. Camden, J. A. Dieringer, J. Zhao, and R. P. Van Duyne, *Controlled Plasmonic Nanostructures for Surface-Enhanced Spectroscopy and Sensing*, *Accounts of Chemical Research* **41**, 1653 (2008).
- [186] M. A. Seo, H. R. Park, S. M. Koo, D. J. Park, J. H. Kang, O. K. Suwal, S. S. Choi, P. C. M. Planken, G. S. Park, N. K. Park, Q. H. Park, and D. S. Kim, *Terahertz field enhancement by a metallic nano slit operating beyond the skin-depth limit*, *Nat Photon* **3**, 152 (2009).
- [187] A. Berrier, R. Ulbricht, M. Bonn, and J. G. Rivas, *Ultrafast active control of localized surface plasmon resonances in silicon bowtie antennas*, *Opt. Express* **18**, 23226 (2010).
- [188] V. Giannini, A. Berrier, S. A. Maier, J. A. Sánchez-Gil, and J. G. Rivas, *Scattering efficiency and near field enhancement of active semiconductor plasmonic antennas at terahertz frequencies*, *Opt. Express* **18**, 2797 (2010).

## References

---

- [189] L. Razzari, A. Toma, M. Shalaby, M. Clerici, R. P. Zaccaria, C. Liberale, S. Marras, I. A. I. Al-Naib, G. Das, F. D. Angelis, M. Peccianti, A. Falqui, T. Ozaki, R. Morandotti, and E. D. Fabrizio, *Extremely large extinction efficiency and field enhancement in terahertz resonant dipole nanoantennas*, *Opt. Express* **19**, 26088 (2011).
- [190] V. Giannini, G. Vecchi, and J. Gómez Rivas, *Lighting Up Multipolar Surface Plasmon Polaritons by Collective Resonances in Arrays of Nanoantennas*, *Phys. Rev. Lett.* **105**, 266801 (2010).
- [191] C. A. Werley, K. Fan, A. C. Strikwerda, S. M. Teo, X. Zhang, R. D. Averitt, and K. A. Nelson, *Time-resolved imaging of near-fields in THz antennas and direct quantitative measurement of field enhancements*, *Opt. Express* **20**, 8551 (2012).
- [192] J. Zuloaga and P. Nordlander, *On the Energy Shift between Near-Field and Far-Field Peak Intensities in Localized Plasmon Systems*, *Nano Letters* **11**, 1280 (2011).
- [193] C. Menzel, E. Hebestreit, S. Mühlig, C. Rockstuhl, S. Burger, F. Lederer, and T. Pertsch, *The spectral shift between near- and far-field resonances of optical nano-antennas*, *Opt. Express* **22**, 9971 (2014).
- [194] M. A. Kats, N. Yu, P. Genevet, Z. Gaburro, and F. Capasso, *Effect of radiation damping on the spectral response of plasmonic components*, *Opt. Express* **19**, 21748 (2011).
- [195] U. Fano, *Effects of Configuration Interaction on Intensities and Phase Shifts*, *Phys. Rev.* **124**, 1866 (1961).
- [196] P. J. Schuck, D. P. Fromm, A. Sundaramurthy, G. S. Kino, and W. E. Moerner, *Improving the Mismatch between Light and Nanoscale Objects with Gold Bowtie Nanoantennas*, *Phys. Rev. Lett.* **94**, 017402 (2005).
- [197] A. Kinkhabwala, Z. Yu, S. Fan, Y. Avlasevich, K. Mullen, and W. E. Moerner, *Large single-molecule fluorescence enhancements produced by a bowtie nanoantenna*, *Nat Photon* **3**, 654 (2009).
- [198] T. Hanke, J. Cesar, V. Knittel, A. Trügler, U. Hohenester, A. Leitenstorfer, and R. Bratschitsch, *Tailoring Spatiotemporal Light Confinement in Single Plasmonic Nanoantennas*, *Nano Letters* **12**, 992 (2012).
- [199] A. Singh, G. Calbris, and N. F. van Hulst, *Vectorial Nanoscale Mapping of Optical Antenna Fields by Single Molecule Dipoles*, *Nano Letters* **14**, 4715 (2014).
- [200] H. Fischer and O. J. F. Martin, *Engineering the optical response of plasmonic nanoantennas*, *Opt. Express* **16**, 9144 (2008).
- [201] D. P. Fromm, A. Sundaramurthy, A. Kinkhabwala, P. J. Schuck, G. S. Kino, and W. E. Moerner, *Exploring the chemical enhancement for surface-enhanced Raman scattering with Au bowtie nanoantennas*, *The Journal of Chemical Physics* **124** (2006).

- 
- [202] D. J. Griffiths, *Introduction to Electrodynamics*, Benjamin Cummings, 3 edition, 1999.
- [203] A. E. Miroshnichenko, S. Flach, and Y. S. Kivshar, *Fano resonances in nanoscale structures*, *Rev. Mod. Phys.* **82**, 2257 (2010).
- [204] E. Hutter and J. H. Fendler, *Exploitation of localized surface plasmon resonance*, *Advanced Materials* **16**, 1685 (2004).
- [205] S. A. Maier and H. A. Atwater, *Plasmonics: Localization and guiding of electromagnetic energy in metal/dielectric structures*, *Journal of Applied Physics* **98**, 011101 (2005).
- [206] P. Nordlander, C. Oubre, E. Prodan, K. Li, and M. Stockman, *Plasmon hybridization in nanoparticle dimers*, *Nano Letters* **4**, 899 (2004).
- [207] I. Romero, J. Aizpurua, G. W. Bryant, and F. J. García De Abajo, *Plasmons in nearly touching metallic nanoparticles: singular response in the limit of touching dimers*, *Optics Express* **14**, 9988 (2006).
- [208] O. L. Muskens, V. Giannini, J. A. Sánchez-Gil, and J. G. Rivas, *Optical scattering resonances of single and coupled dimer plasmonic nanoantennas*, *Opt. Express* **15**, 17736 (2007).
- [209] B. Luk'yanchuk, N. I. Zheludev, S. A. Maier, N. J. Halas, P. Nordlander, H. Giessen, and C. T. Chong, *The Fano resonance in plasmonic nanostructures and metamaterials*, *Nature materials* **9**, 707 (2010).
- [210] S. Zhang, D. A. Genov, Y. Wang, M. Liu, and X. Zhang, *Plasmon-Induced Transparency in Metamaterials*, *Phys. Rev. Lett.* **101**, 047401 (2008).
- [211] S.-Y. Chiam, R. Singh, C. Rockstuhl, F. Lederer, W. Zhang, and A. A. Bettiol, *Analogue of electromagnetically induced transparency in a terahertz metamaterial*, *Phys. Rev. B* **80**, 153103 (2009).
- [212] N. Liu, L. Langguth, T. Weiss, J. Kästel, M. Fleischhauer, T. Pfau, and H. Giessen, *Plasmonic analogue of electromagnetically induced transparency at the Drude damping limit*, *Nature materials* **8**, 758 (2009).
- [213] A. F. Koenderink, *Plasmon Nanoparticle Array Waveguides for Single Photon and Single Plasmon Sources*, *Nano Letters* **9**, 4228 (2009).
- [214] S. R. K. Rodriguez, S. Murai, M. A. Verschuuren, and J. G. Rivas, *Light-Emitting Waveguide-Plasmon Polaritons*, *Phys. Rev. Lett.* **109**, 166803 (2012).
- [215] M. Fleischhauer, A. Imamoglu, and J. P. Marangos, *Electromagnetically induced transparency: Optics in coherent media*, *Rev. Mod. Phys.* **77**, 633 (2005).

## References

---

- [216] A. B. Evlyukhin, S. I. Bozhevolnyi, A. Pors, M. G. Nielsen, I. P. Radko, M. Willatzen, and O. Albrektsen, *Detuned electrical dipoles for plasmonic sensing*, Nano Letters **10**, 4571 (2010).
- [217] S. I. Bozhevolnyi, A. B. Evlyukhin, A. Pors, M. G. Nielsen, M. Willatzen, and O. Albrektsen, *Optical transparency by detuned electrical dipoles*, New Journal of Physics **13**, 023034 (2011).
- [218] A. Pors, M. Willatzen, O. Albrektsen, and S. I. Bozhevolnyi, *Detuned electrical dipoles metamaterial with bianisotropic response*, Physical Review B **83**, 245409 (2011).
- [219] A. Miroshnichenko, S. Flach, and Y. Kivshar, *Fano resonances in nanoscale structures*, Rev. Mod. Phys. **82**, 2257 (2010).
- [220] D. Smith, H. Chang, K. Fuller, A. Rosenberger, and R. Boyd, *Coupled-resonator-induced transparency*, Phys. Rev. A **69**, 063804 (2004).
- [221] R. Kekatpure, E. Barnard, W. Cai, and M. Brongersma, *Phase-Coupled Plasmon-Induced Transparency*, Phys. Rev. Lett. **104**, 243902 (2010).
- [222] M. Yanik, W. Suh, Z. Wang, and S. Fan, *Stopping Light in a Waveguide with an All-Optical Analog of Electromagnetically Induced Transparency*, Phys. Rev. Lett. **93**, 233903 (2004).
- [223] K. Totsuka, N. Kobayashi, and M. Tomita, *Slow Light in Coupled-Resonator-Induced Transparency*, Phys. Rev. Lett. **98**, 213904 (2007).
- [224] Q. Xu, S. Sandhu, M. Povinelli, J. Shakya, S. Fan, and M. Lipson, *Experimental Realization of an On-Chip All-Optical Analogue to Electromagnetically Induced Transparency*, Phys. Rev. Lett. **96**, 123901 (2006).
- [225] A. D. Humphrey, N. Meinzer, T. A. Starkey, and W. L. Barnes.
- [226] F. G. Sedgwick, B. Pesala, J.-Y. Lin, W. S. Ko, X. Zhao, and C. J. Chang-Hasnain, *THz-bandwidth tunable slow light in semiconductor optical amplifiers*, Opt. Express **15**, 747 (2007).
- [227] Q. Gan, Z. Fu, Y. J. Ding, and F. J. Bartoli, *Ultrawide-Bandwidth Slow-Light System Based on THz Plasmonic Graded Metallic Grating Structures*, Phys. Rev. Lett. **100**, 256803 (2008).
- [228] J. Zhang, L. Cai, W. Bai, Y. Xu, and G. Song, *Slow light at terahertz frequencies in surface plasmon polariton assisted grating waveguide*, Journal of Applied Physics **106**, (2009).
- [229] Q. Bai, C. Liu, J. Chen, C. Cheng, M. Kang, and H.-T. Wang, *Tunable slow light in semiconductor metamaterial in a broad terahertz regime*, Journal of Applied Physics **107**, (2010).

- [230] J. G. Rivas, A. F. Benet, J. Niehusmann, P. H. Bolivar, and H. Kurz, *Time-resolved broadband analysis of slow-light propagation and superluminal transmission of electromagnetic waves in three-dimensional photonic crystals*, Phys. Rev. B **71**, 155110 (2005).
- [231] T. Zentgraf, S. Zhang, R. F. Oulton, and X. Zhang, *Ultranarrow coupling-induced transparency bands in hybrid plasmonic systems*, Phys. Rev. B **80**, 195415 (2009).
- [232] T. Jensen, L. Kelly, A. Lazarides, and G. C. Schatz, *Electrodynamics of Noble Metal Nanoparticles and Nanoparticle Clusters*, Journal of Cluster Science **10**, 295 (1999).
- [233] F. G. De Abajo and J. Sáenz, *Electromagnetic surface modes in structured perfect-conductor surfaces*, Physical Review Letters **95**, 233901 (2005).
- [234] S. Zou and G. C. Schatz, *Narrow plasmonic/photonic extinction and scattering line shapes for one and two dimensional silver nanoparticle arrays*, The Journal of chemical physics **121**, 12606 (2004).
- [235] H. C. van de Hulst, *Light Scattering by small particles*, Dover Publications, Inc., 1981.
- [236] V. Giannini, A. Berrier, S. A. Maier, J. A. Sánchez-Gil, and J. G. Rivas, *Scattering efficiency and near field enhancement of active semiconductor plasmonic antennas at terahertz frequencies.*, Optics Express **18**, 2797 (2010).
- [237] L. Razzari, A. Toma, M. Shalaby, M. Clerici, R. P. Zaccaria, C. Liberale, S. Marras, I. A. I. Al-Naib, G. Das, F. De Angelis, M. Peccianti, A. Falqui, T. Ozaki, R. Morandotti, and E. Di Fabrizio, *Extremely large extinction efficiency and field enhancement in terahertz resonant dipole nanoantennas*, Optics Express **19**, 26088 (2011).
- [238] H.-T. Chen, W. J. Padilla, J. M. O. Zide, A. C. Gossard, A. J. Taylor, and R. D. Averitt, *Active terahertz metamaterial devices*, Nature **444**, 597 (2006).
- [239] J. Gu, R. Singh, X. Liu, X. Zhang, Y. Ma, S. Zhang, S. A. Maier, Z. Tian, A. K. Azad, H.-T. Chen, A. J. Taylor, J. Han, and W. Zhang, *Active control of electromagnetically induced transparency analogue in terahertz metamaterials.*, Nature Communications **3**, 1151 (2012).
- [240] M. Seo, J. Kyoung, H. Park, S. Koo, H.-s. Kim, H. Bernien, B. J. Kim, J. H. Choe, Y. H. Ahn, H.-T. Kim, N. Park, Q.-H. Park, K. Ahn, and D.-s. Kim, *Active Terahertz Nanoantennas Based on VO<sub>2</sub> Phase Transition*, Nano letters **10**, 2064 (2010).
- [241] T. P. Steinbusch, H. K. Tyagi, M. C. Schaafsma, G. Georgiou, and J. Gómez Rivas, *Active terahertz beam steering by photo-generated graded index gratings in thin semiconductor films*, Optics Express **22**, 26559 (2014).
- [242] R. Singh, E. Smirnova, A. J. Taylor, J. F. O'Hara, and W. Zhang, *Optically thin terahertz metamaterials.*, Optics Express **16**, 6537 (2008).

## References

---

- [243] C. A. Werley, K. Fan, A. C. Strikwerda, S. M. Teo, X. Zhang, R. D. Averitt, and K. A. Nelson, *Time-resolved imaging of near-fields in THz antennas and direct quantitative measurement of field enhancements.*, Optics Express **20**, 8551 (2012).
- [244] A. Bhattacharya, G. Georgiou, S. Sawallich, and C. Matheisen, *Large near-to-far field spectral shifts for terahertz resonances*, Physical Review B (2016).
- [245] S. Zhang, D. A. Genov, Y. Wang, M. Liu, and X. Zhang, *Plasmon-Induced Transparency in Metamaterials*, Physical Review Letters **101**, 047401 (2008).
- [246] N. Liu, L. Langguth, T. Weiss, J. Kästel, M. Fleischhauer, T. Pfau, and H. Giessen, *Plasmonic analogue of electromagnetically induced transparency at the Drude damping limit*, Nature materials **8**, 758 (2009).
- [247] N. Liu, T. Weiss, M. Mesch, L. Langguth, U. Eigenthaler, M. Hirscher, C. Sönnichsen, and H. Giessen, *Planar Metamaterial Analogue of Electromagnetically Induced Transparency for Plasmonic Sensing*, Nano letters **10**, 1103 (2010).
- [248] Z. Ye, S. Zhang, Y. Wang, Y.-S. Park, T. Zentgraf, G. Bartal, X. Yin, and X. Zhang, *Mapping the near-field dynamics in plasmon-induced transparency*, Physical Review B **86**, 155148 (2012).
- [249] T. Coenen, D. T. Schoen, B. J. M. Brenny, A. Polman, and M. L. Brongersma, *Combined electron energy-loss and cathodoluminescence spectroscopy on individual and composite plasmonic nanostructures*, Physical Review B **93**, 195429 (2016).
- [250] S.-C. Yang, H. Kobori, C.-L. He, M.-H. Lin, H.-Y. Chen, C. Li, M. Kanehara, T. Teranishi, and S. Gwo, *Plasmon Hybridization in Individual Gold Nanocrystal Dimers: Direct Observation of Bright and Dark Modes*, Nano letters **10**, 632 (2010).
- [251] N. Ocelic, A. Huber, and R. Hillenbrand, *Pseudoheterodyne detection for background-free near-field spectroscopy*, Applied Physics Letters **89**, 101124 (2006).
- [252] S. I. Bozhevolnyi, A. B. Evlyukhin, A. Pors, M. G. Nielsen, M. Willatzen, and O. Albrektsen, *Optical transparency by detuned electrical dipoles*, New Journal of Physics **13**, 023034 (2011).
- [253] J. Sui and L. Feng, *Optically and thermally controlled terahertz metamaterial via transition between direct and indirect electromagnetically induced transparency*, AIP Advances **4**, 127122 (2014).
- [254] M. Wan, Y. Song, L. Zhang, and F. Zhou, *Broadband plasmon-induced transparency in terahertz metamaterials via constructive interference of electric and magnetic couplings*, Optics Express **23**, 27361 (2015).
- [255] X. Yin, T. Feng, S. Yip, Z. Liang, A. Hui, J. C. Ho, and J. Li, *Tailoring electromagnetically induced transparency for terahertz metamaterials: From diatomic to triatomic structural molecules*, Applied Physics Letters **103**, 021115 (2013).

# SUMMARY

---

The understanding of electromagnetic radiation and its interaction with matter, (*Optics*, broadly speaking), have engaged the brightest minds from ancient times to these days. Being one of the oldest fields of research, optics has evolved enormously over time. One of the most dramatic evolution is that of understanding light-matter interactions in the sub-wavelength scales. This led to a revolution in optical instrumentation in terms of size and efficiencies. The study of electromagnetic radiation, other than the visible spectrum, also gained momentum at the same time. One spectral band of interest is the Terahertz (THz) frequency window. The THz frequencies correspond frequencies of 0.1 to 10 THz, with free space wavelengths of 0.3 to 3 mm, and with characteristic photon energies ranging from 0.4 to 40 meV. It is only recently, that research at this part of the electromagnetic spectrum has gained a huge momentum, although the interest due to unique properties of these region were well known. Firstly, most materials have spectroscopic signatures at this frequency range due to low energy rotational and vibrational modes of the constituent molecules of matter. Due to relatively slow oscillations of the electromagnetic fields, compared to the optical counterpart, it is possible to measure the full THz electromagnetic transient field in time domain with simple optomechanics. This allows a direct probe of the complex dielectric constant of most materials at THz frequencies. Furthermore, THz frequencies have low photon energies, thus it is non-ionizing. All these features make THz a perfect candidate for contact-less spectroscopy. Secondly, THz frequencies offers the possibility of quenching the bottleneck between optical and microwave communication in terms of bandwidth. Intrinsically, its ability to penetrate most materials without significant effect, makes THz a better choice than microwaves for wireless communication; added to that it also offers more bandwidth. So it is not surprising that THz is finding relevance in many modern research directions as well as daily applications, such as, spectroscopy and material research, semiconductor science, bio-medical sciences, high-speed communication engineering, astronomy, security and quality control. However, THz being a relatively new research direction, the instrumentation is not fully optimized for many daily applications. A lot of scientific effort is being put into this pursuit presently.

In this thesis, we study the interactions of THz radiation with resonant subwavelength structures. The motivation behind this study is two-fold. Firstly, the limitation faced by conventional THz spectroscopy is the large diffraction limited spot size of the probe beam.

This makes probing new energy-relevant materials such as, graphene, 2D semiconductors, nanowires and perovskites impossible due to their sub-millimeter surface profiles. So it is necessary to confine THz radiation beyond the diffraction limit for spectroscopic purposes. Photonic structures have the ability to do this very efficiently. Secondly, arrays of such photonic structures can efficiently cause large changes to the THz radiation, making them relevant for THz communication systems. However, for these devices to work efficiently, we need to study, understand and optimize their interaction with the THz radiation by studying the near-field distributions in the vicinity of these structures. This is why we have developed a THz near-field micro-spectrometer which can measure a broadband THz electric near-field in the time domain with a subwavelength spatial resolution of 10 microns.

In the *Introduction* of this thesis, we have presented a broad historical overview of optics followed by a general discussion on THz frequencies. We discussed the various generation and detection mechanisms of THz radiation along with the different measurement techniques.

In *Chapter 2*, we have presented the basic concepts of the interaction of light with matter in subwavelength scales. This study is based on the creation, manipulation and detection of near-fields in the vicinity of subwavelength structures. In this chapter, we have also presented the THz near-field micro-spectroscopy setup that was developed during the course of this thesis.

In *Chapter 3*, we have shown how such a device can be used to map the complete transient electric near-field vector using time-domain spectroscopy near a resonant sub-wavelength resonator. For the sake of simplicity we used the simplest geometry of a resonant rod. We have also provided a complete description of the three dimensional distribution of the electric fields around the resonator on resonance.

In *Chapter 4*, we have shown how conventional far-field spectral signatures can lead to misleading results and established the necessity for near-field spectral characterization of resonant structures. As these results have implications in the field of sub-wavelength spectroscopy using resonant structures at THz frequencies, for this study we chose a structure that is commonly used in spectroscopy of sub-wavelength objects, i.e., bowtie resonators.

In *Chapter 5*, we have studied the coupling of THz fields in photonic metasurfaces to create changes in the far-field spectrum. The technique used for this study is that of diffractive coupling between resonant structures (frequency detuned gold rods) in a lattice by Rayleigh anomalies (diffraction orders in the plane of the lattice). Far-field coupling of THz fields with the structures results into near perfect transparency at particular frequencies with highly reduced group velocities. This study has implications in the field of photonic devices for THz communication.

Lastly, in *Chapter 6*, we have shown another mechanism of coupling in which the local fields of individual photonic structures (bright and dark modes) couple to each other in the near-field and show similar effects as in *Chapter 5*. The far-field effect in this case is shown to depend on the overlap between the near-fields of the photonic structures, as expected.

Thus, this thesis aims to provide a holistic picture of how THz radiation interacts with resonant photonic structures in the near-field for a better understanding of THz photonics.

Arkabrata Bhattacharya  
Eindhoven, The Netherlands



# LIST OF PUBLICATIONS

---

This thesis is based on the following publications:

1. *Vectorial Mapping of Complex Electric Near-Field near THz resonators*, A. Bhattacharya and J. Gómez Rivas, APL Photonics 1, 086103 (2016). **(Chapter 3)**
2. *Large near-to-far field spectral shifts for terahertz resonances*, A. Bhattacharya, G. Georgiou, S. Sawallich, C. Mathiessen, M. Nagel and J. Gómez Rivas, Physical Review B 93, 035438 (2016). **(Chapter 4)**
3. *Diffraction enhanced transparency and slow THz light in periodic arrays of detuned and displaced dipoles*, M. C. Schaafsma\*, A. Bhattacharya\* and J. Gómez Rivas, ACS Photonics 3(9), 1596-1603 (2016). **(Chapter 5)**
4. *Visualizing near-field coupling in terahertz dolmens*, A. Halpin, C. Mennes, A. Bhattacharya and J. Gómez Rivas, submitted. **(Chapter 6)**

\* Equal contribution

Other publications by the author:

1. *Combining near- and far-field coupling for improved electromagnetically-induced transparency at terahertz frequencies*, A. Halpin, A. Bhattacharya, C. Mennes, N. van Hoof and J. Gómez Rivas, in preparation.
2. *Vectorial mapping of resonant THz near-fields*, A. Bhattacharya, A. Halpin and J. Gómez Rivas, 41st International Conference on Infrared, Millimeter, and Terahertz waves (IRMMW-THz), Copenhagen, Denmark, pp. 1-2 (2016).
3. *Near-field visualization of electromagnetically induced transparency in resonant structures*, A. Halpin, A. Bhattacharya, C. Mennes and J. Gómez Rivas, 41st International Conference on Infrared, Millimeter, and Terahertz waves (IRMMW-THz), Copenhagen, Denmark, pp. 1-2 (2016).
4. *THz near-field microscopy of semiconductor and metal bowtie antennas*, A. Bhattacharya, G. Georgiou, S. Sawallich, C. Mathiessen, M. Nagel and J. Gómez Rivas, 39th International Conference on Infrared, Millimeter, and Terahertz waves (IRMMW-THz), Tucson, Arizona, USA, pp. 1-1 (2014).
5. *Local THz Resonances in Semiconductors: Active Control of Near-Fields, THz Extinction and Beaming*, J. Gómez Rivas, G. Georgiou, A. Bhattacharya, European Conference on Lasers and Electro-Optics-European Quantum Electronics Conference, Munich, Germany, pp. CC\_4\_3 (2015).
6. *Photo-generated THz Metamaterial and Metasurface*, J. Gómez Rivas, G. Georgiou, A. Bhattacharya, Progress In Electromagnetics Research Symposium Abstracts, Prague, Czech Republic, 1A2 SC2: THz Metamaterials: Fundamentals and Applications, pp. 31 (2015).

Patents:

1. *High resolution terahertz sensing*, A. Bhattacharya, A. Halpin, G. Ramanandan, G. Georgiou, M. Nagel, J. Gómez Rivas. European Patent Office, EP16190229.1.

## ABOUT THE AUTHOR

---

Arkabrata Bhattacharya was born in 1986 in West Bengal, India. He studied Physics at the Presidency College, University of Calcutta, India and received a Bachelors degree in Science with first class. Then he studied Optics and Optoelectronics from the University of Calcutta and received a Bachelors degree in Engineering for the same. Afterwards, he was awarded the prestigious Erasmus Mundus European Union scholarship to follow Master of Science in Photonics Engineering, Nanophotonics and Biophotonics. He studied the first semester at the Institut Fresnel, Marseille, France the second semester at the Karlsruhe Institute of Technology, Karlsruhe, Germany and the final two semesters at the Universitat Politècnica de Catalunya, and ICFO (The Institute of Photonic Sciences), Barcelona, Spain. He completed the Masters with a successful thesis entitled “Quantum non-linear optics with single atoms”. In the year 2013, he joined the Surface Photonics group at FOM Institute AMOLF, Amsterdam, The Netherlands, as a PhD student, to work on near-field micro-spectroscopy of resonant structures at THz frequencies. Later, at 2015, he migrated with the group to the FOM Institute DIFFER, Eindhoven, The Netherlands where he finished his thesis.



His hobbies include watching films from different genres from all over the world, listening to music, travelling, reading, wondering about the various intricacies of life in general.



